LIÈGE université Library

https://lib.uliege.be

https://matheo.uliege.be

Master thesis and internship[BR]- Master's thesis : Towards a laboratory validation of a dual-polarization wavefront sensing with the vortex coronagraph[BR]- Internship

Auteur : Seret, Cédric
Promoteur(s) : Absil, Olivier; Orban De Xivry, Gilles
Faculté : Faculté des Sciences appliquées
Diplôme : Master en ingénieur civil en aérospatiale, à finalité spécialisée en "aerospace engineering"
Année académique : 2023-2024
URI/URL : http://hdl.handle.net/2268.2/20378

Avertissement à l'attention des usagers :

Tous les documents placés en accès ouvert sur le site le site MatheO sont protégés par le droit d'auteur. Conformément aux principes énoncés par la "Budapest Open Access Initiative"(BOAI, 2002), l'utilisateur du site peut lire, télécharger, copier, transmettre, imprimer, chercher ou faire un lien vers le texte intégral de ces documents, les disséquer pour les indexer, s'en servir de données pour un logiciel, ou s'en servir à toute autre fin légale (ou prévue par la réglementation relative au droit d'auteur). Toute utilisation du document à des fins commerciales est strictement interdite.

Par ailleurs, l'utilisateur s'engage à respecter les droits moraux de l'auteur, principalement le droit à l'intégrité de l'oeuvre et le droit de paternité et ce dans toute utilisation que l'utilisateur entreprend. Ainsi, à titre d'exemple, lorsqu'il reproduira un document par extrait ou dans son intégralité, l'utilisateur citera de manière complète les sources telles que mentionnées ci-dessus. Toute utilisation non explicitement autorisée ci-avant (telle que par exemple, la modification du document ou son résumé) nécessite l'autorisation préalable et expresse des auteurs ou de leurs ayants droit.

University of Liège - Faculty of Applied Sciences

Towards a laboratory validation of a dual-polarization wavefront sensing with the vortex coronagraph

Author:

Cédric Seret

Supervisors:

Dr. Olivier Absil
Dr. Gilles Orban de Xivry

Master thesis conducted with the aim of obtaining the degree of Master in Aerospace Engineering

Academic year 2023 - 2024

Abstract

In the context of high-contrast imaging, dual-polarization wavefront sensing represents a very promising solution for non-common path aberrations and aberrations control using the vortex coronagraph. The interest of this method lies in the efficient phase retrieval using the unique polarization behaviour of the vortex coronagraph and the simplicity of its implementation. This method has been progressively implemented on Vortex Optical Demsontrator for Coronagraphic Application (VODCA) test bench using the vortex coronagraph called the Annular Groove Phase Mask (AGPM).

The dual-polarization setup requires the most accurate selection of both orthogonal circular polarizations before and after the focal plane. An accurate polarization setup is optimized to ensure the purest circular polarization for both orthogonal states at more than 97% at the focal plane on VODCA. In order to achieve this level of precision, two polarization measurement methods have been presented. The classical method and the rotating quarter wave plate (QWP) method. Both are used and compared to characterize how the polarization state of the light was impacted by the optical elements of VODCA. The rotating QWP method is used to optimize the accuracy of the circular polarizer being more precise and consistent than the classical method.

With the optimized circular polarizer, the dual polarization setup has been evaluated in terms of two particular performance values, the extinction ratio and the rejection ratio. The setup has achieved a non-expected high performance comparable to particularly efficient results obtained in previous studies. Considering the polarization setup without the AGPM, an extinction ratio of 1924 has been achieved. Due to intrinsic performance of the AGPM, the setup with the vortex coronagraph has achieved an extinction ratio of 1521. Moreover, a rejection ratio of 2010 has been obtained for the AGPM. This result has been obtained using a aberration minimization routine to avoid limiting performance due to aberrations in the focal plane. The total contrast achieved by the dual-polarization setup is up to 21e4.

These performance ensured a sufficiently high accuracy of the setup to produce a required diversity for phase retrieval. This produced diversity has been proven by using the deformable mirror (DM) of VODCA to inject specific aberrations in the focal plane and verify the lifting of the sign ambiguity which was confirmed. Following this, some CNN training on aberration identification have led to relative successful wavefront reconstruction tests performed using machine learning.

The dual-polarization setup developed in this work combined with the polarization behaviour of the phase mask allows a sufficient diversity to ensure a performing phase retrieval. However, these results are still preliminary in sight of a laboratory validation of the dual-polarization wavefront sensing using the vortex coronagraph.

Contents

List of Figures

List of Tables

Part I

Context and main goals of this work

1. Context

This work lies in the major challenge of the high-contrast imaging. The direct detection of celestial objects is made particularly difficult by the important flux ratio and the really small angular separation between the faint source, such as Earth-like exoplanets, and their host star. The contrast can be about 10^{10} in the visible. Coronagraphy is used to carry out this issue by a high attenuation of the star light to be able to detect planetary companions in the circumstellar environment.

Several coronagraphic solutions have been developed over the years until the proposition of the Annual Groove Phase Mask (AGPM) in 2005 [15][5]. Since then, the study and development of the AGPM is one of the main objective of the VORTEX project [14]. The AGPM is a Vector Vortex Coronagraph (VVC) which corresponds to an optical vortex created from subwavelength grating. The concept of the vortex coronagraph came from the need of an achromatic behaviour and a continuous phase shift without any dead zone contrary to a previous concept of phase mask, the Four Quadrants Phase Mask (FQPM) [15][14]. These improvements with respect to previous phase masks, and coronagraphic concepts in general, make the AGPM one of the leading designs in the field of exoplanet imaging. The AGPM performance has already been demonstrated in several contexts and in different bands, first in near infrared (NIR) H-band and K-band, in mid-infrared (MIR) L-band using YACADIRE[1] test bench and in MIR L-band using VODCA test bench [30][4][1]. The last results using the AGPM on VODCA in MIR will be used as reference in this work since all the measurements are made on VODCA test bench in the same band.

Besides the high contrast and narrow angular separation which are handled by the coronagraph, the direct imaging of an exoplanet is also limited by residual wavefront aberrations and in particular non-common path aberrations (NCPAs). Adaptive optics (AO) system using focal-plane wavefront sensing (FPWFS) is used in this particular context to handle these NCPAs. Machine learning algorithms using convolutional neural networks (CNNs) are developed to apply to phase retrieval [33][10]. However, these wavefront sensing algorithms need a certain diversity to lift potential phase ambiguities. To this outcome, the polarization behaviour of the AGPM is used to acquire sufficient diversity in the focal plane and retrieve the phase of the wavefront in the pupil plane [16]. This method is proposed by P. Riaud due to the simplicity of execution it features while minimizing the NCPAs. Moreover, it ensures a quasi-instantaneous phase retrieval. This method proposes to split the two orthogonal circular polarization states of the electric field. Without circular polarization splitter, this can be achieve by selecting one of the two orthogonal polarization states using a circular polarizer in a dual-polarization setup.

However, the circular polarizer needs a high level of accuracy to allow the highest confidence in the results. Several polarization measurement methods are presented in D. Goldstein

[1] YAmina CAlibration Detector Infra Red Euros is a test bench at the Paris Observatory.

[22] and two of them are detailed in B. Schaefer et al. [3]. These measurements allow to characterize the resulting polarization state of the light after passing through a polarizing element, or a specific part of VODCA test bench, using the formalism of the Stokes vector [18][22]. The impact of the different reflections can damage the input polarization state at a certain level [19],[23]. These polarization measurements will be used to ensure the most accurate dual-polarization setup.

The polarization measurements and the characterization of an accurate circular polarizer represent the biggest part of this work. The presentation of the configuration and features of VODCA test bench as it was used during this work needs a separate section before specifying the main objectives of the different parts of this study.

2. VODCA test bench

VODCA, which stands for Vortex Optical Demonstrator for Coronagraphic Applications, has been set up to assess the performance of phase masks in the infrared and in particular the vortex coronagraphs [25]. The test bench has evolved since its development in 2019 and a scheme of its final design which has been used in this work is depicted in Figure 2.1.

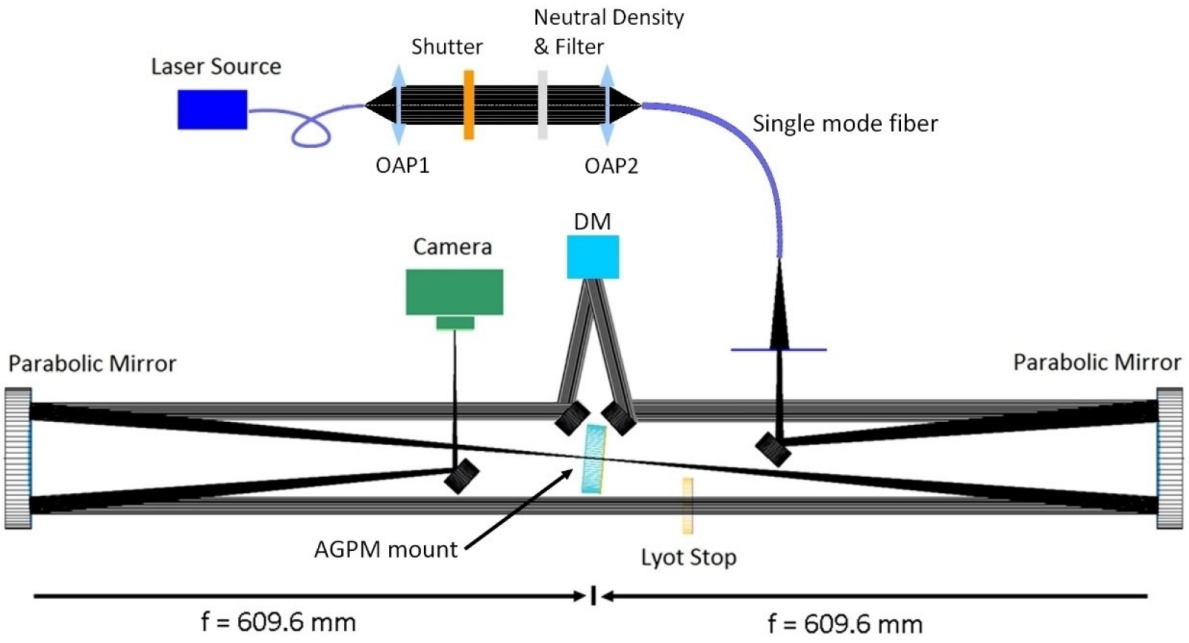

Figure 2.1: Scheme of VODCA setup [25]

The scheme is represented above to facilitate the understanding of the test bench but a picture of VODCA where different parts are highlighted is shown in Figure 2.2.

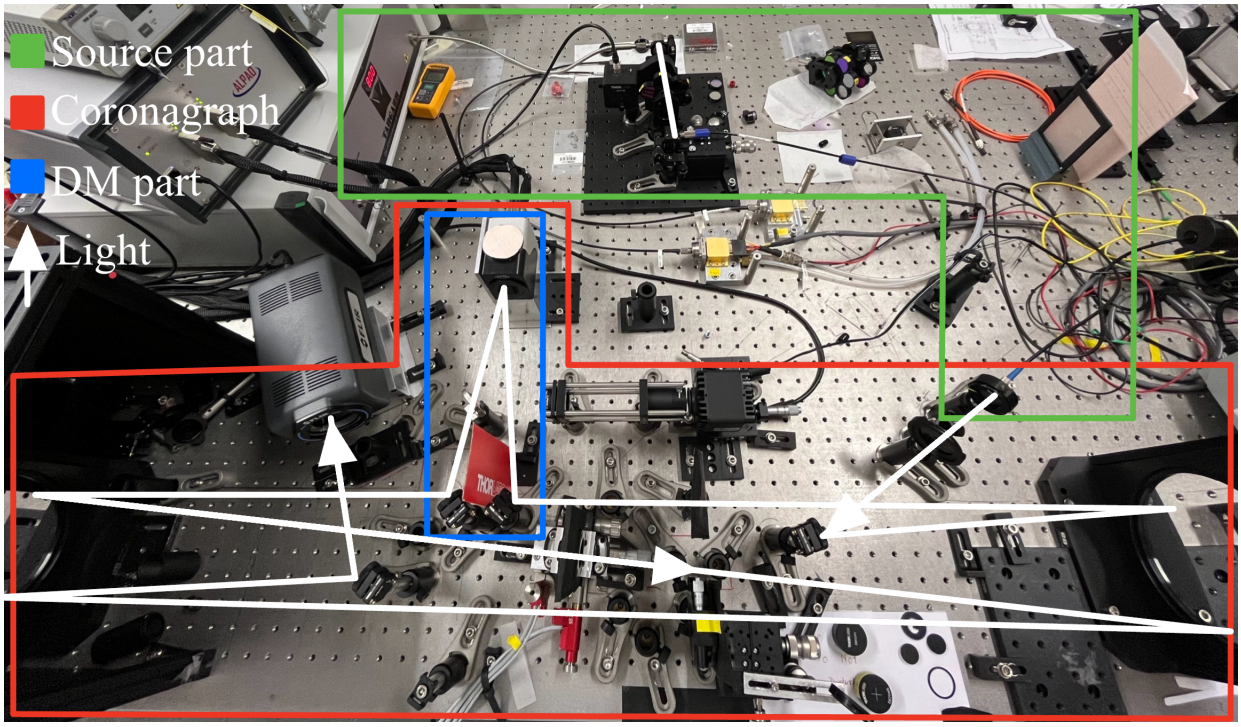

Figure 2.2: Picture of VODCA with the different parts represented.

In this picture, the part framed in green correponds to the source part, detailed in Section 2.1, composed of the laser source, two off-axis parabolas (OAP1 and OAP2), the shutter, the Neutral Density (ND) filter and the filter wheel. The light is then reinjected into a single mode (SM) fiber. The red part represents the main part of VODCA, the coronographic bench composed of the parabolic mirrors, the Deformable Mirror (DM), the AGPM mount, the Lyot stop and multiple wide angle mirrors. The DM part consists of two wide angle mirrors and the DM and is highlighted in blue in Figure 2.2. The different main parts of the test bench are now presented in the following sections.

2.1 Source part

The source of light used in the measurements is a SuperContinuum (SC) source from Le Verre Fluoré. It produces a continuum spectrum from 0.8 to 4 μm. The useful signal, particularly for polarization work, starts above 1.6 μm since the laser is multimode below this wavelength [25]. Therefore it covers H, K and L bands which correspond respectively to wavelengths from 1.44 to 1.77, 1.95 to 2.35 and 3.5 to 4.1. In particular, the band used for the measurements in this work is the L band. The working wavelength used as reference in this work is the design wavelength of the QWP which is 3800 nm.

The light is directed from the source to an OAP by a single mode fiber. The single mode fiber ensures to maintain the initial polarization state outgoing the laser and allows a aberration-free wavefront at the fiber outlet [25]. The source of light is easily interchange-

able by placing another optical fiber on the first mount. The beam is reflected by OAP1 and is directed to OAP2 as shown in Figure 2.1. In between, a shutter is placed to allow or not the light passing through. The shutter is used in VODCA to "acquire dark", which means taking an image of the background to remove it from the final image. This, as explained later, will be very useful in the measurements to get rid of the perturbations in the background when multiple images are acquired.

Just after the shutter, a rotative wheel can be placed to filter the light in the wavelength range desired in order to limit the width of the range and have less variations in the performance of the different compounds, such as the QWP in our measurements, as discussed in Section 7.1.2. Different filter wheels exist for the different bands. These rotating wheels are composed of a certain amount of filters with larger or narrower bandwidths. As the band used in the experiments is the L-band, six filters are available. The central wavelength and the bandwidth of four of them are resumed in Figure 2.3 hereunder.

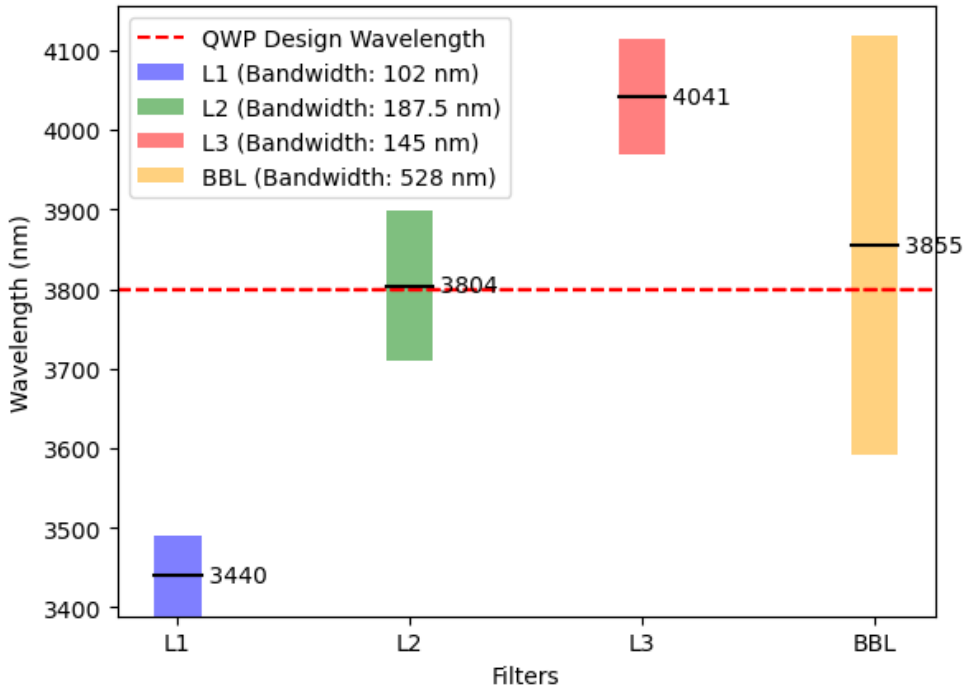

Figure 2.3: Filters bandwidth in L-band with respect to QWP design wavelength.

As represented on the graph, the working wavelength is included only in two filter bands, L2 and BBL. The choice of the filter will be justified when talking about the first results in Section 8.1.

Moreover, a ND filter can be fixed to either the shutter or the filter wheel mount. The ND is a filter with a specific transmission used to attenuate the intensity of the light coming from the source. Some ND filters attenuate more light than others.

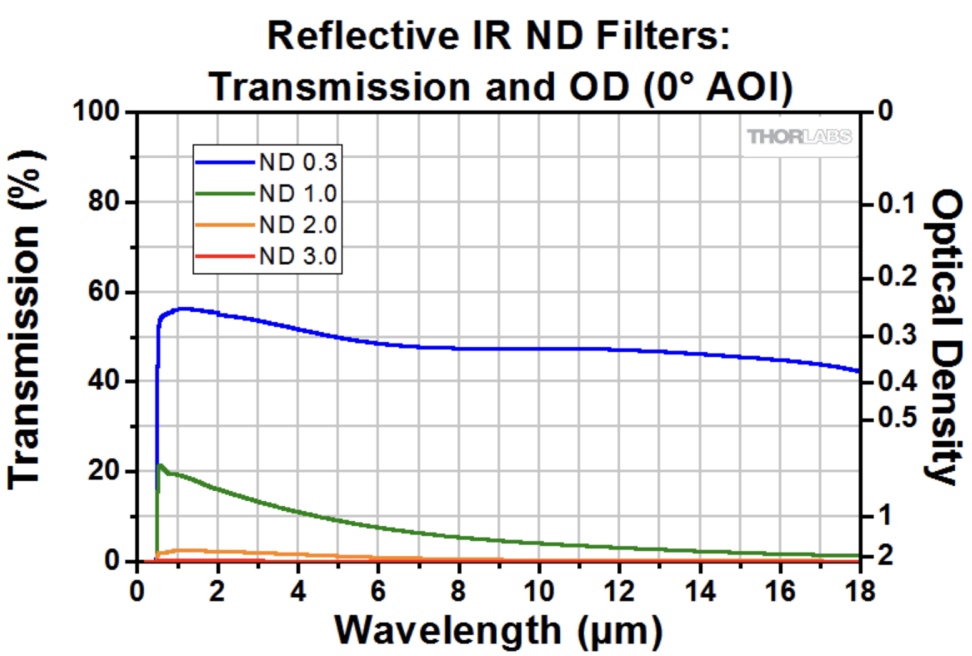

Figure 2.4: Transmission and optical density curves of Neutral Density filters.

As represented in Figure 2.4, different behaviours are linked to the different filters. At the working wavelength, around 3800 nm or 3.8 μm, the transmission is approximated by 10 to the power of minus the Neutral Density indice. Using ND 0.3, the transmission approaches $10^{-0.3}$, so 50.12%. With ND 1.0, the transmission is near 10%, with ND 2.0, 1% and with ND 3.0, 0.1. ND filters are used in particular to avoid saturation of the detector.

The light is then reinjected into an optical fiber as can be seen in Figure 2.1. After the source part, which ends at the outlet of the second single mode fiber comes the main part of VODCA which is characterized as the coronagraph part.

2.2 Coronagraphic part

The coronagraphic part is the main part in VODCA where the on-axis starlight will be cancelled. In telescopic applications, the on-axis starlight is cancelled in favour fo the off-axis light analysis. In this part, the light is reflected by three different types of mirrors. Four small mirrors with large angle reflections are used to redirect the light in the different parts of VODCA. Two large parabolic mirrors are used in two ways. On the one hand, the parabolic mirrors focus the light onto the focal plane and the image plane in the camera. On the other hand, they collimate the light beam before the pupil plane and the Lyot stop. The last mirror type is the Deformable Mirror (DM). All these reflections are represented in Figure 2.1. In Figure 2.5 is represented the typical arrangement of a coronagraph.

The black vertical arrows correspond to parabolic mirrors which focus and collimate the light. Concerning VODCA, the DM defines the pupil plane. The AGPM vortex is placed

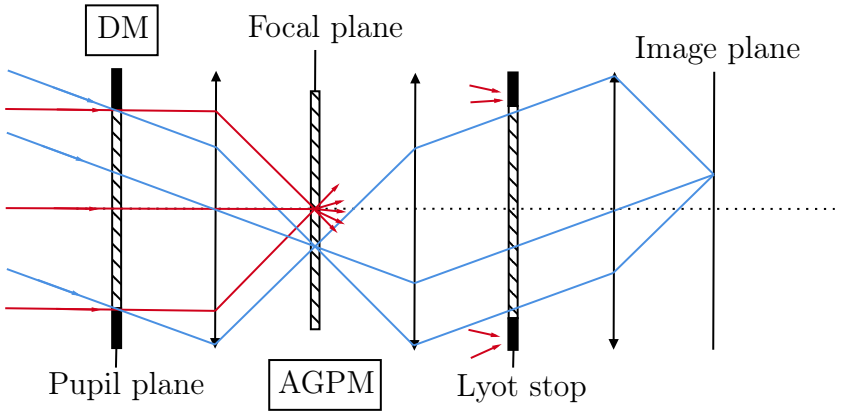

Figure 2.5: Overall structure of a coronagraph. Blue straight lines correspond to off-axis light (exoplanet light), red straight lines correspond to on-axis light (starlight). The centered dotted line corresponds to the optical axis. Vertical arrows are parabolas and vertical rectangle are optical planes. Inspired by schemes found in R. Galicher and J. Mazoyer [21].

in the focal plane where all the on-axis light is focused onto its center. The off-axis light is also focused in the focal plane but not on the center of the AGPM where the light is diffracted and therefore goes through. The Lyot stop, as shown in the scheme, is placed between the collimating parabolic mirror and the final reflection on the focusing parabolic mirror, which converges the light onto the image plane in the camera.

All the technical informations concerning the hardware of VODCA are taken from A. Jolivet [25].

2.2.1 The pupil plane - the deformable mirror

The deformable mirror is an active optical device which is used to compensate for static aberrations. In particular, one DM is used in VODCA to handle phase aberrations. It is an ALPAO DM with continuous reflective protected silver coated surface. The DM has an aperture of 13.5 mm and is composed of 97 actuators. This limited size aperture has the role of the input pupil. The DM is therefore used in wavefront sensing to induce phase shift to counterbalance phase aberration in order to obtain a flat wavefront and limit the perturbations induced by the aberrations. More than a correction role, the DM can also be used to induce aberrations and assess the impact of aberrations on the performances of the setup and in particular the AGPM. The DM is controllable using Python functions to induce aberrations by pushing the different actuators accordingly with a maximum total tip/tilt stroke of 60 μm [25][20].

Due to the reflections on the wide-angle mirrors and the complex shape and reflections on the DM, their effects on the polarization state of the light will be analyzed in the first part of Section II. Wide-angle reflections and reflections on coatings can impact the polarization of the incoming light.

2.2.2 The focal plane - the AGPM

The AGPM is a particular case of the Vector Vortex Coronagraph (VVC). Vectors vortex coronagraphs are one type of phase mask coronagraphs. These coronagraphs just as Lyot coronagraphs are placed in the focal plane. Their particularity is that they are transparent and induce phase shift that reject the on-axis light by destructive interferences. The on-axis light corresponds to the starlight which is diffracted by the phase mask and then is blocked by the Lyot stop as explained in Section 2.2.2. This is the vortex effect created by the AGPM.

It is a half wave plate with a spatially variant fast-axis orientation. A wave plate shifts the phase of a compoenent of the electric field of the light wave with respect to the other perpendicular component. In the case of the half-wave plate, the phase shift corresponds to π. Considering a linear polarized light, a halfwave plate has the effect of the rotation of the polarization by 90 degrees. And with circularly polarized light, the effect is to invert the polarization handedness. Right-handed polarized light is transformed into left handed polarized light and inversely. However, this effect is limited by the performance of the AGPM.

AGPM stands for Annual Groove Phase Mask. The AGPM, which is an optical vortex formed by a subwavelength grating, represents a cutting-edge coronagraph known for achieving high-contrast imaging at extremely small inner working angles (IWA) while maintaining high throughput across a complete 360-degree field of view. [4] The particularity

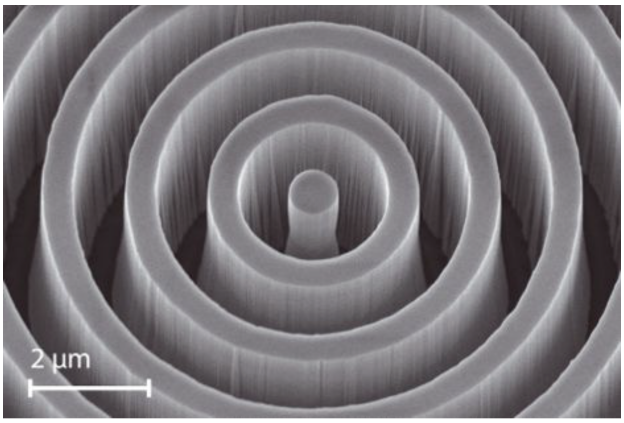

Figure 2.6: Scanning electron microscope (SEM) of an annular groove phase mask (AGPM) made out of diamond subwavelength grating [4].

of the VVC among the phase masks is that it features a continuous helical phase ramp that varies azimuthally around the optical axis. To have a better vizualization of the effect of the vector phase mask, the VVC may be represented using Jones matrices in the circular polarization basis. This representation is developed in Appendix A in Ruane et al. [7].

$$\mathbf{M} = c_V \begin{bmatrix} 0 & e^{il\theta} \\ e^{-il\theta} & 0 \end{bmatrix} + c_L \begin{bmatrix} 1 & 0 \\ 0 & 1 \end{bmatrix}, \tag{2.1}$$

where c_V and c_L are constants, θ is the azimuthal coordinate of the wave plate and l is called the charge and is a non-zero even integer. The fast-axis orientation, χ, is dependent on the azimuthal coordinate as $\chi = l\theta/2$. The first term corresponds to the part of the incoming light which undergoes the effect of the phase mask. The second term is called the leakage, which is the residue of the incoming light which didn't undergo the phase mask effect due to its imperfect retardance. The complex transmission $exp(\pm il\theta)$ is applied to both polarization components being the proportion of the LH and RH polarization in the circular polarization basis. The sign of this particular transmission term is dependent of the handedness of the circular polarization of the incoming light. Both component will be transformed to their orthogonal circular polarization state.

This behaviour of the phase mask with respect to the polarization justifies the need of selecting a circular polarization. In the circular polarization basis, a linear polarized light is composed of a combination of both circular polarization. Being affected by the vortex phase ramp will impact both components with an opposite sign ($exp(\pm il\theta)$) and another combination of both polarization state will be resulting after the phase mask. By selecting a specific circular polarization state, it allows the DM to find a configuration to attenuate the light intensity in the final image, which could be not possible with both circular polarization states present.

As stated in Ruane et al. [7], this issue and the potential stellar leakage lead to the setup with a circular polarizer (CP) before the AGPM and an analyzer after to be able to cancel the leakage, or in some cases, to select it in order to analyze and quantify it.

2.2.3 The Lyot Stop

The role of the Lyot stop is to block all (or most of) the on-axis light in order to allow high contrast imaging. It is made possible due to the vortex effect of the AGPM which diffracts the light focused on its center outside of the downstream pupil plane where the Lyot stop is placed. The on-axis light corresponds to the starlight, the light to cancel to be able to observe near potential celestial objects such as exoplanets. The Lyot Stop has a quite agressive effect to ensure the cancelling of the on-axis light since it blocks 20% of the collimated beam size after the AGPM [25].

2.2.4 Image plane - the camera

The FLIR A6700sc camera, which best matches the wavelength operating ranges of the SC, has been chosen. It features a detector array of 512x640 pixels, each with an individual size of 15 μm. The detector is sensitive to wavelengths ranging from the short end of the visible spectrum up to 5 μm. When the camera is switched on, it is cooled to 77 K to reduce the detector's background radiation. However, the downside of this routine is the 10 to 15 minutes required to reach 77 K and the vibrations from the built-in cooling system. These

vibrations are though minimized using a wide, sturdy mount. Integration times range from 480 ns to several seconds, typically set between 1 and 5 ms, with a frame rate up to 480 Hz. In full frame, when the camera captures images at maximum resolution, the frame rate is maximum 60 Hz.

The camera is a 14-bit operating dynamic range detector, meaning it can register intensity counts from 0 to 16384. However, as it has been seen during the measurements, the saturation of the image occurs whith counts higher than 8000. This can be observed in Figure 9.5. This upper limit is induced by the amplitude of the thermal background. The background image has most of its pixels with a intensity up to 8000, as it can be seen in the following example in Figure 2.7.

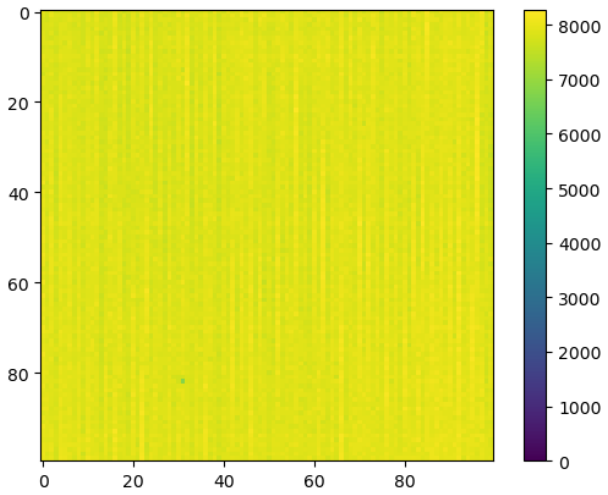

Figure 2.7: Typical thermal background image removed from the final image during processing.

By removing the background to the final image, the maximum intensity count, which was at 16384, occurs 8000 counts lower, around 8000. To avoid this issue, ND filters will be used during the measurements, as explained in Section 8.1.

3. Main objectives

The second part II of this work has two main objectives. The primary objective is to develop highly robust polarization measurement methods to ensure maximum confidence in the obtained results. The second goal is to characterize the effect of some specific parts of VODCA on the polarization of the incoming light going through all the system. This part of the work aims to be able to determine and ensure the purest circularly polarized light incoming to the focal plane onto the AGPM. To accomplish this goal, the polarization is measured at some specific positions. These particular setups will be detailed later. At the end of this part, the dual polarization setup will be created.
Two methods for polarization measurement are described in Schaefer et al.[3], the classical method and the method using a rotative quarter wave plate, which is called the rotating QWP method. Both methods will be used and compared.

The third part III aims to assess the performances of the setup in terms of extinction and rejection ratio. The extinction ratio of a polarization setup is evaluated by computing the contrast between a cross and a parallel polarizaton setup. The cross polarization setup corresponds to set a specific polarization state before the focal plane using a circular polarizer and by selecting the orthogonal polarization state after the focal plane using an analyzer. This contrast measure will give the performance of the polarization selection setup. The rejection ratio is computed as the contrast obtained by comparing the intensity measured when setting the AGPM outside the optical axis with the intensity obtained when the AGPM is centered with the optical axis. This will give the performance of the AGPM to reject the on-axis starlight. Both ratios will be compared and combined to characterize the total performance of the setup around the focal plane. This part aims to optimize the dual polarization setup to obtain contrast above 1:1000. The reference results used as performant results come from previous measurements made on VODCA with the same AGPM and filter [1].

The last part IV has the purpose of evaluate the expected consequences of the performant setup on the wavefront sensing. In particular, the diversity offered by the setup to effectively retrieve the phase of the wavefront is verified. The diversity is characterized by the difference in the aberration pattern with opposite sign or with orthogonal circular entrance polarization. More than that, wavefront reconstruction tests will be performed to evaluate the potential performance of the CNN to retrieve the aberration phase induced on the focal plane. This part will used the optimized setup obtained at the end of part III.

The general objective of this work is to search towards a performant dual-polarization setup for wavefront sensing especially in the sight of phase retrieval using the polarization features of the vortex coronagraph.

Part II

Polarization measurements

4. General concepts

4.1 Stokes formalism

The polarization state of the light can be characterized using different conventions. The one used in this work is the Stokes vector. The Stokes vector is composed of four parameters. The first parameter S_0 corresponds to the total intensity of the light. All four parameters are described in terms of intensities which are computed with squared amplitudes. S_1 corresponds to the preponderance of the horizontal linear polarization (S_1 = 1) over vertical linear polarization (S_1 = -1), S_2 represents the preponderance of the oblique linear polarized light at 45 degrees (S_2 = 1) over linear polarized light at -45 degrees (S_2 = -1). The last parameter, S_3 correponds to circularly polarized light and characterizes preponderance of right handed circular polarization (S_3 = 1) over left handed circularly polarized light (S_3 = -1). A specific condition on these parameters must be respected. The square of the total intensity must be higher or equal to the sum of the squares of the other parameters.
For a fully polarized light, the relation is :

$$S_0^2 = S_1^2 + S_2^2 + S_3^2. \tag{4.1}$$

For partially polarized light, the Equation 4.1 becomes the polarization condition,

$$S_0^2 \geq S_1^2 + S_2^2 + S_3^2. \tag{4.2}$$

The development to achieve this result is detailed in Schaefer et al. [3], but is summarized here below.
The light is characterized by two orthogonal compounds, E_x and E_y, given by :

$$\begin{aligned} E_x(z,t) &= E_{0x}\cos(\omega t - \kappa z + \delta_x) \\ E_y(z,t) &= E_{0y}\cos(\omega t - \kappa z + \delta_y), \end{aligned} \tag{4.3}$$

with E_{0x} and E_{0y} the amplitudes of the optical field, ω is the angular frequency, t is time, κ is the wave number and δ (δ_x and δ_y) is a phase constant.
In order to be able to represent the polarization behaviour of the light, the polarization ellipse is used and is defined as following:

$$\frac{E_x(z,t)^2}{E_{0x}^2} + \frac{E_y(z,t)^2}{E_{0y}^2} - \frac{2E_x(z,t)E_y(z,t)}{E_{0x}E_{0y}}\cos\delta = \sin^2\delta, \tag{4.4}$$

with $\delta = \delta_y - \delta_x$. By transforming the Equation 4.4 in the intensity domain to be able to measure it using a time average of the polarization ellipse, the Stokes vector are defined.

$$\begin{aligned} S_0 &= E_{0x}^2 + E_{0y}^2 \\ S_1 &= E_{0x}^2 - E_{0y}^2 \\ S_2 &= 2E_{0x}E_{0y}\cos\delta \\ S_3 &= 2E_{0x}E_{0y}\sin\delta \end{aligned} \tag{4.5}$$

This expression of the Stokes parameter gives the convention used for all this work. The handedness of the circular polarization is determined by the phase difference δ. A phase difference of $\pi/2 + 2m\pi(m = 0, \pm1, \pm2, ...)$ leads to a right-handed circular polarization state while a phase difference of $3\pi/2 + 2m\pi(m = 0, \pm1, \pm2, ...)$ gives a left-handed circular polarization. This is the convention used in many reference books such as Born and Wolf [18], Hecht [24] and Goldstein [22] which is referred in Schaefer et al. paper [3].[1]

The vector composed of these four parameters represents the general form of the Stokes vector and corresponds to an elliptically polarized light. When the condition from Equation 4.1 is respected, the vector represents completely polarized light. The Stokes vector can also characterize partially polarized light. The degree of polarization of the light represented by the letter P, can be computed using its definition :

$$P = \frac{I_{ELP}}{I_{TOT}} = \frac{\sqrt{S_1^2 + S_2^2 + S_3^2}}{S_0}, \quad (0 \leq P \leq 1). \tag{4.6}$$

I_{ELP} is the intensity of the elliptically polarized light and I_{TOT} is the total intensity of the light. The degree of polarization between 0 and 1 characterizes a partially polarized light which can be seen, as stated in Schaefer et al. [3], as a mixture of unpolarized light (UNP) and completely polarized light. This is described as following :

$$S = \begin{bmatrix} S'_0 \\ S'_1 \\ S'_2 \\ S'_3 \end{bmatrix}_{PP} = (1 - P) \begin{bmatrix} S_0 \\ 0 \\ 0 \\ 0 \end{bmatrix}_{UNP} + P \begin{bmatrix} S_0 \\ S_1 \\ S_2 \\ S_3 \end{bmatrix}_{ELP} \tag{4.7}$$

In most cases, the measured light will be characterized as partially polarized due to the inherent limitation of the compounds and the imperfections in the setup manipulations and measurements.

4.2 Classical method

The classical method needs four measurements of the light to determine the Stokes parameters. This measurement method uses an analyzer composed of a quarter wave plate (QWP) and a linear polarizer (LP) with a polarized source. The specific optical element or setup to analyze is placed in between. A scheme of the general setup used for this method is depicted in Figure 4.1.

In fact, the intensity of the light can be stated as :

$$I(\theta, \phi) = \frac{1}{2}(S_0 + S_1 \cos 2\theta + S_2 \sin 2\theta \cos \phi - S_3 \sin 2\theta \sin \phi), \tag{4.8}$$

[1] Actually, Schaefer reffers to the first edition of Polarized Light written by Edward Collet. This book has been reedited twice (revised and expanded) by Dennis Goldstein (2003, 2011) and the second version is used as reference in this work.

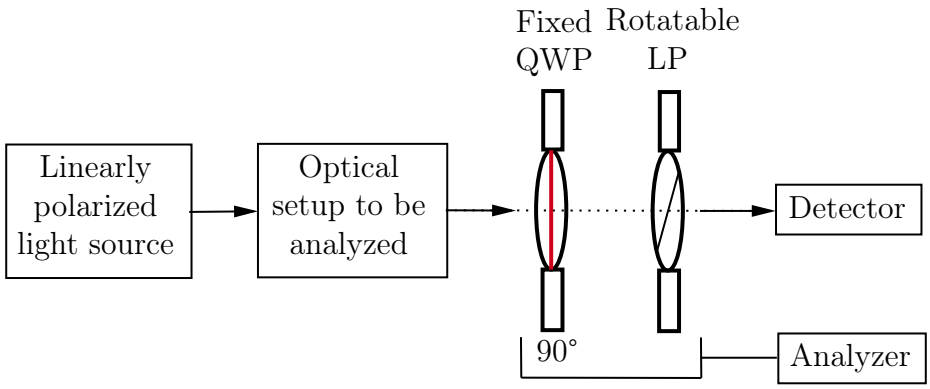

Figure 4.1: Classical method general setup. The black arrows represent the light flux.

with θ the angle of the polarizer and ϕ the angle of the quarter wave plate. The four Stokes parameters being the unknown, four equations are necessary to determine them. Schaefer adapted the expression of the intensity of the light presented in Goldstein [22] to be consistent with the convention precised in the previous section. The expression developed in Goldstein [22] gives an opposite sign for the term corresponding to the fourth parameter in Equation 4.8. This results in opposite sign for the fourth parameter as developed in Equation 4.9 and it does not follow the definition of the handedness of the circular polarization defined earlier. A right-handed circular polarization as defined in Section 4.1 gives [1 ; 0 ; 0 ; 1] using Schaefer formalism and [1 ; 0 ; 0 ; -1] with Goldstein formalism.

The four Stokes parameters can be determined with the four following measurements. The first three measurements are made with the polarizer at 0, 45 and 90 degrees. In Schaefer et al. [3], it is specified that these three first measurements can be made without the quarter wave plate. In addition to that the notation of the values *I(90,0)* suggests that all the measurements could be made with the same setup, so with the QWP placed before the LP, but with the QWP at 0° for the three first measurements. The first results were inconsistent because, with respect to the light source polarization, a QWP at 0° has not at all the same effect than no QWP. This obvious mistake has been quickly solved and these wrong results do not appear in this work due to their irrelevance. But this mistake is mentionned here to note that the three first measurements must be done without the QWP and the notation with $\phi = 0°$ (e.g. *I(90,0)*) means that the QWP is not used.

The QWP is made of a birefringent material and has two specific axis, the fast axis and the slow axis. Both axis will delay the component of the electric field which is parallel to them but with a phase retard difference of a quarter of the wavelength, in the case of the QWP. When the incident light is linearly polarized at a specific orientation which is parallel or perpendicular to the fast axis of the QWP, the light wave will be delayed by a specific phase retard but the polarization state won't change. However, if the orientation of the linearly polarized light has a non-zero angle with respect to both QWP axis, the phase retard will induce a non-negligible change in the polarization state of the light. The measurements with the LP at 0° and 90° could actually be performed with the QWP at 0°, but this is not the case of the measurement including the LP at 45°. To avoid any perturbations, the

quarter wave plate is added only for the last measurement with the polarizer at 45 degrees and the quarter wave plate at 90 degrees, where it is actually necessary. The Stokes vector is then obtained with :

$$\begin{aligned} S_0 &= I(0°, 0°) + I(90°, 0°) \\ S_1 &= I(0°, 0°) - I(90°, 0°) \\ S_2 &= 2I(45°, 0°) - S_0 \\ S_3 &= S_0 - 2I(45°, 90°) \end{aligned} \tag{4.9}$$

For a better vizualization of the polarization state, the different elements are normalized over S_0 which corresponds to the maximum intensity. The results obtained in this work are represented by the normalized Stokes vector given by :

$$S = \left[1\,;\, \frac{S_1}{S_0}\,;\, \frac{S_2}{S_0}\,;\, \frac{S_3}{S_0}\right] \tag{4.10}$$

4.3 Rotating quarter wave plate method

The second method offers theoretically a better accuracy due to the larger amount of data points used. In this setup, a rotating quarter wave plate is used upstream a fixed linear polarizer at 0 degrees. The corresponding setup is depicted in Figure 4.2. The difference

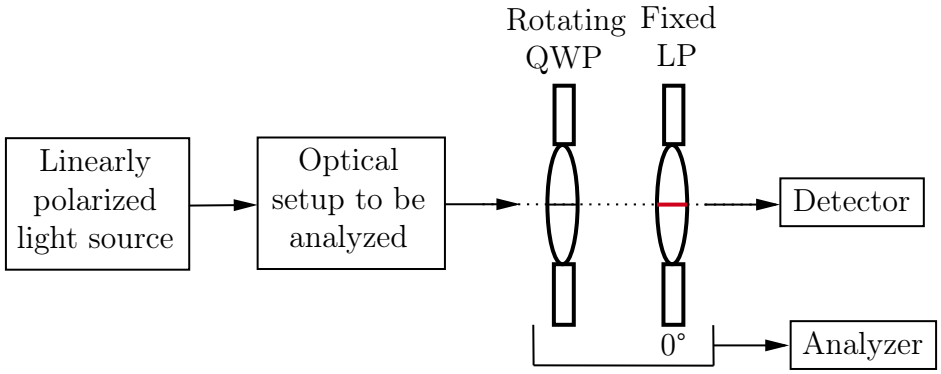

Figure 4.2: Rotating QWP method general setup.

with the setup represented in Figure 4.1 is the use of both compounds (QWP and LP) for each measurement. Moreover, the LP is fixed for all measurements and the QWP is mounted on a motorised rotating mount which can be precisely rotated using a software linked to the mount.

For the sake of clarity, the angle of the QWP is denoted as ϕ, just as in the classical method, contrary to the notation used in Schaefer et al. [3]. As for the classical method, Schaefer adapted the expression of the intensity of light to correspond to the convention

used. However, the sign of the fourth Stokes parameter in Equation 4.11 is not considered in the expression of the parameter B in 4.13. This is fixed in this work to remain consistent with the convention used. The intensity measured by the camera can be described by :

$$I(\phi) = \frac{1}{2}(S_0 + S_1 \cos^2 2\phi + S_2 \cos 2\phi \sin 2\phi - S_3 \sin 2\phi). \tag{4.11}$$

This expression comes from the multiplication of the Muller matrix of a rotated quarter-wave plate retarder with the Muller matrix of a linear horizontal polarizer. This is developed in Goldstein [22]. Muller formalism will be presented and developed in the context of the imperfections in the setup and inherent variations of the retarder and the polarizer and their impacts on the polarization state measured.

The expression from 4.11 can be rewritten in the following form to get rid of the second order terms:

$$I(\phi) = \frac{1}{2}(A + B \sin 2\phi + C \cos 4\phi + D \sin 4\phi), \tag{4.12}$$

with

$$A = S_0 + \frac{S_1}{2}, \quad B = -S_3, \quad C = \frac{S_1}{2}, \quad D = \frac{S_2}{2}. \tag{4.13}$$

In order to define how many data points are necessary to determine the four parameters (A,B,C and D), the Nyquist sampling theorem is used. This theorem states that "a periodic signal must be sampled at more than twice the highest frequency component of the signal" [28]. The highest frequency component in the expression of the signal being 4ϕ, the minimum number of data samples is therefore 8. The expression of the intensity obtained can be written again as a discrete quantity :

$$I_n = \frac{1}{2}(A + B\sin 2\phi_n + C\cos 4\phi_n + D\sin 4\phi_n) \tag{4.14}$$

with n the number of the sample. By developing the mean intensity over N data samples, which is minimum 8, and using methods from Fourier analysis, the four parameters can be expressed and computed using the results obtained for each data sample. The four parameters are determined as follows:

$$\begin{aligned} A &= \frac{2}{N}\sum_{n=1}^{N} I_n, \quad B = \frac{4}{N}\sum_{n=1}^{N} I_n \sin 2\phi_n, \\ C &= \frac{4}{N}\sum_{n=1}^{N} I_n \cos 4\phi_n, \quad D = \frac{4}{N}\sum_{n=1}^{N} I_n \sin 4\phi_n, \end{aligned} \tag{4.15}$$

with N the total number of data samples. This development allows to compute the four Stokes parameters using the relations in Equation 4.13:

$$S_0 = A - C, \quad S_1 = 2C, \quad S_2 = 2D \quad \text{and} \quad S_3 = -B. \tag{4.16}$$

In theory, the Stokes vector will be more precise if many data samples are used. But it must be a compromise between the time taken to execute the measurement method and the precision of the results needed.

As the intensity curve has a period of π, the N data samples can be fixed between 0 and 180 degrees with regular intervals between the angles.

5. Acquisition method

The measurements are made with the two methods presented before but the way to acquire the images for each measurement has also to be determined. The way the images are collected and saved for each measurement corresponds to the acquisition method.

5.1 Python interface

The bench is connected to the computer and some of its features can be handled using a custom-made software and functions in Python. Different classes already existing in the software are used to control some of the main components of the bench. These main elements are the shutter, the deformable mirror and the camera. In order to be able to use the rotating QWP method, another class has to be added to create functions able to control the motorised mount. A separate software from Thorlabs already exists to control the mount, the Kinesis software. However, in order to automate its control, a class must be added in Python which uses the same control as the Kinesis software. The rotating mount is the Stepper Motor Rotation Mount by Thorlabs represented in Figure 5.1. The rotating

Figure 5.1: Stepper Motor Rotation Mount by Thorlabs.

mount interface is created and uses basic functions provided by Thorlabs and also used in the Kinesis software. This class is added in the library of already existing classes to control the different features of VODCA.

Python scripts are therefore created to collect the images captured by the camera and save them in data cubes. To be able to control the different features and acquire a large amount of images while limiting the acquisition time, it is necessary to acquire the data using Python scripts. One script is created for each measurement method. These acquisition methods are progressively improved and optimized.

5.2 Background substraction

At first the acquisition method simply corresponds to take a snapshot of the final image obtained for each measurement and compute the mean intensity measured in the image as the intensity needed for determining the Stokes parameters. This method appears to be very limited and dependent on the small variations of the source and perturbations in the thermal background. The source being not completely stable, perturbations on the final results are quickly observed to conclude that longer measurements and larger data averages are needed to have more trustworthy results.

Different parameters have to be improved to have more precise results. The first idea is to get rid of the perturbations of the background. This is first handled during the data processing as explained in next section, Section 8. This is done using an aperture mask created on the final image. However, an aperture mask is not enough to get rid of the perturbations of the background. In order to be less sensitive to the background and to small perturbations, the intensity measurements are made by means of a large amount of images and by removing from each of these images the corresponding background.

5.2.1 Classical method

The acquisition method is slightly different for the two methods but the idea is the same. Concerning the classical method, 1000 pairs of background (with the shutter closed) and images (with the shutter open) are taken. In a 1000 iteration loop, first the shutter is closed and the resulting image on the camera is acquired and then the shutter is opened and a new image is saved. Two data cubes are resulting, 1000 background images and 1000 open-shutter images. During the processing, each background image corresponding to an open-shutter image is removed from it to get rid of the background perturbations. This is the most accurate in theory but the acquisition is very time consuming. In order to save some iteration time, the acquisition is summarized to a ten iteration loop saving first 100 background images and then 100 corresponding open-shutter images. This is the acquisition process for the classic polarization measurement method. This acquisition method is therefore repeated four times, one for each measurement [I(0,0),I(90,0),I(45,0),I(45,90))].

5.2.2 Rotating QWP method

Considering the rotating QWP method, minimum 8 measurements are necessary as explained in Section 4.3. These measurements are data points in the signal function of the intensity with respect to the QWP fast axis orientation and more data points lead to more accuracy but require more time. At first, only the minimum eight measurements are done to save time. At each data point, 100 background images and 100 open-shutter images are acquired and as before, the backgrounds are removed from the images. The eight measurements of the second method in one script execution are made possible using the rotating mount interface, which rotates the mount between each measurement using the corresponding function.

5.2.3 Comparison

If the two acquisition methods are compared, 1000 pairs of images and background are acquired for each measurement in the classical method while 100 pairs are acquired for each measurement during the rotating QWP method. This difference is selected due to the potential high number of measurements needed depending on the number of data points chosen in the second methods. Since more data points are naturally increasing the iteration time, 100 pairs of background and open-shutter images seem then to be sufficient. This is therefore a lot faster than the classical method at first but the number of data points can be increased to improve the accuracy. The rotating QWP method uses a rotating mount which can be controlled using Python functions and so is automated unlike the classical method which needs manual rotation of the linear polarizer mount and the setting up of the quarter wave plate for the last measurement. The classical method has then a higher acquisition time. More than that, some inaccuracies are introduced due to the manipulations required between each of the four measurements, whereas the only manual verification needed for the rotating QWP method is the determination of the reference angle on the mount with respect to the fast axis of the QWP. Even though, each reference angle, which is the horizontal angle on the corresponding mount which matches the fast axis for the QWP and the transmission axis for the LP, is verified using a highly precise height indicator.

6. Processing method

During the processing, as mentioned in previous Section 5, the data cubes obtained during the acquisition are handled. The corresponding background frames are removed from each open-shutter image. After that, the photometry is performed in the final image. The photometry gives the corresponding intensity value for each measurement which will be used for Stokes parameter computation. Nonetheless, in order to obtain an accurate intensity values, not all the information in the final image must be considered.

6.1 Photometry

The photometry corresponds to how the value of intensity will be determined to compute the Stokes vector. In the final image, each pixel has a different intensity value. Multiple statistic methods exist to compute a single intensity value for the entire image. Among them the mean, the median, the sum and the maximum.

The maximum would give too little information about the intensity distribution in the image and is not considered. The mean and the sum would give the same information about the image, since the mean is only the sum divided by the number of pixels, with the disadvantage to the sum to work with potential very high values. More than that, the mean is more sensible to extreme values while the median is only the center value in an increasingly ordered list of all the intensity values in the image. The median is then theoretically more robust with respect to detector effects such as hot pixels since it makes the intensity value used more resilient against extreme values that might occur in the distribution of the Power Spread Function. Some preliminary measurements have been made to reinforce the choice of the median over the mean but the results gave not enough informations to prefer one photometry method. Due to its more important theoretical robustness, the median is used as photometry method in this work to compute the Stokes vectors.

6.2 Aperture mask

The idea is to get rid of the perturbations in the final images including straylight and ghosts due to unintented reflections or other perturbations. With this intent, a mask is created to consider only the pixels inside the mask. At first the radius is arbitrarily determined from 10 to 15 pixels to include most of the information of the PSF. Nevertheless, during the processing, to improve the accuracy of the results and to be rigorous, the radius must be determined based on the size of the PSF. The radius of the mask is determined by fitting a gaussian function to the obtained PSF and limiting the radius to the radius of the Airy disk. The latter is the distance between the maximum of the function and the first

minimum. This particular distance is determined by:

$$\theta = 1.22 \frac{f \lambda}{d}, \tag{6.1}$$

with f the focal distance, λ the wavelength and d the aperture diameter. The focal distance corresponds to 609.6 mm which is the distance between the focusing parabolic mirror and the focal plane (which is the same distance between the focal plane and the defocusing parabolic mirror) as it is represented in Figure 2.1. The center wavelength of the light emitted by the source is near 3800 nm because the band used is the L-band (more or less between 3.4 and 4.1 μm). The wavelength range used in our measurements is even closer to this center wavelength since the L2 filter is used which is the most narrow filter with a wavelength range from 3710.25 to 3897.75. The aperture diameter is given by the aperture in the pupil plane which corresponds to the diameter of the DM. The diameter of the DM is 13.5 μm. The Airy disk radius is then 2.093×10^{-4} mm. The size of the pixels in the camera corresponds to 15 μm. The aperture mask radius is therefore determined to 13.956 pixels, so 14 pixels. This is valid when acquiring an image obtained with light going through all the system because the light beam is focused in the image plane.

However, this development does not take into account the effect of the Lyot stop. Actually, as mentioned in 2.2.3, the Lyot stop reduces the collimated beam size by 20% and therefore increases the Airy disk raidus in the image plane by a factor 1.25 as the Airy disk radius is inversely proportional to the pupil plane diameter. Following the justification above, this results in a distance of 17.445 pixels in the camera, so an aperture mask radius of 18 pixels. But all the following results are obtained using an aperture disk with a radius of 14 pixels, this mistake in the development being noticed at the end of this work. This development error might have led to choose a better solution for the mask radius than the Airy disk radius. A narrower aperture is indeed more robust againt background perturbations and variations that can appear near the first minimum of the PSF. More that that, an aperture mask of 14 pixels can provide enough information about the PSF shape. An example of the use of such a mask on an image with a PSF is represented in the Figure 6.1.

In the first Subfigure 6.1a, the PSF pattern is clearly represented with the first maximum at the center of the image and the second lower maximum around. This kind of image is obtained when the light is collimated after passing through the all system. In the second Subfigure 6.1b, the aperture mask is applied with a radius of 14 pixels as computed earlier. Only the first maximum is considered in this image.

For the first measurements, VODCA is not considered in all its parts, the optical fiber being placed just before the camera as it is depicted in Figure 8.1. With this first setup, the light is not focused and the image obtained is much larger than the PSF resulting from the diffraction pattern of the focused light. With the original setup of VODCA, the image fits in a 100×100 pixels; in short-circuit configuration, the image must be at least 400×400 pixels. This type of image is shown in Figure 6.2.

As seen in Figure 6.2, the light beam is not focused and the PSF is not observable in this

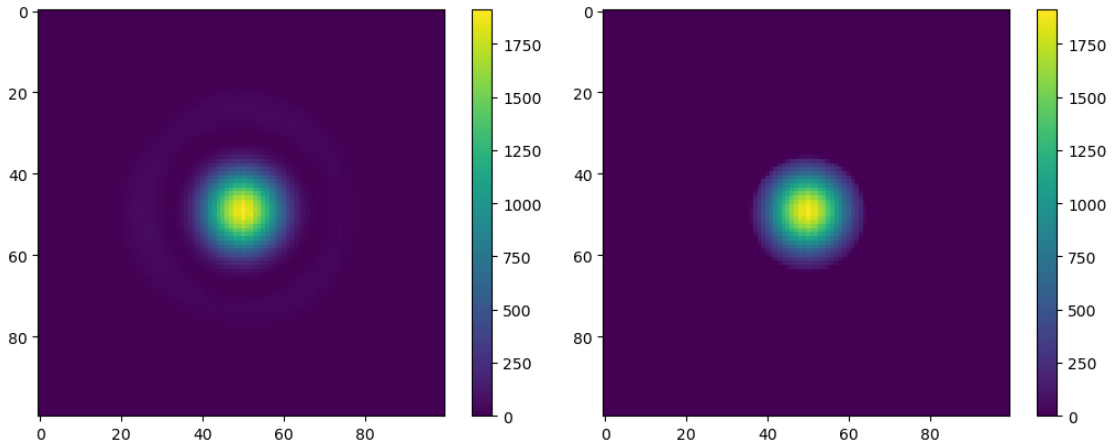

(a) Image without aperture mask applied. (b) Image with the aperture mask applied.

Figure 6.1: Comparison between the image without the aperture mask (left) and with the mask applied (right). Mean image sampled from a left-handed circular polarization measurement at the focal plane of VODCA 9.1 using the rotating QWP method with 8 data points.

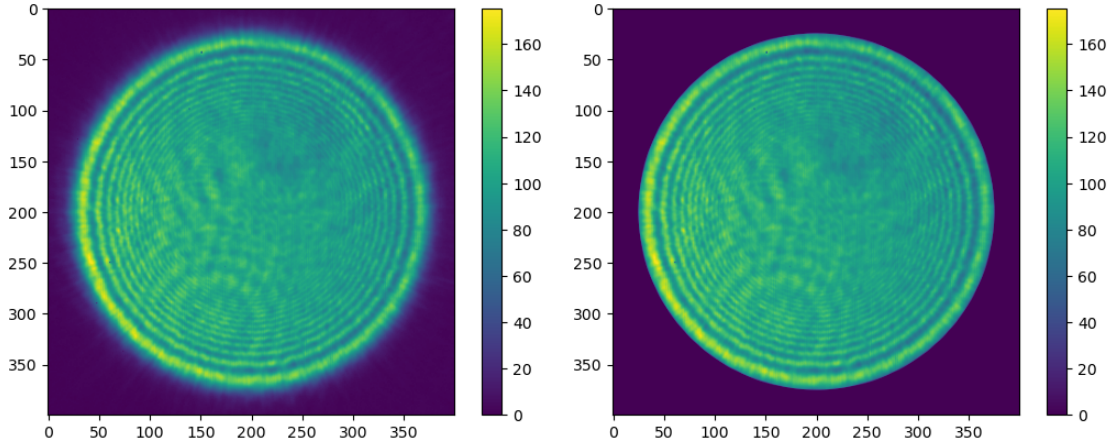

(a) Image without aperture mask applied. (b) Image with the aperture mask applied.

Figure 6.2: Comparison between the image without the aperture mask (left) and with the mask applied (right). Mean image sampled from the linear polarization measurement in short-circuit of VODCA 8.1. It corresponding to the first measurement of the classic method, with the LP oriented to 90° without the QWP placed.

image. This kind of image is obtained when measuring the polarization in short-circuit of VODCA. The aperture mask applied during processing is wider since the light is not focused and has less impact. However, the aperture mask is less necessary in this type of images since it leaves less room to some perturbations. The pattern in this case being wider, the image size is set to 400×400 compared to images including the PSF which have the size of 100×100. As it does not represent the PSF, the first maximum is not as easily isolated. However, in order to be rigorous, the aperture mask is added in every image, and

in the case of the 400×400 images, its radius is more arbitrary. In the example of the Figure 6.2, it corresponds to 175 pixels, to include the entire circular pattern.

It is important to consider only the pixels inside the mask to compute the intensity of the light, especially when computing the photometry in order not to be biased by a lot of pixels set to zero which can greatly impact the final value. This processing method is common to the different measurement methods and to all measurements from results summarized in Table 8.3.

7. Potential sources of inacurracies

As it will be observed in measurements in the following section, the polarization state measured is rarely as pure as expected. The polarization state measured is limited and impacted by several parameters and features described in this section.

7.1 Inacurracy of the setup - Muller formalism

The accuracy of the linear polarizers and the quarter wave plate are limited and can be estimated using Muller formalism. The limitations on the performance of the LP and the QWP come from an intrinsic imperfection, a non-perfect linear polarizer or a non-perfect retardance from the QWP. These are internal limitations. Other limitations come from the inaccuracy on the orientation of the transmission and the fast axis. These are external limitations. Although the last measurements represent with more accuracy the desired polarization, the early results which differ more from the polarization state sought can be explained with this study.

Muller formalism is used to characterize the impact or the effect of a polarizing element on the Stokes vector representing the polarization state. If S is the initial Stokes vector and M the Muller matrix representing a particular polarizing element, the resulting Stokes vector S' is computed as following, as presented in D. Goldstein [22],

$$S \,.\, M = S', \tag{7.1}$$

which can be written in the matrix form,

$$\begin{pmatrix} m_{00} & m_{01} & m_{02} & m_{03} \\ m_{10} & m_{11} & m_{12} & m_{13} \\ m_{20} & m_{21} & m_{22} & m_{23} \\ m_{30} & m_{31} & m_{32} & m_{33} \end{pmatrix} \cdot \begin{pmatrix} S_0 \\ S_1 \\ S_2 \\ S_3 \end{pmatrix} = \begin{pmatrix} S'_0 \\ S'_1 \\ S'_2 \\ S'_3 \end{pmatrix} . \tag{7.2}$$

Any polarizing element can be represented by a matrix in the Muller formalism. General matrices exist for LP and QWP and will be presented in the two following sections.

7.1.1 Linear polarizer

A perfect horizontal LP is charaterized using Muller formalism as following.

$$M_{LP} = \frac{1}{2} \begin{pmatrix} 1 & 1 & 0 & 0 \\ 1 & 1 & 0 & 0 \\ 0 & 0 & 0 & 0 \\ 0 & 0 & 0 & 0 \end{pmatrix}, \tag{7.3}$$

Any random normalized Stokes vector multiplied by this matrix will result in a horizontal polarization state vector : [1 ; 1 ; 0 ; 0]. However, in reality the LP is always imperfect due to internal characteristics or external inaccuracies.

The analysis is first focused on the inherent performance of the LP with respect to its transmission and extinction ratio performance provided by Thorlabs shown in Figure 7.1.

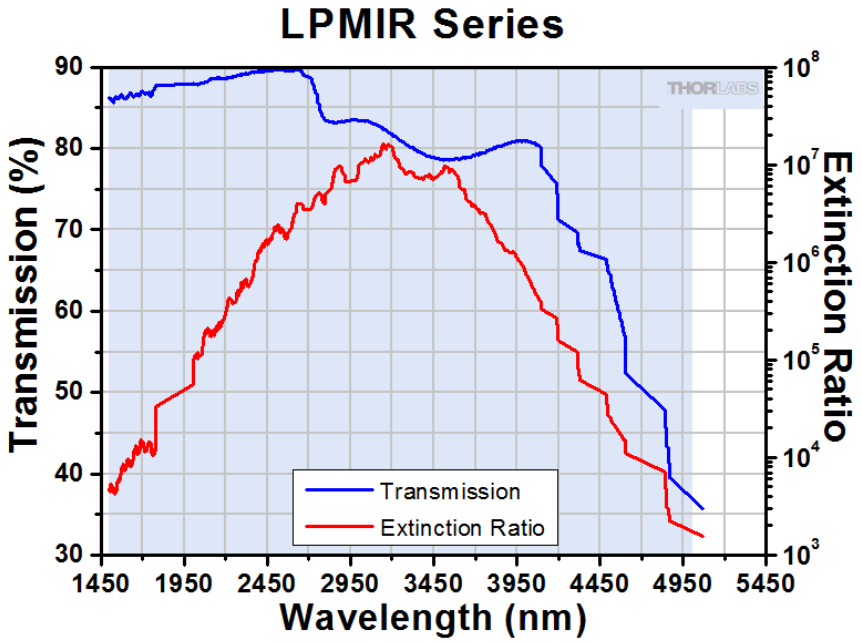

Figure 7.1: Transmission and exctinction ratio of the LPMIR from Thorlabs.

These performances correspond to LPMIR polarizers in general, the LP used in the measurements is the LPMIR100-MP2 which is one specific type. The performances can vary a little from one model to the other but the performances given in Figure 7.1 represent a good generalization. The performances are analyzed at the design wavelength of the QWP (3800 nm) which is the work reference wavelength for measurements in this work, and at limit wavelength admitted by the L2 filter (at $3804 \geq 93.75$ nm).

To be able to observe the effect of a non-perfect LP, the following matrix is used [22][26].

$$M_{LP} = \frac{1}{2}\begin{pmatrix} p_x^2 + p_y^2 & p_x^2 - p_y^2 & 0 & 0 \\ p_x^2 - p_y^2 & p_x^2 + p_y^2 & 0 & 0 \\ 0 & 0 & 2p_x p_y & 0 \\ 0 & 0 & 0 & 2p_x p_y \end{pmatrix}, \tag{7.4}$$

with p_x and p_y the transmission factors for x and y-component of the electric field. The two unknows, p_x and p_y are determined using two specific values which are represented in Figure 7.1, the transmission and the extinction ratio. The transmission from Thorlabs corresponds to the transmittance k in C. U. Keller [26] which is given by the square of the

transmission ratio p,

$$\begin{aligned} k_1 &= p_x^2 \\ k_2 &= p_y^2. \end{aligned} \tag{7.5}$$

As the transmission is defined in Thorlabs by "the percentage of light with a linear state of polarization (SOP) aligned with the transmission axis that is transmitted through the linear polarizer", it corresponds to a factor on the intensity of the light, which corresponds to the k factor. In particular, it relates to k_1 factor because it is question of maximum intensity. k_1 is indeed defined with "transmittance for fully linearly polarized beam at angle that maximizes transmitted intensity" [26]. With these definitions, the matrix represented in Equation 7.4 actually represents a non-perfect linear polarizer with $p_x > p_y$, with the transmission axis aligned with the horizontal.

With the transmission given in Figure 7.1, p_x is then determined and using the definition of the extinction ratio, $ER = \frac{k_1}{k_2}$, p_y can also be determined. Using the values given with the graph, and by interpolation, the values for p_x and p_y are given for 3800, 3710.25 and 3897.75 nm are given in Table 7.1.

Transmission factor	Wavelength [nm]		
	3710.25	3800	3897.75
p_x	0.894	0.891	0.898
p_y	$0.583e^{-3}$	$0.472e^{-3}$	$0.782e^{-3}$

Table 7.1: Values of p_x and p_y for limit wavelengths allowed by L2 filter and QWP design wavelength.

By using these values, the Muller matrices can be constructed and the resulting Stokes vectors can be compared to pure linearly horizontal polarized light.

The entry Stokes vector is arbitrary chosen to be a random polarization Stokes vector from early measurements from Table 8.7. The first measurments from the first set is chosen which is

$$S = [1\,;\, 0.131\,;\, -0.270\,;\, 0.118]. \tag{7.6}$$

The resulting Stokes vectors S' are normalized and summarized hereunder in Table 7.2.

Wavelength [nm]	Resulting Stokes vector
3710.25	[1 ; 0.999 ; -3.1e-04 ; 1.4e-04]
3800	[1 ; 0.999 ; -2.5e-04 ; 1.1e-04]
3897.75	[1 ; 0.999 ; -4.2e-04 ; 1.8e-04]

Table 7.2: Resulting Stokes vectors from the non-perfect LP for limit wavelengths allowed by L2 filter and QWP design wavelength.

The resulting circular and oblique components seem to be negligible, even more when their proportion in the total polarization state is checked (the square of the component). The maximum absolute percentage of oblique polarization corresponds to $1.7e^{-5}\%$ and the maximum proportion of circular polarization is $3.3e^{-6}\%$ of the total polarization.

The second observable effect is the error on the orientation of the fast axis of the LP. In this case, a perfect linear polarizer is considered since the performance of the LP from Thorlabs is close to perfect LP. The Muller matrix representing the perfect LP with respect to the orientation of the transmisson axis (θ) is the following.

$$M_{LP}(\theta) = \frac{1}{2}\begin{pmatrix} 1 & cos(2\theta) & sin(2\theta) & 0 \\ cos(2\theta) & cos^2(2\theta) & sin(2\theta)cos(2\theta) & 0 \\ sin(2\theta) & sin(2\theta)cos(2\theta) & sin^2(\theta) & 0 \\ 0 & 0 & 0 & 0 \end{pmatrix}, \tag{7.7}$$

As before, the imperfect horizontal LP is analyzed. A error of 2 degrees maximum is the most likely error with respect to the manually orientation of the transmission axis. Deviations from the perfect horizontal LP of $\pm 1^\circ$ and $\pm 2^\circ$ are then studied and compared to no deviation at all. Results obtained by multiplying initial Stokes vector 7.6 by Muller matrix considering $\theta = \pm 1^\circ, \pm 2^\circ$ are displayed in Table 7.3.

Transmission axis deviation	Resulting Stokes vector
-2°	[1 ; 0.998 ; -0.07 ; 0]
-1°	[1 ; 0.999 ; -0.035 ; 0]
1°	[1 ; 0.999 ; 0.035 ; 0]
2°	[1 ; 0.998 ; 0.07 ; 0]

Table 7.3: Resulting Stokes vectors from the deviated LP transmission axis for -2, -1, 1 and 2° from the horizontal.

The effect of small deviations on the resulting polarization has more impact, or at least less negligible oblique components. The non-perfect linear polarization measurements obtained before are most likely due to deviation of the transmission axis more than the effect induced by the intrinsic performance of the LP used.

7.1.2 Quarter Wave Plate

In Muller formalism, a perfect QWP with its fast axis horizontally oriented is represented with the following matrix.

$$M_{QWP} = \begin{pmatrix} 1 & 0 & 0 & 0 \\ 0 & 1 & 0 & 0 \\ 0 & 0 & 0 & 1 \\ 0 & 0 & -1 & 0 \end{pmatrix}, \tag{7.8}$$

However, the QWP can produce a non-perfect retardance. The quart wave plate induces a retardance of a quarter of the wavelength between both orthogonal compounds of the electric field with a tolerance of $\lambda/100$ specific to this QWP. In terms of phase, it gives a leading phase of $\pi/2$ to the component parallel to the fast axis with respect to the component parallel to the slow axis. This retardance is the most accurate when working at the QWP design wavelength which is 3800 nm for the QWP used. More than the variations induced by the retardance tolerance, the retardance is dependent on the wavelength and differs from $\pi/2$ with wavelength longer or shorter than the design wavelength as it is depicted in Figure 7.2.

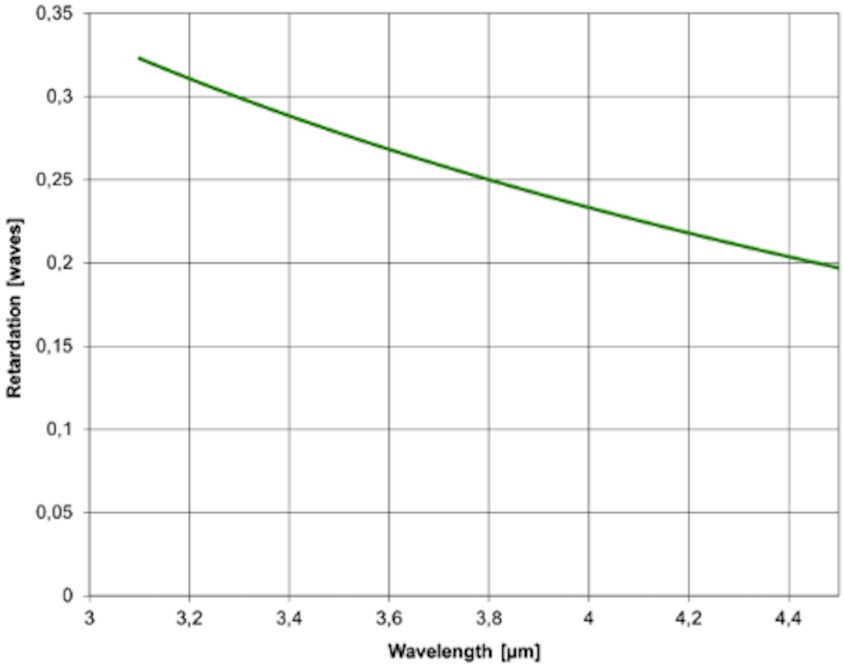

Figure 7.2: Dependence of the retardance of the quarter wave plate in terms of wave factor with respect to the wavelength.

As the filter L2 is used, the maximum and minimum retardance observed can be determined to observe the effect on an initial Stokes vector. This will be combined to the retardance tolerance to observe extreme cases. Retardance values at 3710.25 (considering a deviation of $\lambda/100$), at 3800 (with both extreme cases of the torerance, with $\pm\lambda/100$) and at 3897.75 (considering a deviation of $-\lambda/100$) are determined. The specific retardances are computed using a quadratic interpolation thanks to values at 3750, 3800 and 3850 nm. The retardance values are summarized in the Table 7.4 below.

The retardance depending form of the QWP Muller matrix is given as following with δ

Wavelength [nm] and tolerance	Retardance value [waves]
3710.25 ($+\lambda/100$)	0.27
3800 ($+\lambda/100$)	0.26
3800 ($-\lambda/100$)	0.24
3897.75 ($-\lambda/100$)	0.234

Table 7.4: Retardance for limit wavelength and limit retardance tolerance values.

the retardance in degrees:

$$M_{QWP}(\delta) = \begin{pmatrix} 1 & 0 & 0 & 0 \\ 0 & 1 & 0 & 0 \\ 0 & 0 & cos(\delta) & sin(\delta) \\ 0 & 0 & -sin(\delta) & cos(\delta) \end{pmatrix}. \tag{7.9}$$

The impact of this non-perfect QWP is observed using an entry oblique polarization at 45° since the effect on this polarization using a perfect QWP is well-known and corresponds to a resulting left-handed circular polarization after the QWP. The resulting Stokes vectors are summarized in the following table. The retardance seems already be more sensitive to the

Wavelength and tolerance [nm]	Normalized Stokes vector
3710.25 ($+\lambda/100$)	[1 ; 0 ; -0.125 ; -0.992]
3800 ($+\lambda/100$)	[1 ; 0 ; -0.063 ; -0.998]
3800 ($-\lambda/100$)	[1 ; 0 ; 0.063 ; -0.998]
3897.75 ($-\lambda/100$)	[1 ; 0 ; 0.1 ; -0.995]

Table 7.5: Resulting stokes vector after a non-perfect QWP for limit wavelength and limit retardance tolerance values with oblique polarized light upon entry.

wavelength with more impact due to the imperfect retardance on the resulting polarization state than the impact of the non-perfect polarizer could be. The non-perfect retardance can't be solved except by chosing the narrower filter possible which has been done.

The only optimization possible is on the orientation of the fast axis. The effect of the deviation of the fast axis from the horizontal or the angle that induce a retard of $\pi/2$ on the phase is analyzed considering the same deviations as earlier which are $-2°$, $-1°$, $1°$ and $2°$. The impact of the orientation of the axis in the Muller matrix of the QWP is represented hereunder as given in C. U. Keller [26] considering a perfect retardance of 90°.

$$M_{QWP}(\delta) = \begin{pmatrix} 1 & 0 & 0 & 0 \\ 0 & cos^2(2\phi) & cos(2\phi)sin(2\phi) & sin(2\phi) \\ 0 & cos(2\phi)sin(2\phi) & sin^2(2\phi) & cos(2\phi) \\ 0 & -sin(2\phi) & -cos(2\phi) & 0 \end{pmatrix}. \tag{7.10}$$

As for the non-perfect retardance, the oblique polarization Stokes vector is used at entry to be able to compare the resulting Stokes vector to the perfect left-handed circular polarization. The resulting vectors are summarized in next table. Contrary to results from

Fast axis deviation [deg]	Normalized Stokes vector
-2	[1 ; -0.07 ; 0.005 ; -0.998]
-1	[1 ; -0.035 ; 0.001 ; -0.999]
1	[1 ; 0.035 ; 0.001 ; -0.999]
2	[1 ; 0.07 ; 0.005 ; -0.998]

Table 7.6: Resulting stokes vector after a QWP with its fast axis deviating from the horizontal by $-2°$, $-1°$,$1°$ and $2°$.

Table 7.5, the second Stokes parameter is impacted. Opposite angles of deviation have only an impact on the sign of second Stokes parameter, apart from that, the Stokes vectors are similar for deviation with opposite sign. The orientation of the fast axis has less impact than the intrinsic retardance on the oblique parameter. However, in order to obtain results from Table 8.22, the orientation of the QWP which has been slightly changed, could have had an impact to reduce the unwanted linear proportion in the polarization state after the circular polarizer.

Given that both effects (retardance error and orientation imperfections) have non-negligible impacts, their combined influence can be evaluated using the following matrix (which is separated in two parts being too large to display in one piece).

$$M_{QWP}(\phi,\delta)[:,1,2] = \begin{pmatrix} 1 & 0 \\ 0 & \cos^2(2\phi) + \cos(\delta)\sin^2(2\phi) \\ 0 & \cos(2\phi)\sin(2\phi) - \cos(2\phi)\cos(\delta)\sin(2\phi) \\ 0 & -\sin(2\phi)\sin(\delta) \end{pmatrix} \tag{7.11}$$

$$M_{QWP}(\phi,\delta)[:,3,4] = \begin{pmatrix} 0 & 0 \\ \cos(2\phi)\sin(2\phi) - \cos(2\phi)\cos(\delta)\sin(2\phi) & \sin(2\phi)\sin(\delta) \\ \cos(\delta)\cos^2(2\phi) + \sin^2(2\phi) & \cos(2\phi)\sin(\delta) \\ -\cos(2\phi)\sin(\delta) & \cos(\delta) \end{pmatrix} \tag{7.12}$$

Only the previous limit cases are considered; at 3710.25 nm ($+\lambda/100$) and 3897.75 ($-\lambda/100$) and with $\pm 2°$ of orientation deviation. The resulting Stokes vectors are summarized in next table.

The combination of the unperfect LP with an unperfect QWP can be interesting to study by analyzing the limit configurations.

Wavelength and tolerance [nm]	Fast axis deviation [deg]	Normalized Stokes vector
3710.25 (+λ/100)	±2	[1 ; ±0.074 ; -0.058 ; -0.996]
3897.75 (-λ/100)		[1 ; ±0.067 ; 0.042 ; -0.997]

Table 7.7: Resulting Stokes vector after a QWP with imperfect retardance and fast axis orientation deviation with ±2°.

7.1.3 Combination of the LP with the QWP

Evaluating the combined effect of the inaccuracies of both the LP and the QWP is quite interesting since they will often be used in serie. In all polarization measurements, the analyzer is made of both compounds. More than that, the objective of the first section is to set an accurate circular polarizer. Assessing its inherent inaccuracies seems essential. Again, exetreme cases will be presented to have a range of accuracy tolerance.

As the impact of the non-perfect polarizer is negligible, only the deviation of the transmission for the LP will be combined to both effects evaluated in Table 7.7. The deviation of the transmission axis of the polarizer will be around 45° to correspond to the setup of the circular polarizer. The resulting Stokes vector is then computed by multiplying the initial vector by $M_{LP}(\theta)$ in Equation 7.7 and then by $M_{QWP}(\phi, \delta)$ from Equations 7.11 and 7.12.

$$S' = M_{LP}.M_{QWP}.S \tag{7.13}$$

The resulting Stokes vectors are determined with a deviation of ±2° on the transmission axis of the LP and on the fast axis of the QWP and with a non-perfect retarder at 3710.25 nm and 3897.75 nm with a tolerance of ±λ/100. The results are resumed in Table 7.8. The cases where both LP and QWP undergo the same deviation in the same orientation are discussed since the relative orientation wouldn't change in that case and this is in theory equivalent to the case whose results are summarized in Table 7.5.

Transmission axis deviation [deg]	Wavelength and tolerance [nm]	Fast axis deviation [deg]	Normalized Stokes vector
∓2	3710.25(+λ/100)	±2	[1 ; ±0.147 ; -0.114 ; -0.992]
∓2	3897.75 (-λ/100)	±2	[1 ; ±0.13 ; 0.134 ; -0.992]

Table 7.8: Resulting Stokes vector after a QWP with imperfect retardance, transmission and fast axis orientation deviation with ±2°.

It is quickly seen that important proportions of second and third Stokes vectors are induced by the combined inaccuracies (in the worst cases). These results are only considering the effect of the inaccuracy of the setup. The impacts that the reflection can have on the polarization will be discussed when analyzing the impact of the different parts of VODCA on the polarization state.

7.2 Impact of reflections

VODCA includes many reflections required by the complex optical layout of the coronagraph. Three types of reflections which have been mentioned in Section 2.2 occur in VODCA. Wide angles reflections on gold-coated flat mirrors are used to redirect the light. The large silver-coated parabolic mirrors are used to collimate the light beam on the one hand and to focus it on the other hand. The last reflection is on the silver-coated DM. The main goals of these coatings is to provide the highest reflectivity to avoid any chromatic aberrations. The gold-coating ensures a minimum reflectivity of 96% (Thorlabs) while the silver-coating can achieve up to 98% of reflectance but is more typically around 96%. However, the reflection on these material can have unintented effects at low magnitude, such a retardance, depolarization or diattenuation.

This section aims to introduce the potential effect of the different reflections on the polarization state of the reflected light. This section will not go into any great depth in the analysis of the issue but will provide a first introduction to be referred to when analysing the measurements of the polarization state of the light in various parts of VODCA.

The impact of the reflection of the light on metallic coating is dependent on two specific parameters, the refractive index n and the extinction coefficient κ. These parameters are dependent on the working wavelength of light incident to the metallic coatings.

7.2.1 Gold-coated flat mirrors

This first exploration is based on the work of B. I. Gramatikov [23]. The impact of the reflection on gold-coated mirror is studied with a reflection at 45°, which is the case in the DM part and before the camera. The article gives the tools to estimate the impact on polarization by a specific coating using Muller formalism but this short analysis will be focused on the results. The results show non-negligible impact on different entrance polarization states. However, the study developped is based on a different working wavelength which is 785 nm. Since the refractive index and the extinction coefficient κ are dependant on the wavelength, the results obtained must not be taken as absolute reference. By considering the evaluation of both index from S. Babar and J. H. Weaver [17], the values of both parameters at 785 nm and 3800 nm are compared in following Table.
The difference between the parameters at different wavelengths is indeed non-negligible.

Working wavelength [nm]	Refractive index	Exctinction coefficient
785	0.079	4.712
3800	0.853	25.977

Table 7.9: Refractive index and extinction coefficient of gold for different wavelengths [17].

To go further and in order to be able to properly evaluate the reflection impacts during the measurements in this work, it would be interesting to build the Muller matrix using parameters specific to the working wavelength, 3800 nm.

7.2.2 Silver-coated parabolic mirrors

The estimation of the impact of the reflection cannot be evaluated by the same tools as in the previous subsection as it implies a incidence angle of 45°. The impact on the polarization of silver coated fold mirrors is described in K. Crabtree [19]. Once again the results are obtained assuming a working wavelength in VIS rather than MIR and must therefore be taken with caution. Here after are summarized the different parameters obtained at the wavelength considered in the article and the working wavelength of this work.
In fact, the optical parameters from silver and gold are comparable and their effect on the

Working wavelength [nm]	Refractive index	Exctinction coefficient
450	0.052	2.6747
3800	0.734	27.936

Table 7.10: Refractive index and exctinction coefficient of silver for different wavelengths [17].

polarization could similar. However, the important difference between both reflections is the incidence angle which is much less important considering the reflection on the parabolic mirrors, as can be seen in Figure 2.1. The effect that is particularly discussed in [19], is the effect of beam folding elements which includes parabolic mirrors. The effect of the angle of incidence is also evaluated with a difference of retardance from $1/5^{th}$ to $1/20^{th}$ when the incidence angle varies from 60° to 30°. This result shows the important impact on the incidence angle which is much less important for parabolic mirror which should then induce less retardance and therefore less elliptical polarization impact.

7.2.3 Silver-coated deformable mirror

No specific behaviour to deformable mirror has been found considering the variation of the refractive index and the extinction coefficient. It will then first approximated as a flat silver-coated mirror to consider its impact on polarization. Since the angle of incidence on the DM is again much smaller than 45°, no high retardance is expected as for the reflection on the parabolic mirror.

This slight overview is quite preliminary but ensures a first interpretation of results obtained in next section. To be more consistent, the Muller matrix proposed in [23] could be computed with the informations gathered about the optical parameters of gold and silver to have a first approximation of impacts to the polarization associated to the working wavelength of this work. But for this analysis, the study of the reflective impact didn't go further.

8. Measurements

Various specific parts of VODCA appear to be interesting candidates for assessing the polarization state upon light arrival at their locations. These main parts of VODCA are the DM part, the focal plane and the Lyot stop. By determining the polarization state of the light at these locations, the impacts of the multiple reflections in VODCA will be characterized. Once the impact of the different reflections determined, the optimal placement for the dual polarization setup will be chosen and fixed. Regardless, the first interesting assessment is the polarization state of the source which is at first unknown.

8.1 Polarization of the source

To be able to measure the polarization of the light source, the second optical fiber is unplugged from the mount before the coronagraph part to short-circuit VODCA and get rid of all the reflections which can impact the measurement. The setup is therefore the following shown in Figure 8.1.

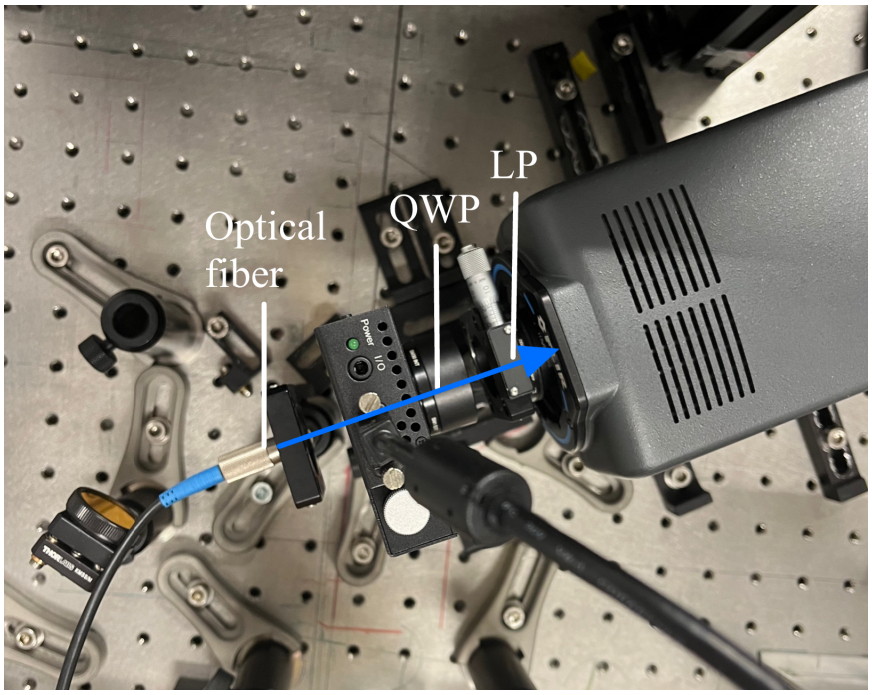

Figure 8.1: Polarization measurement setup in VODCA short-circuited.

The only element between the source part and the camera is the analyzer composed of a LP and a QWP. To get started, only the classical method is tested because, at first, it seems to be easier to use since the rotating mount has not yet been approached and tamed (the rotating mount interface has not yet been created).

8.1.1 Filter comparison

In order to find the best way to analyze the results in the best conditions, the different interesting filters are compared. Different filters are available for the band L : L1, L2, L3, L4, L5 and BBL (Broad-Band). The informations about L1, L2, L3 and BBL filters are represented in Figure 2.3.

The BBL and L2 filters are the two only filters which include the design wavelength of the QWP which is 3800 nm. Both are compared in the first results with some preference for the L2 being narrower and more centered on the working wavelength. The results obtained with both filters are compared and summarized in Table 8.1 below.

Filter	Normalized Stokes vector
BBL	[1 ; 0.172 ; -0.762 ; 0.758]
L2	[1 ; -0.231 ; -0.492 ; 0.858]

Table 8.1: Stokes vectors of the light source with respect to different filters used.

The first condition to verify is the polarization one. As a reminder, this specific condition is $S_0^2 \geq S_1^2 + S_2^2 + S_3^2$. When the Stokes vector is normalized, the condition becomes $1 \geq S_1^2 + S_2^2 + S_3^2$. The results concerning the polarization condition are displayed below in Table 8.2.

Filter	Photometry method
BBL	$1 < 1.185$
L2	$1 < 1.032$

Table 8.2: Polarization condition relative to results obtained in Table 8.1.

The results are very different from one filter to the other. It is then difficult to choose now between the two filters since there are no results much better than the others. However, the polarization condition gives a first sight on the potential variation of the results with a higher exceeding of the condition for the BBL. Moreover, since the design wavelength of the QWP used is 3800 nm, it seems more accurate to limit the wavelength to a narrow range around 3800 nm to have the more precise quarter phase retard. More than that, the results of the AGPM performance using the L2 filter are better than with other filters.

The non-compliance with the polarization condition is not alarming, especially since the polarization condition is not respected only by less than 19% using BBL filter and by 3.2% with the L2 filter. This light exceeding can be due to inaccuracies of the setup during the measurements. As demonstrated in Section 7, the imprecisions of the manipulations can have a non-negligible impact, especially when using a QWP which is the case during the fourth measurement in the classical method which is performed to compute the fourth Stokes parameter. Even though, the processing of the data must be improved.

To avoid results which depend on isolated values or perturbations in the background, an aperture mask is added to the final image as described in Section 6. With this processing feature added, measurements form Table 8.1 are processed again. These results will be used to confirm if the polarization condition is verified or still not complied with. The results obtained are summarized in Table 8.3. Once again the Stokes vector displayed are normalized as it will be always the case.

Filter	Stokes vector
BBL	[1 ; 0.174 ; -0.772 ; 0.18]
L2	[1 ; -0.257 ; -0.48 ; 0.741]

Table 8.3: Stokes vector obtained in short-circuit of VODCA by removing the unwanted light using an aperture mask.

The fourth parameter computed using BBL filter undergoes an important change. The other parameters, including the one from the Stokes vector obtained using L2 filter, are still of the same order of magnitude. The good point is that the polarization condition is verified for each measurement as it is summarized in Table 8.4.

Filter	Polarization condition
BBL	$1 \geq 0.659$
L2	$1 \geq 0.846$

Table 8.4: Polarization condition verified of results from Table 8.3.

The conclusion that can be done from these preliminary results is the positive impact of the aperture mask on the polarization condition. By removing the potential perturbations in the background, the computed median intensity represents the intensity in the final image with more accuracy. After that, a lower variation on the results is observed using the L2 filter, which confirms the choice of the filter used. The higher variation using the BBL filter was expected since the QWP performance can depend on the wavelength. The larger the working filter bandwidth is, the higher the potential variations are. The impacts of the non-perfect retardance with the wavelength are already important using the L2 filter as described in Section 7.1.2. The potential impacts using a filter with a bandwidth near four times larger are expected to be much more important.

The AGPM used in future measurements, the AGPM-L5, provides better performance when the L2 filter used rather than other filters. This feature is a key factor for choosing the L2 filter as working filter.

With respect to the conclusions made in this section, all next measurements are executed using the L2 filter. More than that, in order to avoid any loss of information in the final

results, the ND 1.0 filter is placed juste after the L2 filter to slightly attenuate the incoming light flux.

The Stokes vectors obtained with L2 and BBL filters come from two different measurements. The difference between both polarization states is important and intriguing since the same source has been used. For now, this difference can be explained by the fact that these results are preliminary and the measurement method will be improved in next sections. However, since no information about the polarization of the source is known, the polarization state of the source could be highly variable. This issue is discussed in next Section 8.1.2.

8.1.2 Randomness of the source

Until now, the acquisition method was still just a snapshot of one image after the acquisition of a dark, which removes the background automatically. The evolution of the acquisition method has been described in previous Section 5. It is only now that the acquisition method consisting of collecting pairs of background and open-shutter images is implemented. The objective of this method is to measure more constant results than the Stokes vectors computed in previous section. And this is confirm as shown in the results below in Table 8.5. These four measurements are made the same day.

Normalized stokes vector
[1 ; 0.082 ; -0.481 ; -0.418]
[1 ; 0.047 ; -0.395 ; -0.443]
[1 ; 0.074 ; -0.447 ; -0.543]
[1 ; 0.084 ; -0.532 ; -0.593]

Table 8.5: First set of normalized Stokes vector obtained with the updated acquisition method and the classical measurement method.

The polarization state seems to be more consistent. The accuracy of the polarization measurement can be improved but for now, the issue of the random polarization has to be solved. Indeed, the obtained Stokes vector represent a different polarization state than in Table 8.3. An assumption is that the polarization state of the laser is highly dependent on the external conditions when the light source is activated. That hypothesis explains why the previous results in Table 8.1 correspond to polarization states different from results shown in Table 8.5. This hypothesis can be reinforced by 5 measurements made on a different day. The results corresponding to these measurements are summarized in Table 8.6.

As it can be clearly seen, the vectors of a same set represent the same type of polarization even if for now, there are still variations in the Stokes parameters. But there is a complete shift in polarization state between two sets. This confirms that the source has a polarization state which can change radically between two activations. The measurements taken

Normalized Stokes vector
[1 ; -0.207 ; 0.135 ; 0.117]
[1 ; -0.235 ; 0.163 ; 0.104]
[1 ; -0.243 ; 0.165 ; 0.179]
[1 ; -0.266 ; 0.207 ; 0.188]
[1 ; -0.267 ; 0.205 ; 0.219]

Table 8.6: Second set of Normalized Stokes vectors using the classical measurement method.

on different days are made with the same source with the same power in the same configuration, but some manipulations and differences in temperature when the source is switched on could lead to different states of polarization. Since the SM fibers are made to maintain the polarization state of the incoming light, the change in the polarization state has great chances to occur inside the laser source. However, when manipulating the optical fibers, the mechanical constraints applied on it or the increase in temperature induced can alter the polarization state outgoing the source part, especially considering the measurements made with the short-circuit setup since the optical fiber had to be manipulated to create this setup.

In parallel to the measurements made with the classical method, the rotating QWP method have been introduced and tested. The acquisition and the processing method are adapted to the new measurement method, but the same steps are followed. Indeed, the QWP is more automated, and the script is sufficient to measure a Stokes vector without any manual intervention on the setup. As presented in 4.3, the setup corresponds to a QWP mounted on rotating motorised mount followed by a linear polarizer at 0°. Multiple measurements conducted on various days aim to determine if the hypothesis confirmed using the classical method also holds true when employing the rotating QWP method. Three different sets of five measurements are summarized in Table 8.7.

Normalized Stokes vectors		
1^{st} set	2^{nd} set	3^{rd} set
[1 ; 0.131 ; -0.270 ; -0.118]	[1 ; -0.291 ; -0.134 ; 0.262]	[1 ; 0.103 ; -0.171 ; -0.047]
[1 ; 0.19 ; -0.288 ; -0.199]	[1 ; -0.28 ; -0.134 ; 0.253]	[1 ; 0.128 ; -0.145 ; -0.103]
[1 ; 0.221 ; -0.302 ; -0.253]	[1 ; -0.273 ; -0.134 ; 0.246]	[1 ; 0.143 ; -0.151 ; -0.104]
[1 ; 0.231 ; -0.302 ; -0.268]	[1 ; -0.267 ; -0.133 ; 0.235]	[1 ; 0.129 ; -0.154 ; -0.107]
[1 ; 0.231 ; -0.295 ; -0.270]	[1 ; -0.241 ; -0.15 ; 0.223]	[1 ; 0.119 ; -0.136 ; -0.096]

Table 8.7: Normalized Stokes vectors of the light source obtained with rotating QWP method on three different days.

The condition of polarization is verified for all the Stokes vectors displayed in Table 8.7. The same observations are made with the results from Table 8.5 and Table 8.6. The polarization state is the same with variations along time (there is 10 minutes between each measurement) for measurements made on the same set. These variations can be caused by

the time that the source takes to be stable or to reduce the thermal perturbations induced by manipulations. This seems to be the case in the first set, the last measurements present less and less variations. It goes from up to 68% difference between the same parameter from one measurement to the other to maximum 3% variation. The Stokes vector displayed in Table 8.7 seems to characterize a low polarized state of light.

The degree of polarization of the different results from Table 8.5, Table 8.6 and Table 8.7 are summarized hereunder. It is computed with respect to the mean Stokes vector of each set.

	Measurement method	
	Classic method	Rotating QWP method
1^{st} set	0.685	0.418
2^{nd} set	0.341	0.389
3^{rd} set	/	0.216

Table 8.8: Degree of polarization of the mean Stokes vectors from Table 8.5, 8.6 and 8.7.

It is important to note that only the second sets of both methods have been measured the same day, the others set (especially the first one) are not necessarily made with the same "activation" of the source. According to these results, the light source tends to be more unpolarized than completely polarized. It is mentionned in Schaefer et al. [3] that polarization work must only be done using a linear polarized source of light, a randomly polarized source of light is not suitable for this kind of measurements. The variable behaviour of the polarization state of the light source may tend to particular results such as low polarized light as shown in Table 8.8. Based on the results obtained in this section and this affirmation also stated in D. Goldstein [22], the polarization light coming from the source must be properly filtered using a polarizer to be able to work with polarization measurements.

8.2 Polarization filtered

In order to characterize the effect on the polarization of the different parts of VODCA and to allow an effective wavefront retrieval, the input polarization must be determined and fixed. Therefore, applying a linear polarizer at the input to enforce known polarization appeared to be a reasonable approach. At first the linear polarization is fixed arbitrary to 45°. However, after that, in order to get the least impact from reflections, the input polarization must be set by a linear polarizer at 0 or 90° to obtain horizontal or vertical polarized light which is less impacted by reflections. Due to space constraints, the linear polarizer cannot be placed between the source and the analyzer in the actual setup represented in Figure 8.1 and the latter must therefore be adapted as seen in Figure 8.2. The optical fiber mount and the first linear polarizer are placed before the last mirror as shown in this picture.

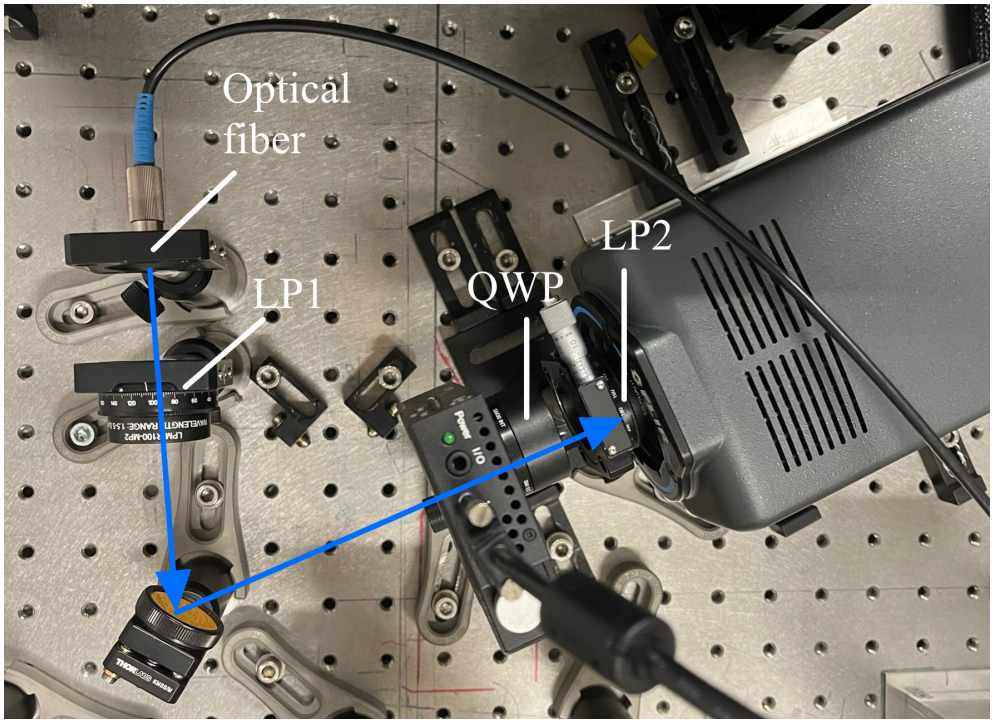

Figure 8.2: Polarization measurement setup in VODCA short-circuited with linear polarizer after the optical fiber.

8.2.1 First measurements set

For the sake of trust in our measurement method and in the precision of linear polarizer, several measurements are made with this updated setup. These first results are obtained with a linear polarizer set at 45° after the source part and are summarized in Table 8.9. Both measurement methods are used and compared.

Measurement number	Measurement method	
	Classic method	Rotating QWP method
1	[1 ; 0.214 ; -0.828 ; -0.211]	[1 ; 0.265 ; -0.915 ; 0.251]
2	[1 ; 0.27 ; -1.001 ; -0.306]	[1 ; 0.26 ; -1.079 ; -0.254]
3	[1 ; 0.307 ; -1.002 ; -0.312]	[1 ; 0.248 ; -0.608 ; -0.174]
4	[1 ; 0.273 ; -0.991 ; -0.175]	[1 ; 0.113 ; -1.445 ; 0.089]

Table 8.9: Stokes vectors obtained in short-circuit with a entrance linear polarization state filtered at 45°.

Classical method results

Considering first the classical method, the diagonal part of the polarization is well represented in the third parameter of the Stokes vector. An opposite sign is observed for the third parameter (S_2 must be positive for a linear polarization at 45°) and this is due to

the reflection on the mirror before the analyzer. The reflection changes the 45° linearly polarized light into -45° polarized light. Non-negligible linearly horizontal and circularly right-handed polarization components appear in the Stokes vector. This unwanted contribution in S_1 parameter comes certainly from the inaccuracy of the angle of the entry linear polarizer which can give some horizontal contribution or from the inaccuracy of the analyzer.The reflection on the wide angle mirror can also impact in elliptical components. As introduced in Section 7.2, some retardance can be induced when considering a angle of incidence of 45° on a gold-coated mirror. However, as this effect is limited by the high reflectivity of gold at the working wavelenth, such mangitude of elliptical polarization has more probability to be induced by inaccruacies in the analyzer. In spite of it all, this potential perturbation will be corrected by placing the entry polarizer just after the mirror.

To compare with other linear polarization orientation, the entry linear polarizer will be set to 0° for next measurements which is also more easily adjustable thanks to a precise digital height gauge. The perturbations encountered must be solved since they induce a polarization condition which is not respected for most of the measurements. The setup for the classic method becomes an entry LP with its transmission axis fixed to the horizontal at 0° after the last wide angle mirror followed by the analyzer with the optical fiber mount at the same place before the last mirror due to space constraints.

Rotating QWP method results

Concerning the QWP method, more aberrant results are obtained. Except for the first Stokes vector which is similar to the results obtained with the classical method, most of the other vectors don't verify the polarization condition and give totally unacceptable values with some parameters way above 1, which is, by definition, not possible. This is clearly a problem coming from the measurement method or the processing method. As for the classical method, the same measurements will be made with a linear polarizer with its transmission axis parallel to the x-axis, which is set from the beginning to the horizontal, to be parallel to the surface of the testbench.

8.2.2 Second measurements set

The results displayed in following Table 8.10 are obtained for both methods. To allow the comparison, the two last results in the table correspond to Stokes vector obtained with the entry linear polarizer placed juste before the last wide angle mirror.

Classical method results

As expected, less perturbations in oblique and circular parameters are observed. First about the classical method, by comparison with the two last measurements, the effect of the wide-angle mirror on the linear polarization is clearly seen with an added contribution in the oblique parameter. Each time one of the parameters exceeds the maximum value of

1^{st} LP position	Measurement number	Measurement method	
		Classical method	Rotating QWP method
After the last mirror	7	[1 ; 0.996 ; -0.005 ; -0.088]	[1 ; 0.855 ; 0.094 ; 0.0002]
	8	[1 ; 1.041 ; -0.033 ; -0.09]	[1 ; 0.949 ; -0.031 ; 0.011]
	9	[1 ; 0.974 ; 0.029 ; -0.149]	[1 ; 0.831 ; -0.07 ; -0.021]
	10	[1 ; 1.028 ; -0.002 ; -0.061]	[1 ; 0.911 ; -0.031 ; -0.001]
Before the last mirror	11	[1 ; 0.97 ; 0.281 ; -0.084]	[1 ; 1.009 ; 0.208 ; 0.018]
	12	[1 ; 0.979 ; 0.253 ; -0.095]	[1 ; 0.944 ; 0.213 ; -0.002]

Table 8.10: Stokes vectors obtained in short-circuit with an entry polarization forced to horizontal linearly polarized light.

one, such as in the measurements 8 or 10 for the classical method, the polarization condition is obviously not respected. However, the polarization condition is eceeding by only less than 10% considering the measurments 8 and 9 which is an acceptable error margin considering the potential errors during the measurements. Nevertheless, the contribution of the circular parameter is less important and closer to 10% than 20 or 30% like it was the case in previous measurements in Table 8.9. The values obtained for the oblique parameter (S_3) can be linked to imprecisions on the transmission axis of the first LP as it corresponds to the order of magnitude found in Table 7.3 when evaluating the impact of potential errors using Muller formalism. The circular parameter (S_3) is probably linked to imprecisions in the analyzer as the apparition of elliptical polarization comes the impact of a phase retard which can only be induced by the QWP of the analyzer in this setup.

Rotating QWP method results

Then, regarding the rotating QWP method, the results have nothing in common with the results from the Table 8.9 and are even better than the results obtained with the classical method. This was expected at first when describing the accuracy of the two methods. The oblique parameters oscillate around 0 such as for the classical method and the circular parameter is much lower than what is being sought. The only measurement which leads to unchecked polarization condition corresponds to the 11^{th} measurement which is impacted by the perturbations of the reflections on the wide-angle mirror.

8.2.3 Review

The conclusion drawn from this segment is that the polarization must be at its purest state before being influenced by any component of the system, in order to accurately measure the effect of that specific component. This is made possible by filtering the polarization state of the light coming from the source part. A linear polarizer is therefore set with its transmission axis to the horizontal after the optical fiber. According to the last results, the rotating QWP method is more promising, with only 8 data points, but both methods will be applied to measure the impact of the following parts of VODCA to continue the

comparison and confirm the accuracy of the second method.

8.3 Impact of the DM part

The deformable mirror environment is a sensitive part of VODCA. The reflection of the light on it can be particular due the 97 actuators deforming the mirror which gives to it the main role in the aberrations control. It is so highly interesting to determine its effect on the polarization. Two mirrors are also considered in DM part and are used to redirect the light to the DM. These mirrors induce reflections with large angles. These reflections could also have a significant impact on the polarized light. Due to space constraints, the DM with the two wide angle mirrors must be considered together as the DM part.

8.3.1 First setup

Based on the conclusion of the last section, the polarization of the light must be filtered before getting to measure the effect of the DM part. To this end, a first setup is created with a horizontal linear polarizer placed just after the source of light. This ensures that the polarization of light coming from the source part is known. With respect to the random polarization coming from the source, a greater or lower amount of light is filtered by the LP. This is because the initial polarized light can have a higher or lower proportion of linear polarized light. The analyzer is placed just after the DM part. Both measurement methods are still used at this stage of the project. The initial setup corresponding to this section is depicted in Figure 8.3.

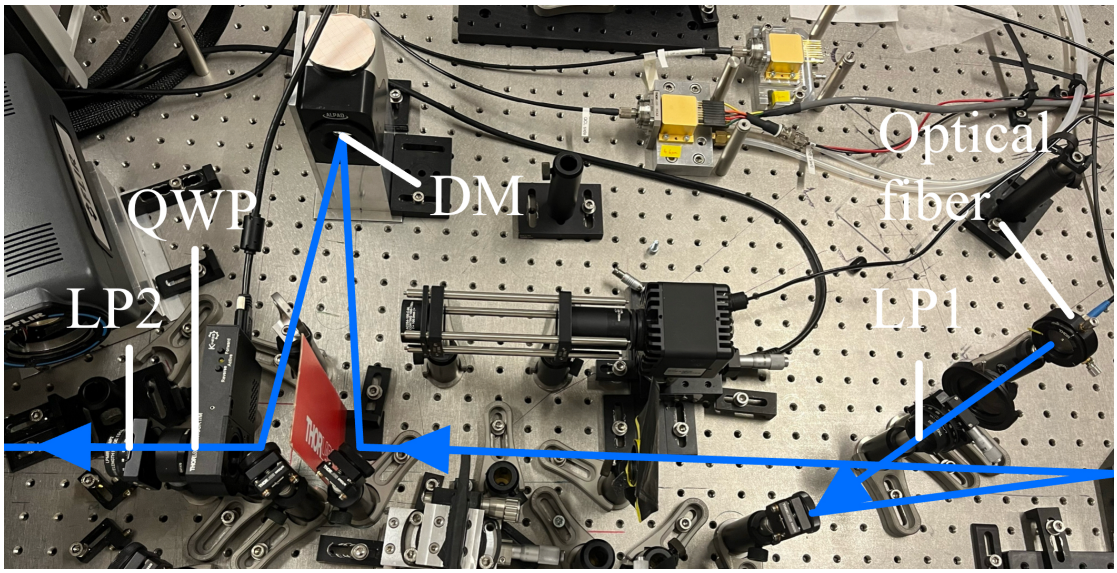

Figure 8.3: Polarization measurement setup for DM part analysis.

By positioning the LP just after the source part, more than just the DM part is considered for the measure. Indeed between the source part and the DM part, two reflections occur, the first to redirect the light onto the large parabolic mirror and the second on the parabolic mirror. The measurement methods seem to work with a linear polarizer with an horizontal transmission axis but in order to verify that this is not the only case which allows the methods to give good results, the same measurements will be made with a vertical polarized in entry, which means a linear polarizer with its transmission axis perpendicular to the x-axis in entry. The Stokes vectors therefore measured are summarized in Table 8.11.

1^{st} LP orientation	Measurement number	Measurement method	
		Classic almethod	Rotating QWP method
Horizontal polarization	13	[1 ; 0.961 ; 0.353 ; -0.077]	[1 ; 0.754 ; -0.095 ; -0.137]
	14	[1 ; 0.957 ; 0.360 ; -0.078]	[1 ; 0.751 ; -0.085 ; -0.129]
	15	[1 ; 0.963 ; 0.397 ; -0.100]	[1 ; 0.715 ; -0.074 ; -0.134]
	16	[1 ; 0.980 ; 0.396 ; -0.106]	[1 ; 0.721 ; -0.078 ; -0.131]
Vertical polarization	17	[1 ; -0.971 ; -0.178 ; -0.034]	[1 ; -0.975 ; 0.098 ; 0.144]
	18	[1 ; -0.972 ; -0.207 ; -0.078]	[1 ; -0.976 ; 0.078 ; 0.142]
	19	[1 ; -0.968 ; -0.209 ; -0.123]	[1 ; -0.978 ; 0.088 ; 0.144]
	20	[1 ; -0.970 ; -0.190 ; -0.060]	[1 ; -0.981 ; 0.081 ; 0.141]

Table 8.11: Stokes vectors obtained by filtering a linear polarization in entry just after the source part and analyzing the impact on the polarization state by the DM part.

Horizontal and vertical polarization directions are not affected by reflections in the same way as oblique and circular polarizations. The Stokes parameters relative to the horizontal and vertical polarization are retrieved close to 1 (-1 respectively) except for the horizontal polarization vectors measured with the rotating QWP method which can be explained by an error occured during the measurements. In fact, during the initial uses of the rotating mount, the motorized mount sometimes did not work as expected, resulting in a stationary mount that led to unwanted outcomes. However, this type of malfunction was quickly solved and this significant decrease with respect to the total intensity is no longer observed. These results are therefore considered as an exception. Except for this particular set, the results for the second method are more constant from 2% to 22% variation for the rotating QWP method compared to variations from 0.4% to 72% for the classical method. For measurements 13 to 16 for the first method, the second parameter is too high which gives a polarization condition not verified. But the condition is encountered for all others measurements. More specifically, the polarization condition for measurements 13 to 16 using classical method are displayed in the following Table 8.12.

The condition is not respected at a maximum of near 13%, which can be an acceptable range of error even if it is non-negligible. In Section 7 the impact of the inaccruacy of the LP and QWP on the resulting polarization state have been evaluated. These intrinsic errors combined to the low variations of the source intenisty during multiple measurements

Measurement number	Polarization condition
13	5.4%
14	5.2%
15	9.%
16	12.8%

Table 8.12: Polarization condition overshoot error of results from 8.11.

can lead to this type of exceeding polarization condition.

Moreover, the results are more similar between the results obtained with both polarization states injected for the second method. The most important variation in absolute value for the second parameter in the Stokes vector for the classical method is about 55% while it corresponds to maximum 24% for the other method. The switch of sign for the third and the fourth parameters makes also more sense for the rotating QWP method. Indeed, a perturbation to a horizontal polarization which gives a negative oblique polarization will naturally give a positive oblique polarization when applied to a vertical polarization. This is theoretically logical if one reflection entails a specific phase retard. And this is the same reasoning for the circular parameter.

8.3.2 Setup update

In order to isolate properly the effects of the DM part, the polarization filter should be placed just before the concerned part. The perturbation on the Stokes vectors due to other reflections will be then neglected. These manipulations are made with only the horizontal polarization in entry.

1^{st} LP orientation	Measurement number	Measurement method	
		Classic method	Rotating QWP method
Horizontal polarization	21	[1 ; 0.959 ; 0.261 ; -0.070]	[1 ; 0.982 ; 0.096 ; 0.138]
	22	[1 ; 0.959 ; -0.037 ; -0.040]	[1 ; 0.969 ; 0.085 ; 0.142]
	23	[1 ; 0.963 ; -0.072 ; -0.038]	[1 ; 0.956 ; 0.060 ; 0.141]
	24	[1 ; 0.958 ; 0.229 ; -0.042]	[1 ; 0.933 ; 0.032 ; 0.146]

Table 8.13: Stokes vectors obtained by forcing a linear polarization in entry just before the DM part and analyzing the impact on the polarization by the DM part.

Rotating QWP method results

Considering the rotating QWP method, the problem with too low values for the second parameter is no longer encountered. The third and fourth parameters are even similar to the results in the Table 8.11. The opposite signs are resulting from the reflections on an

odd number of mirrors. For example, considering a 45° polarization, the reflection on an even number of mirrors will result in a 45° polarization state while reflections on an odd number of mirrors will result in a -45° polarization state since the polarization is inverted at each reflection, as it was concluded when observing the effect of the last mirror on an oblique polarization state in Table 8.9.

Classical method results

The classical method seems more sensitive to perturbations induced by the different reflections while the results obtained with the rotating QWP method are mainly impacted by the DM part since they are similar with results from 8.11. If the results from Table 8.13 and Table 8.9 obtained with the rotating QWP are compared, the nearly 15% in circular polarization seem to be induced by the DM part, or even the DM itself since the wide angle mirrors didn't have such an impact when observing the results in Table 8.9 while characterizing the polarization state of the light source. However, since each type of coating can induce some retardance, the elliptical polarization can be induced by the combination of the effects induced by all three reflections.

8.3.3 Review

The measured polarization and the difference between the horizontal polarization vector ([1;1;0;0]) and the vector measured is firstly due to the precision of the setup. The purity of the input polarization and precision of the angles of the LP and the QWP of the analyzer are limited to the manipulations and alignments of the different compounds and it can impact the Stokes vectors obtained in a non-negligible way as demonstrated in Section 7 . The second larger impact is due to the reflections on the wide-angle reflection mirrors and on the DM. This effect induced by the reflections originates from the coatings used on the different mirrors, which can induce relatively slight phase retardation on the incoming light. The effect induced by the DM is difficult to separate from the impacts of the other reflections in the DM part. Therefore, the DM part impacts the polarization state of light in a non-negligible way, it seems reasonable to filter the horizontal polarization after the DM to be independent of the perturbations from this part of VODCA.

8.4 Impact of the parabolic mirrors

As concluded in the previous section, the polarization must be filtered after the DM part since unwanted elliptical components are induced by the DM part. By filtering the polarization state of the light coming from the DM part, the potential perturbations on the polarization of the light can come from the reflection on the focusing parabolic mirror before the focal plane. To assess this impacts, the Stokes vectors are computed with the analyzer after the focal plane where one reflection on a parabolic mirror occur and after the Lyot stop where two reflections of this type occured.

8.4.1 Polarization state at the focal plane

It is at the focal plane that it is most important to know precisely the state of polarisation of the focused light and to be able to control it with a high level of accuracy. In the coronagraph setup, the AGPM is placed in the focal plane and to be able to characterize the effect of the AGPM and verify its performances, the arriving light polarization state must be well known and controlled. The setup to measure the polarization in the focal plane corresponds therefore to the first LP juste after the DM part and the analyzer just after the focal plane mount. This setup is represented in the picture in Figure 8.4.

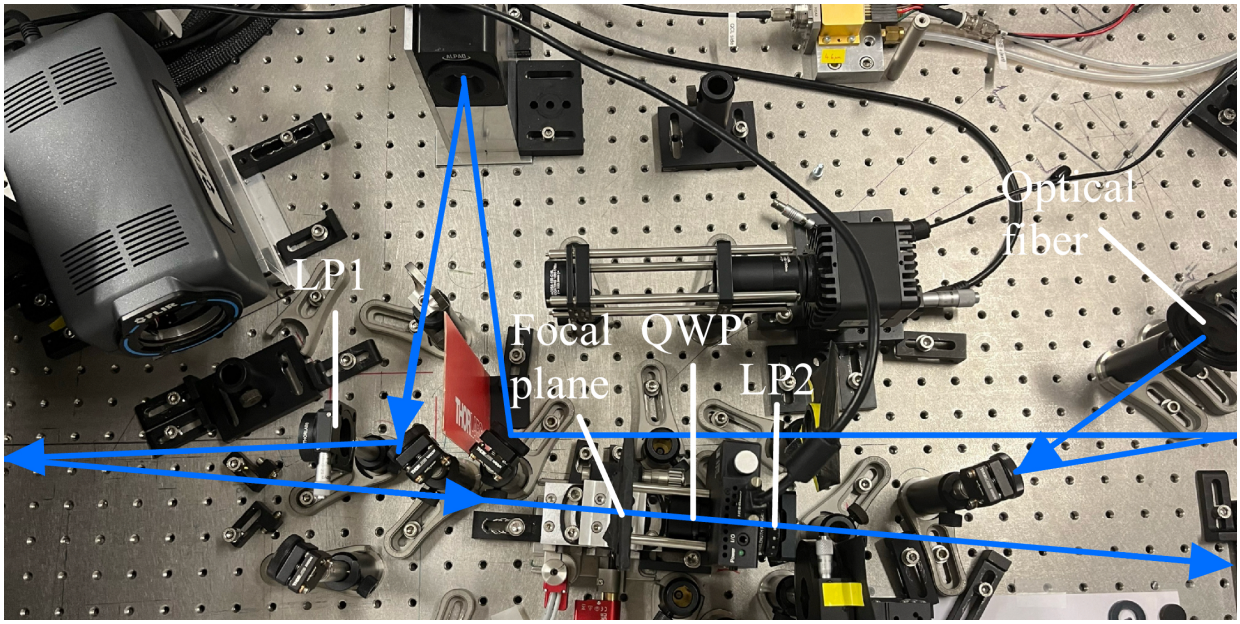

Figure 8.4: Polarization measurement setup for focal plane part analysis.

The first results are summarized in the Table 8.14 hereunder. The rotating QWP method being more constant and offering more precise results, this method is chosen to measure the polarization state for now.

The part of circular polarization which is associated to the reflections in the DM part which induced an elliptical component in previous Section 8.3 is now eliminated to leave a circular parameter relatively close to 0, with a maximum of 0.02% of circular polarization (the total polarization given by $S_1^2 + S_2^2 + S_3^2$). The second parameter represents a purer linear polarized light for vertical polarized than horizontal polarized light in entry. The minimum contribution by S_1 is 77 % with horizontal polarization in entry contrary to 97.812% minimum for vertical polarized light in entry. However the oblique parameter has the same order of magnitude with a mean contribution of 2% for both set of measurements. This difference with the pure horizontal (respectively vertical) polarized light comes either from the inaccuracy of the x-axis reference of the first LP or the analyzer, or some perturbations encountered with the reflection between the filtering LP and the analyzer. The oblique parameter could be induced by the combination of an imprecised transmission axis

1^{st} LP orientation	Measurement number	Rotating QWP method
Horizontal polarization	25	[1 ; 0.939 ; 0.159 ; -0.004]
	26	[1 ; 0.942 ; 0.165 ; -0.014]
	27	[1 ; 0.879 ; 0.160 ; -0.002]
	28	[1 ; 0.913 ; 0.149 ; 0.004]
Vertical polarization	29	[1 ; -0.994 ; -0.149 ; -0.004]
	30	[1 ; -0.998 ; -0.171 ; 0.013]
	31	[1 ; -0.990 ; -0.164 ; 0.001]
	32	[1 ; -0.989 ; -0.163 ; -0.001]

Table 8.14: Stokes vectors obtained by forcing a linear polarization in entry just after the DM part and analyzing the state of the polarization at the focal plane.

orientation of the first polarizer with the reflections on the parabolas. The polarization condition for Stokes vectors with vertical polarization upon entry is not verified. This is expected due to the first parameter close to 1. The corresponding polarization conditions are displayed in following Table 8.15

Measurement number	Polarization condition
29	1%
30	2.5%
31	0.7%
32	0.5%

Table 8.15: Polarization condition overshoot error of results from 8.14.

This time the polarization condition is very slightly not fulfilled, which can be neglected and due to small measurements errors.

8.4.2 Polarization state at the Lyot stop

The last hypothesis about the oblique component is verified by placing the analyzer after the Lyot stop where one more reflection has been encountered on a similar parabolic mirror. The Stokes vectors obtained are shown in Table 8.16.

The oblique contribution is now at least twice as high as in results from Table 8.14 which confirms what was expected. Two similar reflections happen before the light arrives to the Lyot stop. The generation of this oblique contribution can then be associated with the reflections on the silver-coated parabolas. The other effect already discussed before is the switch in the sign of the parameter which is due to the reflection itself and happens in particular for oblique polarization. Both entrance polarizations undergo some decrease

1^{st} LP orientation	Measurement number	Rotating QWP method
Horizontal polarization	33	[1 ; 0.852 ; -0.331 ; -0.016]
	34	[1 ; 0.876 ; -0.434 ; 0.022]
	35	[1 ; 0.858 ; -0.359 ; -0.002]
	36	[1 ; 0.848 ; -0.336 ; 0.007]
Vertical polarization	37	[1 ; -0.968 ; 0.359 ; -0.008]
	38	[1 ; -0.965 ; 0.38 ; -0.002]
	39	[1 ; -0.967 ; 0.372 ; -0.001]
	40	[1 ; -0.967 ; 0.369 ; 0.003]

Table 8.16: Stokes vectors obtained by forcing a linear polarization in entry just after the DM part and analyzing the state of the polarization at the Lyot stop.

in the second parameter. Since the oblique contribution has increased, this decreasing in horizontal (resp. vertical) contribution is logical. Despite this decrease, the polarization condition is still not respected.

Measurement number	Polarization condition
37	6.6%
38	7.6%
39	7.3%
40	7.1%

Table 8.17: Polarization condition overshoot error of results from 8.16.

Compared to the condition values shown in Table 8.15, the values are less negligible in this case, but being still no more than a few hundredths. These larger overshoots may still be induced by the same inherent errors to the measurement setup but impacted twice more by reflections than the results from Table 8.15.

8.4.3 Increasing of sample points number

Now that the rotating QWP method and its measurement setup are beginning to be more accurate, the same measurements are made with 16 data points instead of 8 data points to check if a notable increase in precision is observed or if 8 data points are largely sufficient to obtain relatively good results. These measures have been made with the vertical polarization in entry, at the focal plane and at the Lyot stop. The results are displayed in Table 8.18.

These results confirm the previous results obtained with 8 data points with a bit more consistency as it can be concluded from a fewer results. Especially for the last parameter which

Analyzer position	Measurement number	Rotating QWP method (16 data points)
After the focal plane	41	[1 ; -0.994 ; -0.145 ; -0.002]
	42	[1 ; -0.991 ; -0.146 ; -0.004]
After the Lyot stop	43	[1 ; -0.967 ; 0.359 ; 0.003]
	44	[1 ; -0.963 ; 0.365 ; 0.003]

Table 8.18: Stokes vectors obtained by forcing a vertical linear polarization in entry just after the DM part and analyzing the state of the polarization at the focal plane and at the Lyot stop, with the rotating QWP method using 16 data points.

should not be affected by the reflection on the parabolic mirrors as expected. The same polarization state is expressed in these Stokes vector than in Table 8.14 and in Table 8.13. 8 data points are sufficient to get an idea of the polarization state using the rotating QWP method and give a better compromise between the time consumption and the accuracy, but using 16 data points offers more consistency and precision. However, this increase in consistency does not resolve the issue of the non-compliance with the polarization condition.

Measurement number	Polarization condition error
43	6.4%
44	6.1%

Table 8.19: Polarization condition overshoot error of results from 8.18.

The values obtained by computing the non-respected polarization condition are indeed of the same magnitude.

8.4.4 Review

The conclusion of all these measurements appears to be quite simple. Due to the different impacts of several parts of VODCA on the polarization state of the light coming from the source and being aware of the highly varying polarization state of the light source, the polarization must be filtered just before the focal plane, where the AGPM will be placed, in order to control the purest polarization of the light before it interacts with the AGPM.

8.5 Circular polarization measurements

For the subsequent stage of this work, it is imperative that the light incident on the AGPM possesses the most pristine circular polarization, to effectively characterize the performance of the vortex and to allow the most efficient wavefront sensing. The information concerning the polarization state of the incoming light must be relied upon with upmost confidence. This is why, in parallel to previous measurements, some early tests of circularly polarized light measurements have been done.

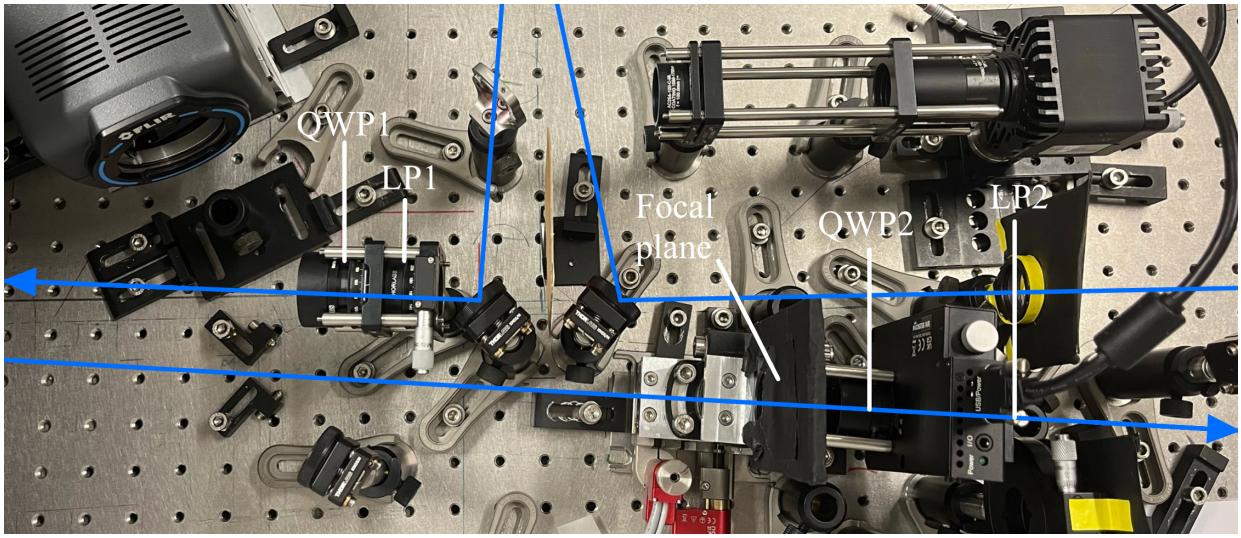

Figure 8.5: Polarization measurement setup for circular polarization analysis.

8.5.1 Polarizer after the DM part

The setup to filter circular polarization is the same as in Figure 8.4 with QWP added after the first LP to create a circular polarizer.

The polarization filter in entry is composed of a linear polarizer followed by a QWP fixed with its fast axis parallel to x-axis, the horizontal in the testbench plane. In order to induce right-handed circularly (RH) polarized light, the difference in angle between the transmission axis of the LP and the fast axis of the QWP must be -45°. On the contrary, in order to obtain left-handed circularly (LH) polarized light, the difference between the two orientations must be +45°. Since the QWP is fixed to 0°, to have RH polarization, the linear polarizer must be oriented to -45° (or 135°) and to have LH polarization, the LP must be oriented to +45°.

A RH polarized light has been first induced just after the DM part. In fact these first measurements have been made before concluding the necessity of a polarization filter just before the focal plane. Two sets of measurements are presented here below in Table 8.20, two measurements obtained with the analyzer placed after the focal plane and the two others with the analyzer placed after the Lyot stop.
Since the condition on the polarization is given by $S_0^2 \leq S_1^2 + S_2^2 + S_3^2$, the proportion of each Stokes parameter over the total intensity of the ligh beam is given by the squared parameter. The proportion of the first parameter is negligible since it correponds to maximum a contribution of less than 0.2%, and thus can be associated to some perturbations and inaccuracy of the setup. Now, the second parameter, the oblique contribution, is non-negligible. It correponds to less than 2% of the total polarization. It is a small part but can correspond to the conclusion made in the last section about the effect of the reflections on the parabolic mirrors. In all these measurements, contrary to the results obtained with vertical polarization upon entry, the polarization condition is well respected.

Analyzer position	Measurement number	Rotating QWP method (16 data points)
After the focal plane	45	[1 ; 0.018 ; -0.129 ; -0.982]
	46	[1 ; 0.040 ; -0.169 ; -0.981]
After the Lyot stop	47	[1 ; 0.037 ; 0.157 ; 0.975]
	48	[1 ; 0.043 ; 0.172 ; 0.976]

Table 8.20: Stokes vectors obtained by forcing a RH polarization in entry just after the DM part and analyzing the state of the polarization at the focal plane and at the Lyot stop, with the rotating QWP method using 8 data points.

8.5.2 Polarizer before the focal plane

The hypothesis of the impact the parabolic mirrors will be quickly verified by making many sets of measurements with the circular polarizer just before the focal plane and the analyzer right after. These measurements will ensure that a precise circular polarization can be achieved upon entry. This new setup is similar to the one depicted in Figure 9.1, without the AGPM placed.
All the sets are represented in the following Table 8.21.

Measurement number	Entry circular polarization orientation	
	Left-handed	Right-handed
49	[1 ; 0.090 ; -0.027 ; -0.982]	[1 ; -0.101 ; 0.004 ; 0.987]
50	[1 ; 0.081 ; 0.027 ; -0.983]	[1 ; -0.087 ; -0.019 ; 0.989]
51	[1 ; 0.089 ; 0.012 ; -0.972]	[1 ; 0.245 ; -0.022 ; 0.955]
52	[1 ; 0.079 ; -0.010 ; -0.973]	[1 ; 0.238 ; -0.012 ; 0.952]
53	[1 ; 0.115 ; -0.021 ; -0.965]	[1 ; -0.094 ; 0.023 ; 0.968]
54	[1 ; 0.112 ; -0.029 ; -0.962]	[1 ; -0.094 ; 0.024 ; 0.967]
55	[1 ; -0.140 ; 0.035 ; -0.969]	[1 ; 0.140 ; -0.041 ; 0.966]
56	[1 ; -0.149 ; 0.024 ; -0.971]	[1 ; 0.114 ; -0.034 ; 0.959]
57	/	[1 ; 0.146 ; -0.043 ; -0.968]

Table 8.21: Stokes vectors obtained by forcing a circular polarization in entry (Left-handed and right-handed) just before the focal plane and analyzing the state of the polarization after the focal plane with the rotating QWP method using 8 data points.

To have more context about these results, it is important to note that they have not been measured at the same time. Four different sets are represented here. Measurements 49 and 50 corresponds to the first set. A second set is created with measurements 51 and 52, a third set with measurements 53 and 54 and the last set with measurements 55, 56 and 57.

On the one hand, with respect to the results in the Table 8.20, the oblique parameter

contribution is no more the main concern. It confirms that it could be caused by the reflection onto the parabolic mirror between the polarization filter and the analyzer in the previous setup. On the other hand, the second parameter has now a higher contribution and is variable. Gradually, with each measurement, attempts are made to rectify the setup by implementing improvements, which appear to be the cause of the various fluctuations in the Stokes vectors. The first two sets are made in the same conditions on two different days. For the third set, the analyzer has been fixed to the mount of the focal plane to increase the accuracy in the alignment between the two elements. However, it is not guaranteed that the focal plane is precisely perpendicular to the orientation of light. Until now, the reference angle used for the linear polarizers are the same from the beginning of the measurements. However, since the Stokes parameters are not better by improving the setup, a new characterization of the reference angle for the transmission axis of the linear polarizer could improve the results. This is what is done for the last set (measurements 55, 56 and 57).

Most of the results in Table 8.21, are comparable to results from Section 7 where the imperfections of the LP and the QWP were evaluated. Results obtained in Tables 7.7 and 7.8 considering imperfect retardance of the QWP and deviation of the transmission and fast axis present higher variations than most of the results presented in Table 8.21. The perturbations encountered in these results are then more than certainly caused by the inherent imperfections of the polarizer and can be resolved by optimizing the setup.

The analyzer is adjusted to allow LH polarized light to pass through. By rotating the transmission axis of the LP in the circular polarizer, the maximum intensity reached corresponds to a configuration where the polarization filter is set LH polarization, while the minimum intensity corresponds to RH polarization at the input. This is processed without modifying the reference angle of the quarter wave plates. Once the minimum and the maximum intensity are found for specific orientations of the first linear polarizer, the LP inside the analyzer is rotated to verify if a lower minimum and a higher maximum are achievable. Once the lowest minimum and the highest maximum intensities are found, polarization measurements are made with the new references for both LP (the one in the polarization filter and the one in the analyzer). This leads to measurements 55, 56 and 57 from Table 8.21 which gives non satisfying results. The second and third Stokes parameters are not improved with respect to the previous measurements. It means that no purer polarization is reachable with this polarization filter setup upon entry. The optimisation must be done in another way.

8.5.3 Circular polarizer optimization

The circular polarizer is optimized in the setup represented in Figure 9.1. The idea is to make several polarization measurements while rotating the first polarizer in order to find the purest LH and RH polarization. The evolution of the Stokes parameters for a left-handed circular polarization measured is represented in Figure 8.6. Iterations in the following graphs correspond to the measurements made after a specific modification in the orientation of the characteristics axis (transmission axis or fast axis). The impact of these modifications on the Stokes vector are evaluated at each iteration and the next modification

is made accordingly to converge to the purest circular polarization.

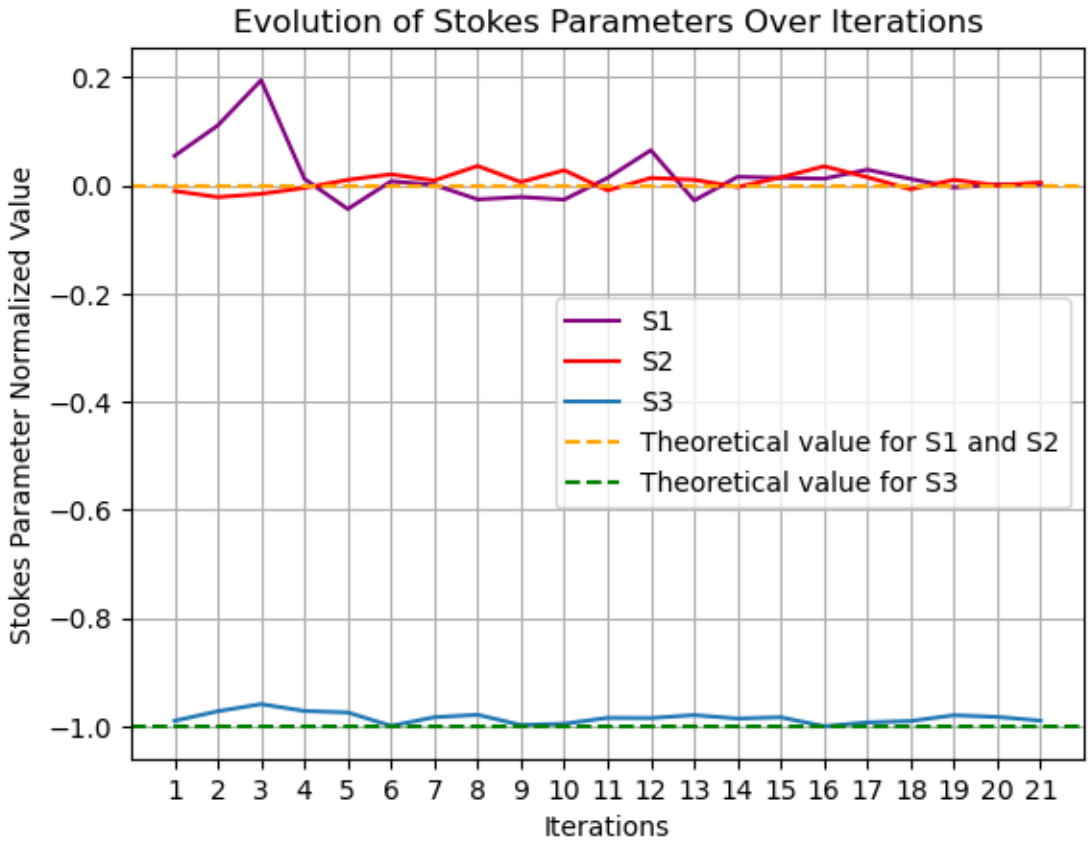

Figure 8.6: Determination of the entrance polarization setup by optimization of the Stokes parameters values for LH polarization.

Even if other iterations, such as the 6^{th} iteration ([1 ; 0.008 ; 0.021 ; 0.999]), seem to be good candidates for the purest RH polarization in entry, the setup associated to the last iteration offers the most constant results. Once a setup produces good results for LH polarization, it is tested for RH polarization, the objective being to find the setup that will produce the purest LH and RH polarizations. That means that the orientation of the transmission axis in the circular polarizer which gives the purest LH should be in theory the closest to 90° from the transmission axis orientation that gives the purest RH polarization. In a circular polarizer, a LH polarization should be obtained with a angle difference of +45° between the fast axis of the QWP and the transmission axis of the LP while a RH polarization should be obtained with the orientation of the transmission axis at 90° from the previous orientation, so at -45° with respect to the fast axis of the QWP. In theory the handeness is inverted when the transmission axis of the LP undergoes a rotation of 90°.

Based on this optimization for the case of the LH polarization, the setup obtained is used to measure the RH polarization produced by rotating the LP by 90°. Starting from the 17^{th} iteration, the RH polarization produced is measured and the results are displayed in

the following graph.

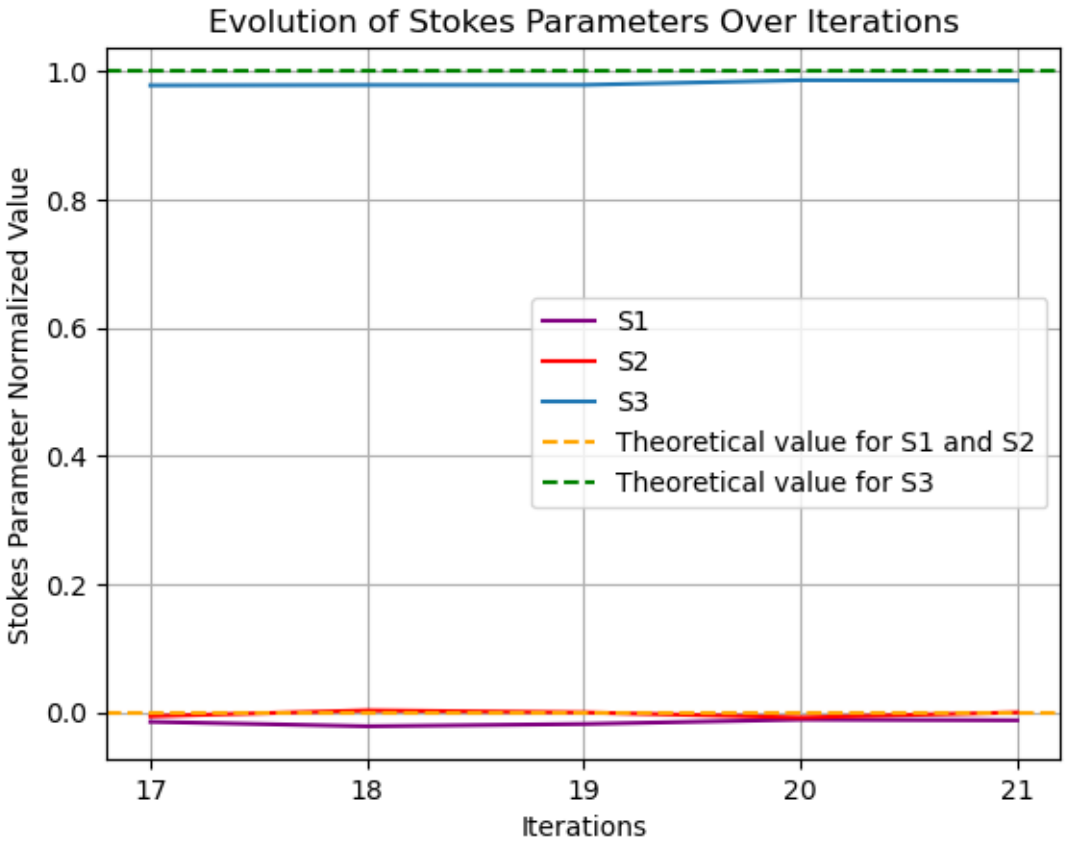

Figure 8.7: Determination of the entry polarization setup by optimization of the Stokes parameters values for RH polarization.

The 21^{th} iteration is the one that gives more constant results and the closest ones to the theoretical polarization states.

Progressively with the iterations, the analyzer reference angles have also been tested. To obtain these results, the reference angle for the QWP in the analyzer has been modified by 1° and the horizontal reference of the last LP has been rotated by 2°, which gives these last results.

8.5.4 Final results

The values of the Stokes parameters obtained at the final iteration for both entrance polarization are summarized in Table 8.22.

These results confirm that the too high linear contribution present in results from Table 8.21 comes from the inaccuracy on the orientations of the characteristic axis of both the circular polarizer and the analyzer as described in Section 7. As expected, a purer state of

Entry polarization	Iteration number	Rotating QWP method (8 data points)
LH	21	[1 ; 0 ; 0.01 ; -0.99]
RH	21	[1 ; -0.01 ; 0 ; 0.99]

Table 8.22: Stokes vectors obtained by filtering a circular polarization in entry (LH and RH) just before the focal plane and analyzing the state of the polarization after the focal plane with the rotating QWP method using 8 data points.

polarization is achieved with this setup. This was expected since there is no perturbation of the flux between the polarization filter and the analyzer in this setup, the probleme can only come from the setup itself. More than that, the analyzer is now trustable and the measurement method can be used with more confidence in the obtained results, with the highest precision reachable manually. The optimization of both the circular polarizer and the analyzer will have a crucial role in the performance of the dual polarization setup.

Part III

Dual polarization setup

9. Dual-polarization setup performance

The role of the dual-polarization setup is to be able to effectively select one of the circular polarization in order to obtain coronographic images whith sufficient diversity to retrieve phase informations about the wavefront at the entrance pupil. The performance of the dual-polarization setup is evaluated in two ways. Firstly, through the extinction ratio which gives the performance of the circular polarization selection with and without the AGPM. In this first part, the AGPM is focused off-axis to consider only the half wave plate performance. As represented in Equation 2.1, the half wave plate can be imperfect and give a non-ideal retardance with a certain amount of leakage (c_V). This first feature is limited by the precision of the circular polarizer and the analyzer used in addition to the proportion of leakage produced by the half wave plate. The second analyzed effect is the intrinsic performance of the AGPM through the rejection ratio which is its ability to diffract the on-axis light oustide the Lyot stop. Wavefront errors in phase and amplitude are limiting this performance and represent the issue behind the wavefront sensing. More than that, this performance is also limited by the ability to center with accuracy the AGPM with the light beam focused in the focal plane. It is expected that the performance of the polarization setup doesn't limit the intrinsic performance of the AGPM and this will be verified in this section.

9.1 Setup description

The optimized setup used to assess these performance is shown in Figure 9.1. A first circular polarizer composed of a LP followed by a QWP with its fast axis parallel to the x-axis is placed before the focal plane just as for the circular polarization measurement setup. As it can be seen in the picture, the first linear polarizer is fixed to the first quarter wave plate to ensure an alignement between the two elements. This first polarizer allows to produce LH or RH polarized light. Then the light is focused onto the focal plane where the AGPM can be placed off and on-axis. After that, an analyzer is placed which is composed of a QWP with its fast-axis horizontal at 0° followed by a LP. The role of this second polarizer is to select between RH and LH polarized light, depending on what is to be analyzed and measured. In the final setup, the second QWP and LP are both fixed in the same cage with the mount in the focal plane to ensure alignement between both compounds and the AGPM.

However, at first, the two last compounds are dissociated from each other and from the focal plane mount. The alignement of the setup is not granted and the first results will bear witness of that. The second QWP is mounted on the rotating mount in order to use the same analyzer for potential future polarization measurements (including the optimization of the incoming polarization state presented before in Section 8.5). All compounds in the final setup are aligned with the mount in the focal plane but it isn't granted that the focal plane mount is actually perpendicular with high accuracy to the direction of light. A mar-

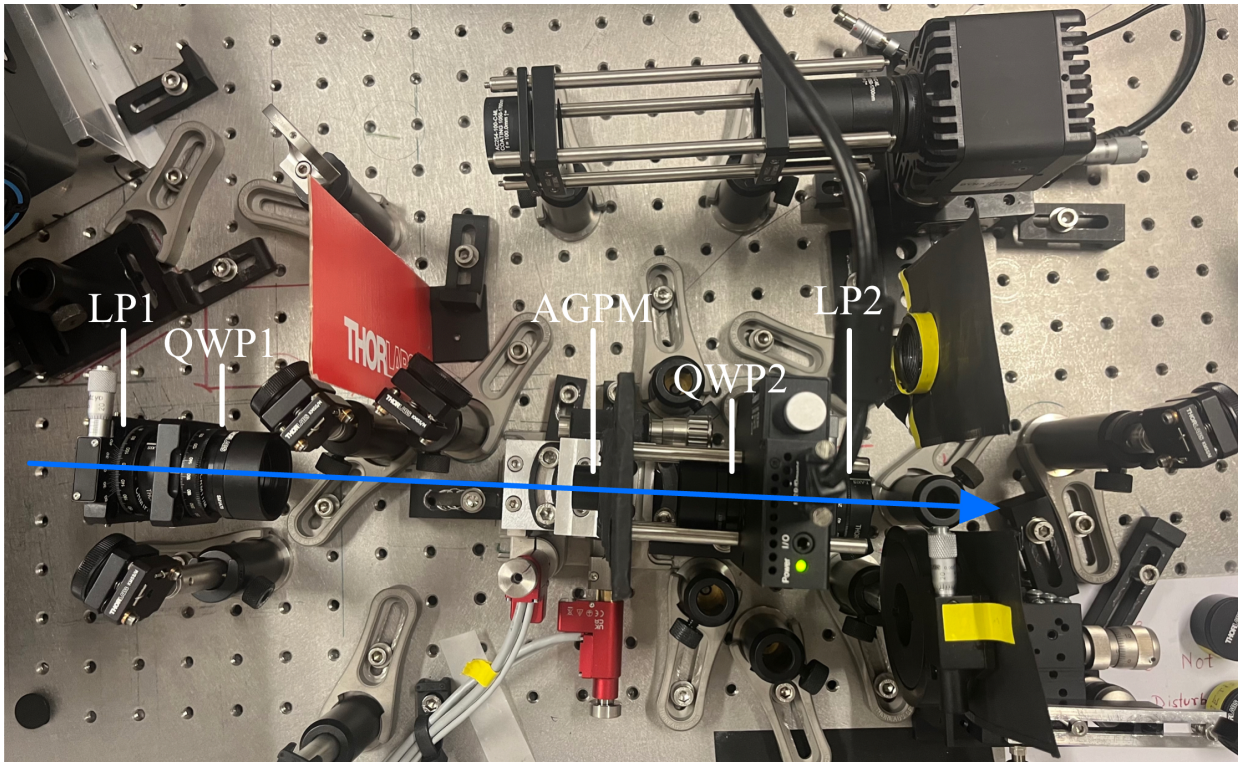

Figure 9.1: Vortex performance measurement final setup. The blue arrow representing the direction of the light flux.

gin of error can occur because of this potential misalignement which can induce unwanted refraction, deviation of the light or more variations in the retardance of the different wave plates.

By giving an example using LH polarization state upon entry, the behaviour of the polarization state with and without the AGPM placed is presented here. In the first setup, without the AGPM, the polarization is not affected when focused onto the focal plane and the RH polarization will remain the same. As explained previously, both QWP plate are firstly fixed with their fast axis parallel to the horizontal, as it is represented on both schemes in Figures 9.2 and 9.3. This is chosen arbitrarily to move only one type of component (the LPs). Moreover, the second LP must be rotatable for the polarization measurements using the same setup. With this convention, in order to obtain LH polarization upon entry, the first LP is set to 45°. The polarization doesn't change between both QWPs and a LH polarization being retarded by $\pi/2$ gives linear polarized light at 135°.

In the second setup represented in Figure 9.3, the polarization undergoes the effect of the half wave plate. With respect to the accuracy of the retardance of the wave plate, the circulary polarized light switches of handedness. The resulting RH polarized light is changed into linearly polarized light at 135° by the second QWP.

Then, in order to add more clarity to the future measurements, considering that only the

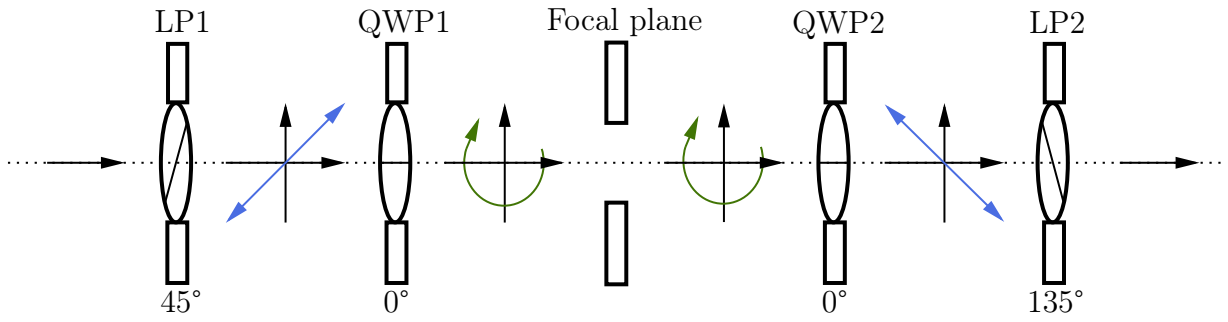

Figure 9.2: Evolution of the polarization state of de light along the setup without the AGPM placed.

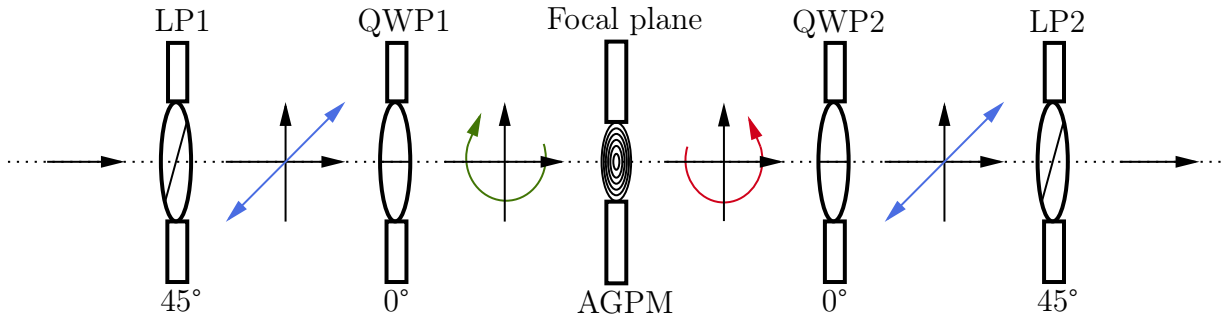

Figure 9.3: Evolution of the polarization state of the light along the setup with the AGPM placed.

linear polarizer will be manipulated, the Table 9.1 summarizes which configuration gives the maximum or the minimum intensity, the extinction and rejection ratio computed being nothing more than contrasts.

LP2 \ LP1	45°	135°
45°	Min	Max
135°	Max	Min

LP2 \ LP1	45°	135°
45°	Max	Min
135°	Min	Max

Table 9.1: Configuration to obtain the minimum and maximum intensities in both cases, without the AGPM (left) or with the AGPM (right).

Therefore, if the transmission axis of the two polarizers are perpendicular to each other, the intensity will be maximum for the setup without the AGPM and if they are parallel, the intensity of the light in the image obtained will be minimum. And it's the opposite when the AGPM is placed.

9.2 Extinction ratio

The extinction ratio is defined by the ratio of the maximum intensity obtained by modulating the analyzer on the same polarization than the entrance polarization and the minimum intensity obtained by cancelling the light upon entry with an orthogonal polarization after the focal plane. Theoretically, the setup without the AGPM and with the AGPM off-axis should give nearly the same results in terms of extinction ratio. With a perfect dual polarization setup, the difference in contrast between the two configurations (with and without AGPM) should come only from the imperfect retardance of the half wave plate and correponds to the leakage. More than that, the same contrast should be attainable with both polarization upon entry (LH and RH).

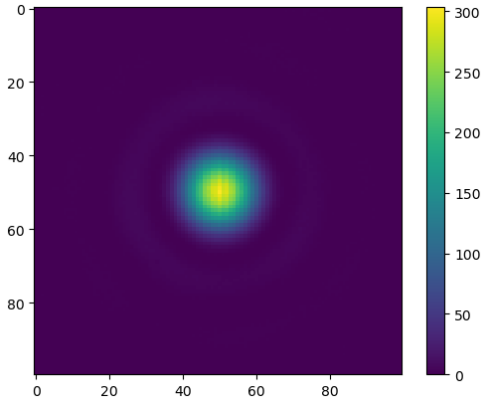

(a) Without AGPM
LP1 = 45°, LP2 = 45°,
$I_{median} = 62.8$, $I_{sum} = 70.1e3$,
$I_{max} = 303.8$.

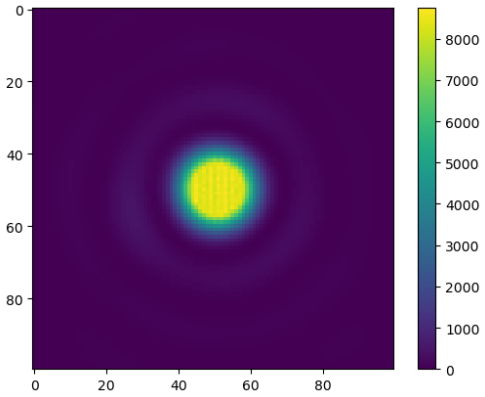

(b) With AGPM
LP1 = 45°, LP2 = 45°,
$I_{median} = 3290.6$, $I_{sum} = 3.1e6$,
$I_{max} = 8.8e3$.

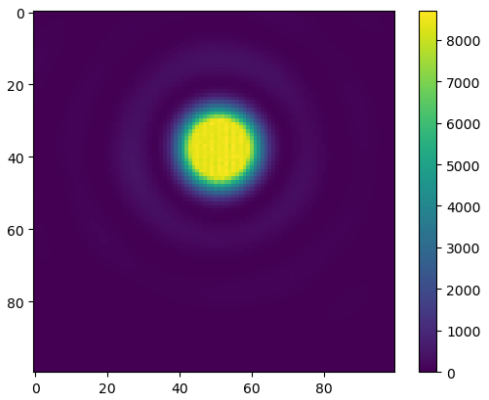

(c) Without AGPM
LP1 = 45°, LP2 = 135°,
$I_{median} = 3.9e3$, $I_{sum} = 3.4e6$,
$I_{max} = 8.7e3$.

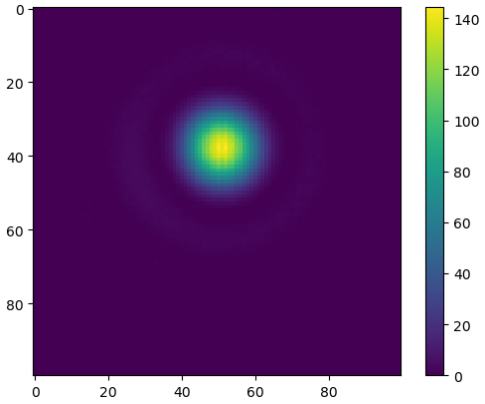

(d) With AGPM
LP1 = 45°, LP2 = 135°,
$I_{median} = 31.6$, $I_{sum} = 34.5e3$,
$I_{max} = 144.5$.

Figure 9.4: Comparison bewteen extinction ratios obtained with and without the AGPM placed with LH polarized light filtered.

The goal is to find a setup whose extinction ratio is the highest to ensure sufficient precision on the selected polarization state and the highest contrast limit reachable. In order to determine a target value, another contrast is used as comparison, the rejection ratio. In light of the results previously obtained in A. Jolivet [1], a rejection value of 2092 ± 119 could be achievable for the AGPM used with the L2 filter. However, this result corresponds to a particularly performant setup. For this work, the objective of a rejection ratio more recently obtained of 1000 is set. This objective of a contrast of 1000 is fixed also for the extinction ratio. With an imperfect dual polarization setup, the limitation on the contrast can come from the limits of the setup and the manipulations: the precision of the orientation and reference angles of the different compounds and from the imperfect retardance of the QWP, which was presented in Section 7.

At first, the results obtained with both entrance polarization (LH and RH) will be considered and compared. The mean intensity, the maximum and the sum of intensities are summarized in the caption of the different figures. Full images are represented in Figure 9.4 but an aperture mask is applied before computing the intensity values.

The first feature observed in Figure 9.4 is the saturation in the images corresponding to the configurations which give a maximum intensity in Subfigures 9.4b and 9.4c. This is quickly verified by plotting the corresponding central PSF of both images. In Figures 9.5a and 9.5b, a plateau is visible as if the top of the PSF were cut off, and this is due to camera saturation as explained in Section 2.2.4. The plateau appears just above 8000 counts, the intensity count must be verified first in the software before acquiring any image. This occurred due to the removal of the ND filter and could have been anticipated as measurements at maximum intensity were conducted. The ND 1.0 filter will be placed again for future measurements without the AGPM and with the AGPM off-axis.

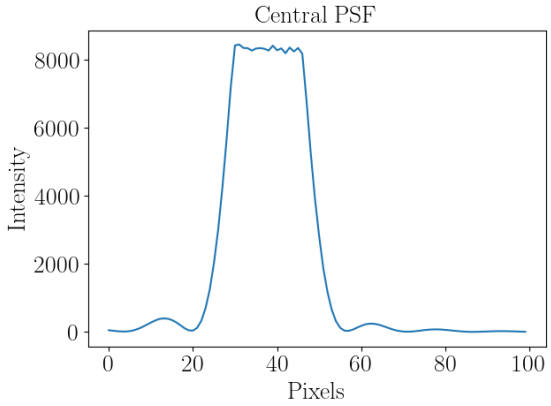

(a) PSF obtained with maximum intensity without the AGPM.

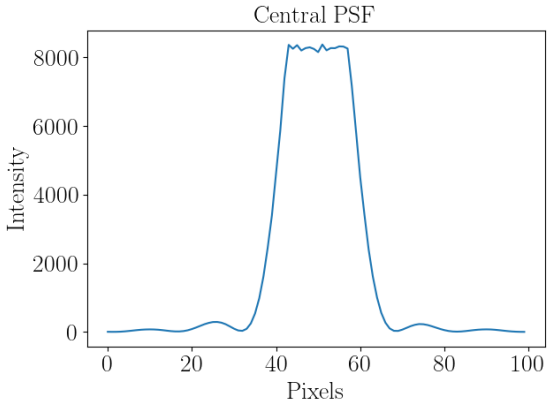

(b) PSF obtained with maximum intensity with the AGPM.

Figure 9.5: PSF of saturated images at maximum intensity with LH polarization upon entry.

The extinction ratio for this configuration can't be determined because of the saturation.

For this set, only the contrast obtained with entrance RH polarized light in following Figure 9.6 can be evaluated. When switching the polarization state upon entry by rotating the first LP to 135°, the results obtained are expected to be similar. However the light source polarization may have a greater proportion of one orientation of circular polarization over the other and this can vary from one set of measurements to the other as determined in Section 8.1. It is then expected that the intensity count is depending on the polarization state filtered in the first analyzer.

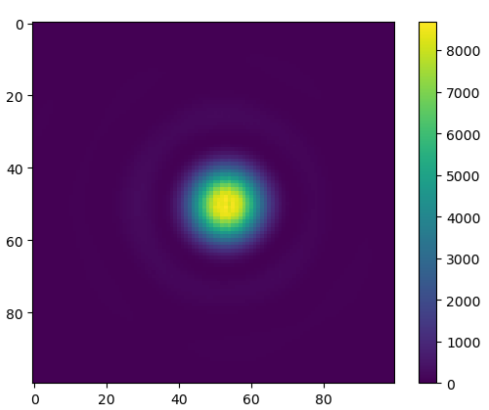

(a) Without AGPM
LP1 = 135°, LP2 = 45°,
I_{median} = 2e3, I_{sum} = 2.2e6,
I_{max} = 8.7e3.

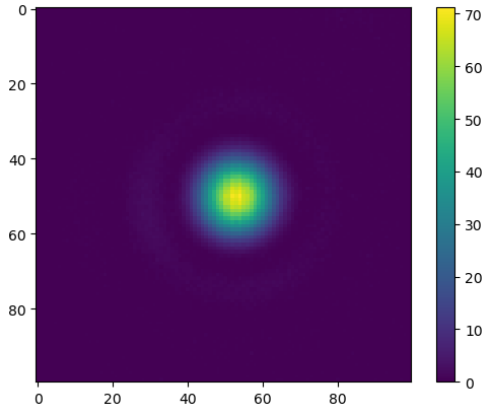

(b) With AGPM
LP1 = 135°, LP2 = 45°,
I_{median} = 15.2, I_{sum} = 16.8e3,
I_{max} = 71.3.

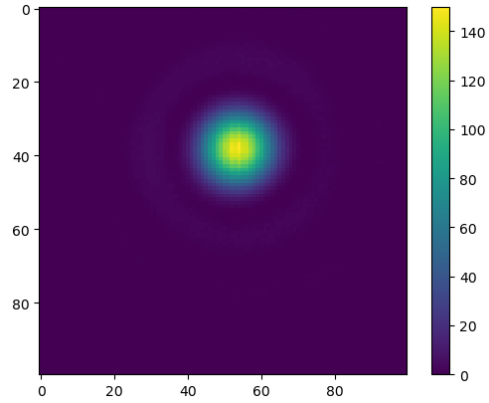

(c) Without AGPM
LP1 = 135°, LP2 = 135°,
I_{median} = 30.9, I_{sum} = 34.9e3,
I_{max} = 150.1.

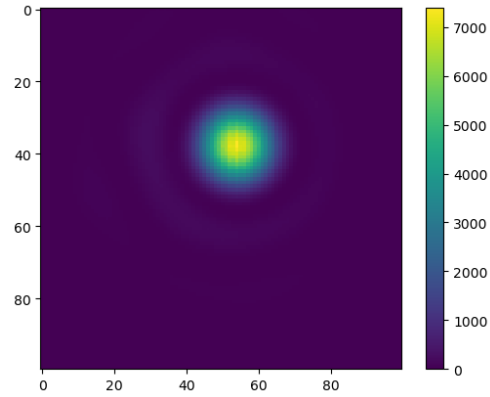

(d) With AGPM
LP1 = 135°, LP2 = 135°,
I_{median} = 1.6e3, I_{sum} = 1.8e6,
I_{max} = 7.4e3.

Figure 9.6: Comparison bewteen extinction ratios obtained with and without the AGPM placed with RH polarized light filtered.

The PSF in Figure 9.6a and 9.6d obtained with RH entrance polarization are less saturated than the one observed in Figure 9.4. The corresponding PSF are displayed in Figure

9.7 to compare with the previous PSF displayed in Figure 9.5.

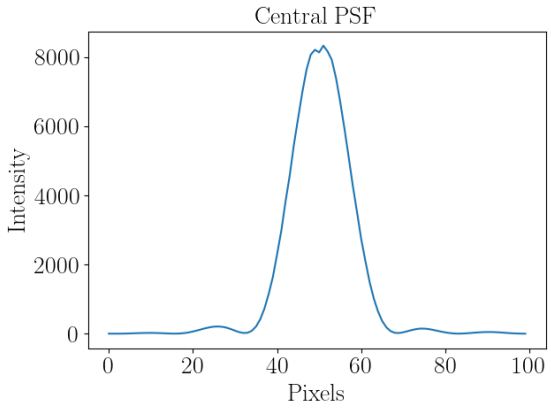

(a) PSF obtained without the AGPM with maximum intensity.

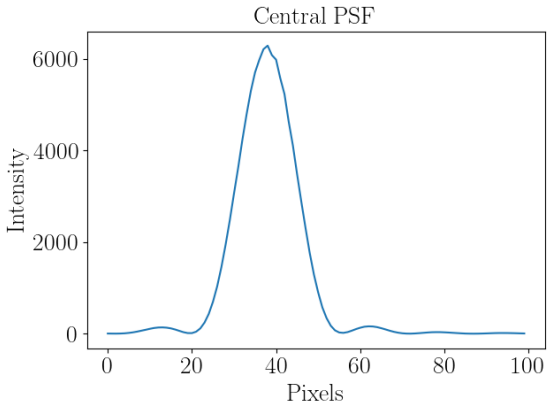

(b) PSF obtained with the AGPM with maximum intensity.

Figure 9.7: PSF of saturated images at maximum intensity with RH polarization upon entry.

In fact, the saturation pattern also appears above an intensity of 8000, but it can be observed that this corresponds to the peak of the PSF, in contrast to the PSF in Figures 9.5, where the saturation cuts the PSF lower relative to its peak. The maximum intensity obtained with a RH polarization is then lower than with LH polarization upon entry. This can be explained by the unknown state of the polarization of the source. Nevertheless, a first approximation of the extinction ratios can be evaluated for the second results summarized in Figure 9.6 with RH entrance polarization since the maximum intensity has little impact on saturation. By comparing the extinction ratios computed with the median, the maximum and the sum of the intensities, the following results in Table 9.2 are obtained.

Setup / Photometry	No AGPM	AGPM
Median intensity	66	105
Sum intensity	65	103
Maximum intensity	58	104

Table 9.2: Extinction ratios obtained with and without the AGPM with RH polarization upon entry.

These first results of extinction ratio are not consistent with the theory. Indeed, since the difference between the two configurations is the presence of the AGPM, theoretically, the contrast obtained with the AGPM off-axis cannot be higher. If the leakage is really small, the contrast obtained with the AGPM can approach the one obtained without AGPM but not surpass it. The AGPM can only reduce the accuracy on the polarization state measured due to the presence of a certain proportion of leakage 2.1. The most logical explanation to

these results lies in the inaccuracy of the setup which has not yet been corrected through the alignmement improvement and the optimization presented in Figures 8.6 and 8.7.

Moreover, these results a too low with respect to the target extinction ration fixed to 1000. In order to obtain such a contrast with this setup, this latter must be improved .

9.2.1 Alignement optimization

The setup can be first improved by the alignement of the different compounds to the optical axis. An observable feature in the Figures 9.4 and 9.6 is the upward shift of the PSF when the second LP is rotated to 135°. This is probably due to the misalignement between the second LP and the optical axis which can induce a shift in the final image. As mentioned in the setup description, the optimized setup includes the fixation of the second QWP and LP together with the AGPM mount as represented in Figure 9.1. Concerning the circular polarizer before the focal plane, the LP and the QWP cannot be fixed directly to the AGPM mount such as the analyzer due to space constraints. However, better alignment is achieved by extending small rods from the AGPM mount to the polarization filter to ensure proper alignment between them. After repositioning, the rods are removed to avoid any unwanted reflections. This is done to improve the alignement between the added optical elements and the focal plane even if the alignement of the AGPM mount in the focal plane to the optical axis is not totally granted.

After the first step of the alignement of the setup, when only the configuration of the analyzer has been improved, a first set of measurements is made using the ND 1.0 filter to avoid any saturation. The ND 1.0 filter prevents the saturation but attenuates the incoming flux too much and the results obtained with the AGPM off-axis cann't be used to compute the extinction ratio. Indeed no resulting PSF is present in the image. The choice of the ND filter must be discussed case-by-case but rigorously noted in order to compare the intensity values properly in the same basis.

After the total alignement optimization of the alignement of the setup, a new mesurement set is made. The results obtained with a LH and RH entrance polarization are displayed in Figure 9.8 and 9.9.

It is difficult to compare the absolute values of the intensities of the images obtained with previous set of measurements due to the variation of the source. The high variation of the polarization state of the source is one of the main issues and conclusions of the Part II. The portions occupied by the different polarization states in the randomly polarized source light change with external conditions. The proportion of LH polarization and RH polarization in incoming light beam may vary, being higher or lower, respectively. Since the polarization is filtered before reaching the focal plane, the amount of light intensity passing through the filter can also be higher or lower, depending on the polarization state of the source light. This randomness prevents a strict comparison of the intensity values obtained in different images for two different sets, as they are often taken on different days or after the source has been switched off and on again. However, the extinction ratio is a robust value allowing

strict comparison when there is no saturation and enough flux.

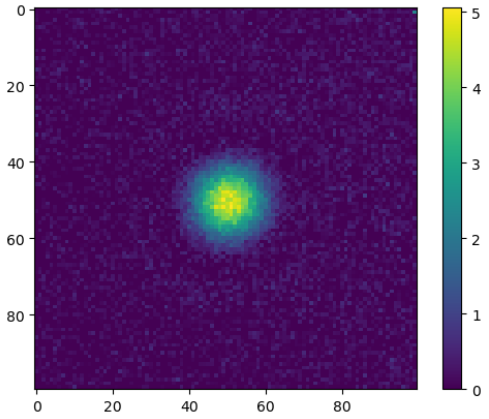

(a) Without AGPM
LP1 = 45°, LP2 = 45°,
I_{median} = 1.1, I_{sum} = 1.1e3,
I_{max} = 5.1.

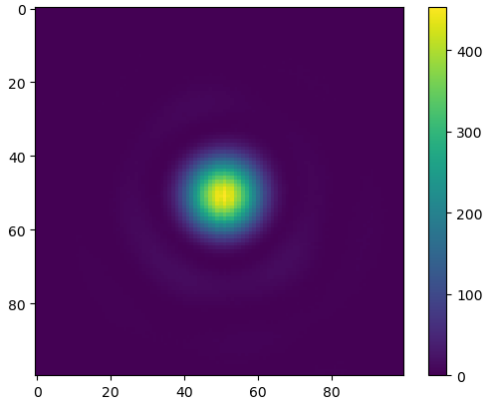

(b) With AGPM
LP1 = 45°, LP2 = 45°,
I_{median} = 103.7, I_{sum} = 11.1e3,
I_{max} = 453.8.

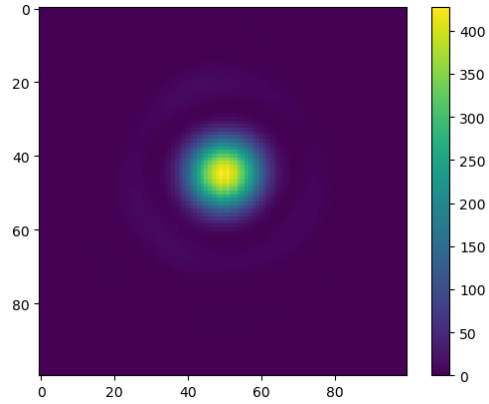

(c) Without AGPM
LP1 = 45°, LP2 = 135°,
I_{median} = 94.4, I_{sum} = 104.e3,
I_{max} = 428.

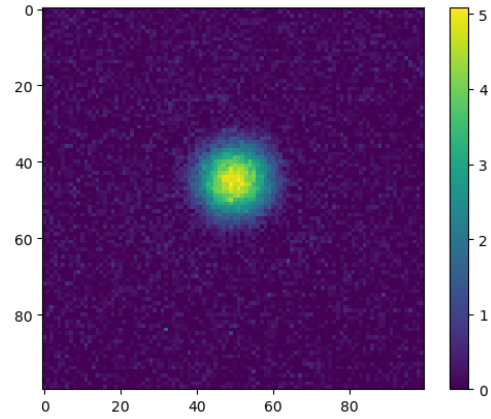

(d) With AGPM
LP1 = 45°, LP2 = 135°,
I_{median} = 1.2, I_{sum} = 1.2e3,
I_{max} = 5.1.

Figure 9.8: Comparison bewteen extinction ratios obtained with and without the AGPM placed with LH polarized light filtered with the analyzer fixed and the polarization filter aligned to the AGPM mount.

For once, there is neither saturation nor not enough flux for both circular entrance polarization. The extinction ratios obtained for the last results from Figure 9.8 and 9.9 are noted in Table 9.3. With this improved setup, constant and similar performance are found between the setup with and without the AGPM. The difference of contrast obtained with different entrance polarization cannot be compared with results from the first set of measurements due to the saturation obtained before. However, the extinction ratios obtained with orthogonal entrance polarizations give values with the same order of magnitude.

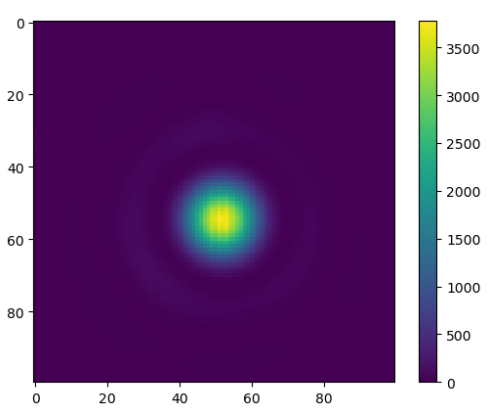

(a) Without AGPM
LP1 = 135°, LP2 = 45°,
I_{median} = 820.7, I_{sum} = 900.1e3,
I_{max} = 3.8e3.

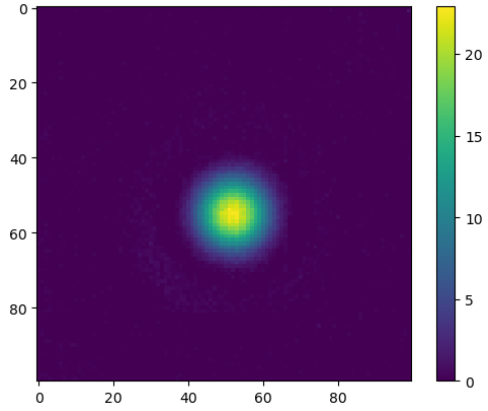

(b) With AGPM
LP1 = 135°, LP2 = 45°,
I_{median} = 4.6, I_{sum} = 5.2e3,
I_{max} = 22.9.

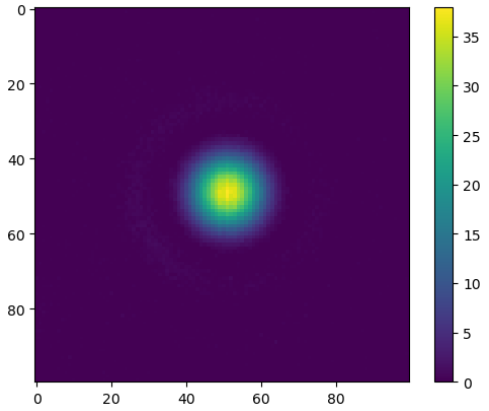

(c) Without AGPM
LP1 = 135°, LP2 = 135°,
I_{median} = 7.6, I_{sum} = 8.7e3,
I_{max} = 38.

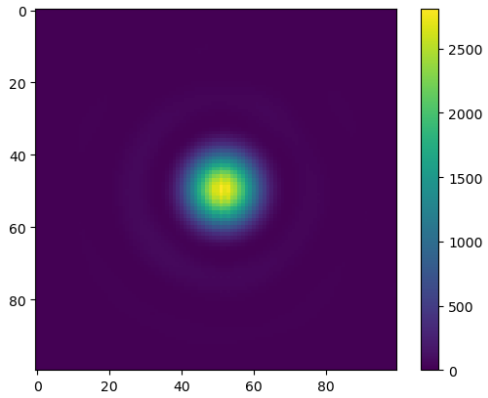

(d) With AGPM
LP1 = 135°, LP2 = 135°,
I_{median} = 610.8, I_{sum} = 660.8e3,
I_{max} = 2.8.

Figure 9.9: Comparison bewteen extinction ratios obtained with and without the AGPM placed with RH polarized light filtered after the alignement optimization of the setup.

With respect to the extinction ratios computed in Table 9.2, the values from Table 9.3 are indeed more constant from one setup to the other (with and without the AGPM), especially with the LH polarization upon entry. These ratios are relatively acceptable but, once again, the extinction ratios are improved when using the AGPM which is not physically accurate. Even if this difference is small, better results with the AGPM do not make sense. Now that the setup is aligned, the obvious error can come from the manipulations during the measurements and the inherent limitations of the optical components. This latter hypothesis will be solved in next section. As stated before, the contrasts obtained are still below the target value of minimum 1000. Some more improvements can be made.

Photometry	Entry polarization	No AGPM	AGPM
Median intensity	LH	85	86
	RH	108	132
Sum of the intensities	LH	88	89
	RH	104	126
Maximum intensity	LH	85	89
	RH	100	123

Table 9.3: Extinction ratios obtained with and without the AGPM after the optimization of the alignement of the setup.

9.2.2 Polarizer optimization

It is at this particular step that the polarization upon entry has been optimized. The optimization have been presented in Tables 8.7 and 8.6 in Section 8.5.

As the performances with LH and RH polarizations have resulted in consistent and relatively similar extinction ratios, only the LH polarized light case will be analyzed. After this circular polarizer optimization, the new set of measurements is represented in Figure 9.10. This set, as before, has been measured with the QWP in the analyzer to 0°. The correponding exctinction ratios are dispayed in Table 9.4.

Photometry	QWP2 orientation [°]	No AGPM	AGPM
Median intensity	0	80	1521
	90	1924	83
Sum of the intensities	0	80	1261
	90	1440	81
Maximum intensity	0	78	927
	90	1116	80

Table 9.4: Extinction ratios obtained with and without the AGPM with the QWP2 at 0° and 90°.

Once again the configuration with the AGPM has a much higher contrast in this case. Since the two configurations were expected to produce similar contrast limited by the leakage in the case of the AGPM, this really high difference (almost a factor of 20) is hard to explain. When looking to the resulting PSF in Figure 9.10, the issue seems to come from the minimum intensity configurations. The maximum intensity is lower with the AGPM than without due to the presence of the leakage which limits the pureness of the polarization coming to the analyzer. However, using the same argument, the minimum intensity should be higher with the AGPM due to the residual initial polarization state after the AGPM. These effects combined lead to a lower extinction ratio than without the AGPM. This is true in theory, because as it is seen in Figure 9.10d, the minimum intensity obtained with the AGPM is actually the lowest by more than a factor 10 which results in a much higher

contrast.

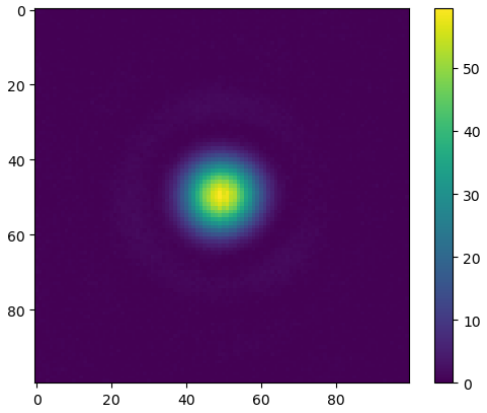

(a) Without AGPM
LP1 = 45°, LP2 = 45°, QWP2 = 0°
I_{median} = 12.8, I_{sum} = 14e3,
I_{max} = 59.5.

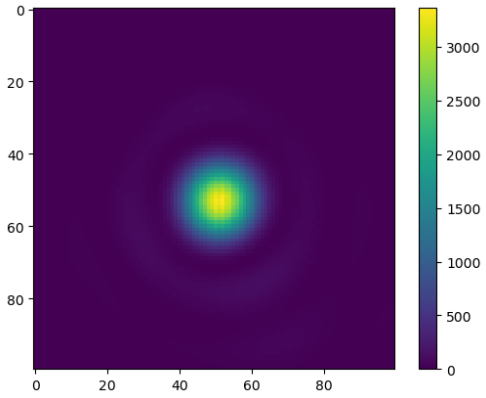

(b) With AGPM
LP1 = 45°, LP2 = 45°, QWP2 = 0°
I_{median} = 778.8, I_{sum} = 828.3e3,
I_{max} = 3.4e3.

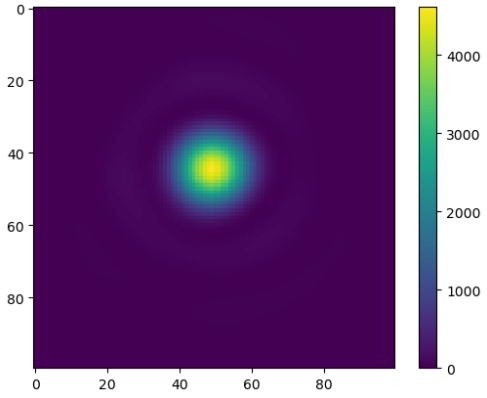

(c) Without AGPM
LP1 = 45°, LP2 = 135°, QWP2 = 0°
I_{median} = 1e3, I_{sum} = 1.1e6,
I_{max} = 4.6e3.

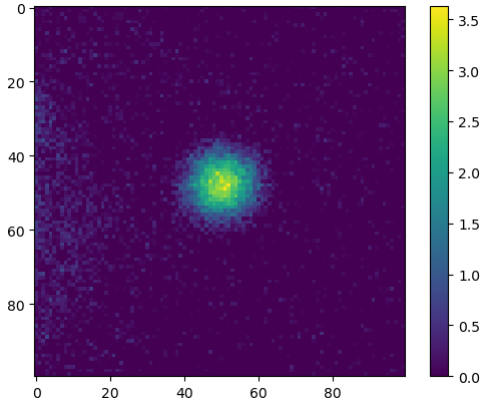

(d) With AGPM
LP1 = 45°, LP2 = 135°, QWP2 = 0°
I_{median} = 0.5, I_{sum} = 656.9,
I_{max} = 3.6.

Figure 9.10: Comparison bewteen extinction ratios obtained with and without the AGPM placed with LH polarized light filtered with the analyzer fixed and the polarization filter aligned to the AGPM mount and the second QWP set to 0°.

Since the entrance polarization has been optimized making the circular polarizer the most accurate, an hypothesis is that the orientation of the polarizer in the analyzer at 135° is particularly accurate. The setup could have been optimized in a way that the second LP at 135° is much more precise and closer to the optimal orientation than 90° away at 45°.

However, a configuration which such a contrast corresponds to a very good performance, higher than expected (1000). The downside of this configuration is that this high extinction

ratio is obtained only for the configuration using the AGPM. To retrieve a very low minimum without any AGPM, following the previous hypothesis, the minimum should appear in the configuration with the second LP at 135°. This is achieved by rotating the second QWP to 90°. In fact, the only effect induced by the rotation of the QWP is a change in the retard induced by the wave plate, from $\delta = \pi/2$ to $\delta = -\pi/2$. The maximum and the minimum obtained, using the same orientation for the first and second LP will be inverted and the minimum will appear for the second LP at 135°.

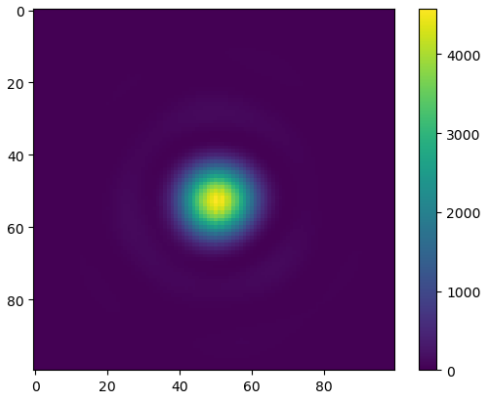

(a) Without AGPM
LP1 = 45°, LP2 = 45°, QWP2 = 90°
I_{median} = 1e3, I_{sum} = 1.1e6,
I_{max} = 4.6e3.

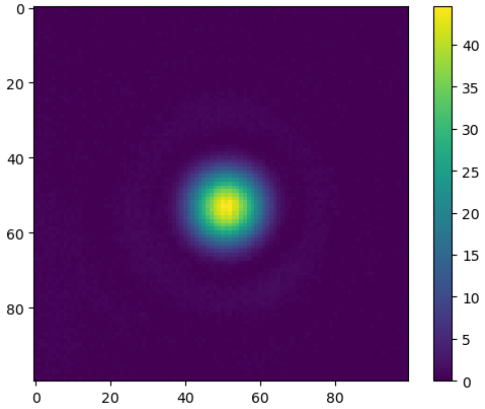

(b) With AGPM
LP1 = 45°, LP2 = 45°, QWP2 = 90°
I_{median} = 9.7, I_{sum} = 105.8e3,
I_{max} = 44.6.

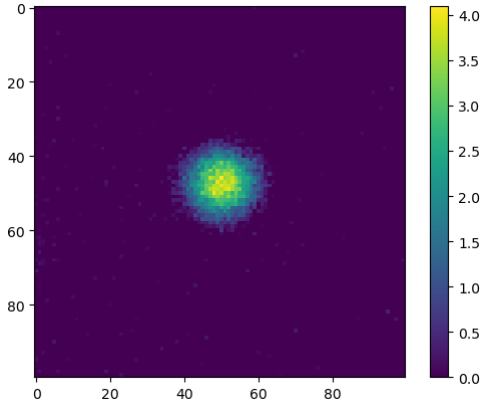

(c) Without AGPM
LP1 = 45°, LP2 = 135°, QWP2 = 90°
I_{median} = 0.5, I_{sum} = 765.1,
I_{max} = 4.1.

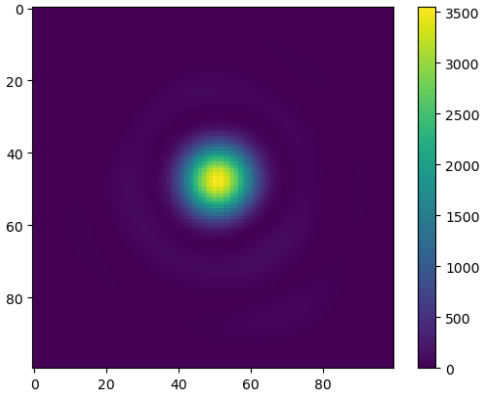

(d) With AGPM
LP1 = 45°, LP2 = 135°, QWP2 = 90°
I_{median} = 801.8, I_{sum} = 859.9e3,
I_{max} = 3.6e3.

Figure 9.11: Comparison bewteen extinction ratios obtained with and without the AGPM placed with LH polarized light filtered with the analyzer fixed and the polarization filter aligned to the AGPM mount and the second QWP set to 90°.

The results obtained with the QWP in the analyzer set to 90° are shown in Figure 9.11. The corresponding extinction ratios obtained are summarized in same Table 9.4 as before.

Even if the extinction ratios are not consistent in the same configurations, it is a good point that some configurations allow an efficient contrast with and without the AGPM. More than that, the highest contrast is obtained without the AGPM and the other maximum contrast which is obtained with the AGPM is a bit lower, which maybe can be an effect of the leakage.

9.2.3 Final results

The highest extinction ratio obtained outperforms the first expectations and is even comparable to the rejection ratios obtained in A. Jolivet [1]. In fact, the highest contrast obtained in a configuration only dependent of the accuracy of the circular polarizer and the analyzer corresponds to 1924. The highest extinction ratio obtained in a configuration with the AGPM, so dependent on both the accuracy of the polarization setup and the imperfect half wave plate, is about 1521. Due to the numerous improvements and optimizations, a configuration reaching a higher contrast than expected and even a comparable performance to the particularly good rejection ratios obtained in A. Jolivet [1] (2092 ± 119) is determined.

The objective was to achieve the highest extinction ratio possible in order to prevent from any limitation on the vortex performance which will now be assessed.

9.3 Rejection ratio

The main objective of the part III is to reach a configuration where the maximum extinction and rejection ratio are obtained. An acceptable extinction ratio is found in previous Section 9.2. The capacity of the AGPM to diffract the on-axis light outside of mask created by the Lyot stop can also be analyzed. This performance is characterized by the rejection ratio. The rejection ratio corresponds to the contrast between the intensity got off-axis and the intensity got on-axis. As stated in previous Section 9.2, this rejection ratio has already been evaluated in A. Jolivet [1] to 2092 ± 119. Again, the objective for the rejection ratio in this work is 1000 because of the particularly performant results obtained by A. Jolivet. The measurements of the rejection ratios are made in parallel to those made for the exctinction ratio in previous section.

9.3.1 AGPM centering

The AGPM is mounted on a motorized mount which is manipulable with the computer. This allows precise motion by inducing a relative movement to the initial position of the mount with a certain amount of relative "counts" in the limits of the mount. Contrary to the other elements of VODCA, functions to control this motorized mount are not yet implemented in Python. The centering of the AGPM is made manually by inducing relative motion before any measurement script execution. The centering of the AGPM on the light beam is so highly limited but will represent a good approximation.

In order to facilitate the centering, the ND filter is removed. When the AGPM is close to be centered on the focused light, the very low light flux makes it difficult to center the vortex. Therefore, the maximum flux possible is necessary to allow maximum accuracy. This won't lead to saturation due to the diffraction of the light induced by the AGPM center which attenuate considerably the light flux which reaches the camera.

9.3.2 Aberrations minimization

Because the set of measurements with the AGPM on axis have been made in parallel to the measurements for the extinction ratio, the setup has undergone the exact same optimizations as presented in previous Section 9.2. Measurements are made at different steps of the opimization process just as in previous section. To compute the rejection ratio, the results obtained in Figures 9.4 to 9.11 using the AGPM off-axis are compared to results obtained with the AGPM on-axis. Nevertheless, since the objective of the Part III is to find a configuration which allows good performance in terms of extinction and rejections ratios, it is logical to present the results obtained with the configuration which gave the best extinction ratio in previous section. This configuration is presented in Section 9.2.2.

However, an additional optimization has been added which is specific to the images obtained when centering the AGPM on the light beam. This optimization aims to reduce the impact of aberration inside the focal plane using the DM. An aberration minimization routine has been developped in A. Jolivet [1] and a similar routine is used in these measurements. This routine is based on a certain number of high order aberration modes and inject aberrations among these modes using the DM (in the case of these measurements, 10 high-order modes were used) in order to counter the effect of the aberrations in the focal plane. The routine iterate by adapting the magnitude of the aberrations injected until finding a satisfying minimum residual aberration value. This optimization is necessary when trying to assess the AGPM performance.

As for last results from previous section, only the LH as entrance polarization is anayzed. The results obtained with the same configurations as in Figure 9.10 are displayed in Figure 9.12.

The first image in Figure 9.12a is obtained with a configuration where the LP are parallel which gives the maximum intensity as summarized in Table 9.1. In this configuration the residual polarization due to the leakage is blocked by the analyzer. The pattern observed in Figure 9.13a mostly comes from the centering accuracy and the effects of the residual aberrations in the focal plane.

On the contrary, the second image in Figure 9.6b corresponds to the minimum intensity configuration (9.1). It represents the leakage and therefore the imperfection of the AGPM performance. The rejection ratio of the AGPM is evaluated in the configuration where the centering and aberrations effects are measured, the configuration corresponding to the maximum intensity.

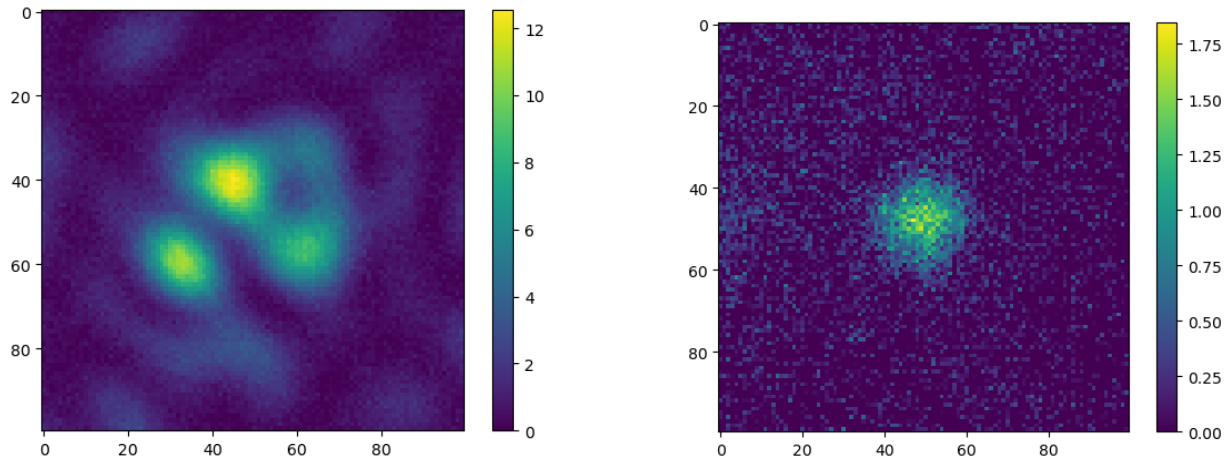

(a) AGPM on-axis
LP1 = 45°, LP2 = 45°, QWP2 = 0°
I_{median} = 4.1, I_{sum} = 9.4e3,
I_{max} = 12.6.

(b) AGPM on-axis
LP1 = 45°, LP2 = 135°, QWP2 = 0°
I_{median} = 0.5, I_{sum} = 406.5,
I_{max} = 1.8.

Figure 9.12: Images obtained by focusing the light onto the center of the AGPM, with L2 filter and aberration minimization routine using 10 first high order modes with QWP2 at 0°.

Configuration	Rejection ratio
LP1 = 45°; LP2 = 45°; QWP2 = 0°	1884

Table 9.5: Rejection ratios obtained with the AGPM centered after wavefront aberration minimization using 10 high-order modes with QWP2 = 0°.

By comparing the results obtained in Figure 9.12a with the results from Figure 9.10b, the resulting rejection ratio is obtained and displayed in Table 9.5.

The rejection ratio is computed considering that the ND 1.0 filter is used for results from Figure 9.10. The latter has been considered ten times higher due to the estimated 10% transimission of the ND filter from Figure 2.4. It seems that the AGPM is not precisely centered. In A. Jolivet [1], there's talk of a centering routine developped because of the great source of uncertainty which is the manual centering. If the AGPM is the most precisely centered, the rejection ratio would be better so the rejection ratios obtained with approximated centerings will correspond to minimum performances. However, the contrast obtained is very high (higher than expected) and is comparable to the one obtained by A. Jolivet [1]. Even if the results can be improved either by a more accurate centering or by a better aberrations minimization as the resulting PSF obtained in Figure 9.12 suggests, the value resumed in Table 9.5 is highly satisfying for this work.

As one of the hypothesis in previous Section 9.2.2 was that the second LP was the most accurate at 135°, the same measurements are made with the QWP at 90° to observe a

Configuration	Rejection ratio
LP1 = 45°; LP2 = 135°; QWP2 = 90°	2010

Table 9.6: Rejection ratios obtained with the AGPM centered after wavefront aberration minimization using 10 high-order modes with QWP2 = 90°.

maximum intensity with LP in the analyzer at 135°.

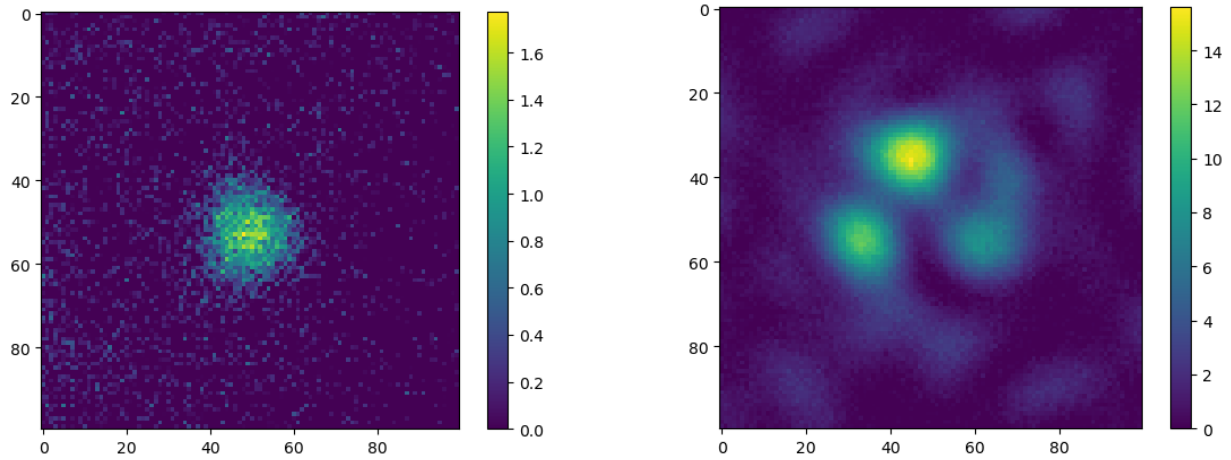

(a) With AGPM
LP1 = 45°, LP2 = 45°, QWP2 = 90°
I_{median} = 0.5, I_{sum} = 386.7,
I_{max} = 1.8.

(b) With AGPM
LP1 = 45°, LP2 = 135°, QWP2 = 90°
I_{median} = 4, I_{sum} = 9.6e3,
I_{max} = 15.6.

Figure 9.13: Images obtained by focusing the light onto the center of the AGPM, with L2 filter and aberration minimization routine using 10 first high order modes with QWP2 at 90°.

The corresponding rejection ratio computed using results from Figure 9.11 is displayed in Table 9.6.

Contrary to the extinction ratio, the rejection is not highly better when the QWP is set to 90°, the AGPM performance does not appear affected the same way by the accuracy on the second LP polarization. A slight improvement in the rejection ratio is observable but contrary to Figures 9.10 and 9.11, the results obtained in with the QWP at 0° in Figure 9.12 and with the QWP at 90° in Figure 9.13 are similar.

9.3.3 Final results

The optimization process described in Section 9.2.2 has been beneficial to the AGPM performance. Also the routine added using the DM has allowed to reduce the residual value of the high-order aberrations in the focal plane. The results obtained for the rejection ratio are comparable to the one obtained in A. Jolivet [1]. Rejection ratio up to 1884 and 2010

are obtained compared to 2092 ± 119 obtained by A. Jolivet. The same configuration that gives the higher extinction ratio gives a highly satisfying rejection ratio.

9.4 Global contrast

Very good performances were not expected due to some approximations and manipulations of the setup by hand which can lead to some imprecisions. However, a configuration allowing good extinction and rejection ratios is found which will be useful for wavefront sensing. Indeed, high extinction and rejection ratios ensure a very precise dual-polarization setup. The diversity expected and induced in the focal plane will be sufficient and will allow a good phase retrieval during wavefront sensing wich will be useful during wavefront reconstruction. This will be disccussed in following Part IV.

The total attenuation reachable by the setup can be computed by considering the extinction of the polarization setup combined with the rejection of the AGPM. This is determined by comparing the maximum intensity obtained with the polarization setup without the AGPM (when no extinction or ejection are considered) with the minimum intensity obtained with the AGPM centered (when both effects are considered). This corresponds to the intensity in the image from Figure 9.11a (obtained using ND 1.0) with respect to the intensity obtained in the image from Figure 9.13a. By computing the ratio of the median intensity, the total attenuation ratio is 21,274.

Giving the extinction and rejection ratios computed earlier, the total combined attenuation ratio could be expected higher. Due to the AGPM performance and the presence of leakage, the contrast is limited when considering the extinction with the polarization setup and the rejection with the AGPM on-axis combined.

Part IV

Wavefront Sensing and Control

10. Sign ambiguity

As stated in M. Quesnel et al. [10] and G. Orban De Xivry et al. [33], a sign ambiguity exists for even Zernike modes such as the astigmatism which is used in this section. This sign ambiguity is an important issue in Focal-Plane Wavefront Sensing when using a sign in-focused image. In fact, this sign ambiguity prevents from using a unique unambiguous focal plane intensity measurement to accurately retrieve the phase in the pupil plane. This sign ambiguity results in identical Fourier transforms of the pupil-plane electric field and its flipped and conjugated counterpart. If the Fourier transforms are identical, the distribution of intensity is also identical in the focal plane.

More than ensuring the purest polarization possible of the light incoming to the focal plane which gives a better accuracy on the performance of the vortex, the circular polarizer before the focal plane combined to the effect of the AGPM allows to lift any sign ambiguity about the aberrations induced in the focal plane. The ambiguity about the aberrations appear when the exact same image is retrieved when applying the same absolute magnitude of one type of aberration but with opposite signs. It is so impossible to distinguish the positive astigmatism from the negative one. It is possible to induce aberrations in the focal plane by applying specific modes with a certain amplitude on the wavefront using the DM. The DM will move the actuators in order to induce some aberrations such as oblique and vertical astigmatisms which are used in this section.

The setup for these measurements is composed of the circular polarizer and the AGPM. Before any measurement, the AGPM is centered as precisely as possible on the focused light beam and the aberrations are minimized with the DM routine on 10 high order modes as introduced in Section 9.3.2. Then, two types of measurements are made to verify that the ambiguity is well cleared up with this set up. The measurements are made by injecting vertical astigmatism since it corresponds to a mode which does not have a revolution symmetry, to be able to observe more easily the diversity.

10.1 Diversity on the sign

10.1.1 Results obtained on VODCA

In order to obtain an image which is dominated by the aberrations, an amplitude of 800 nm of vertical astigmatism is applied. The goal of this section is to verify that the dual polarization setup lifts the ambiguity. Therefore, the ambiguity is first demonstrated on the sign by showing images obtained by injecting ± 800 of vertical astigmatism with no circular polarizer before the AGPM. The resulting images are displayed in Figure 10.1.

The images presented in Figure 10.1 don't present a total ambiguity but this is only due to

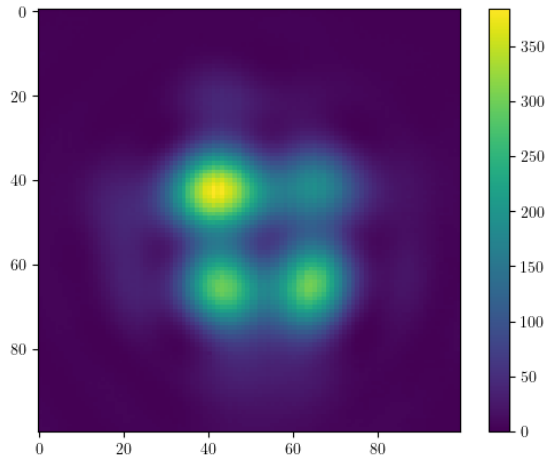

(a) Vertical astigmatism; amplitude = 800 nm;
No circular polarizer, AGPM on-axis.

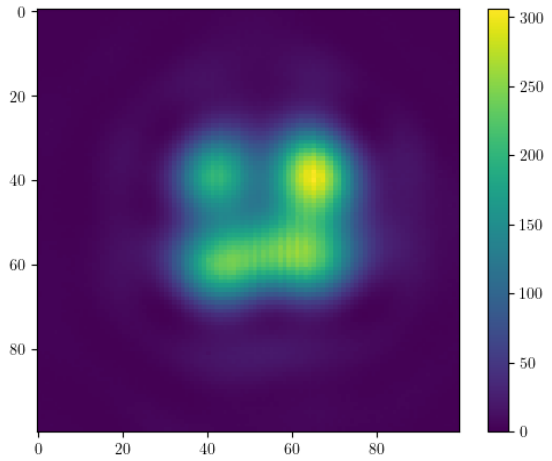

(b) Vertical astigmatism; amplitude = -800 nm;
No circular polarizer, AGPM on-axis.

Figure 10.1: Comparison between images obtained with vertical astigmatism induced by the DM using the AGPM on-axis without entrance circular polarization.

centering imprecisions. With a perfect centering, it would be difficult to observe a difference between the two images. On the other hand, the ambiguity can also be demonstrated by showing the images obtained when using the circular polarizer but without the AGPM. Negative and positive astigmatism are applied and compared in Figure 10.3.

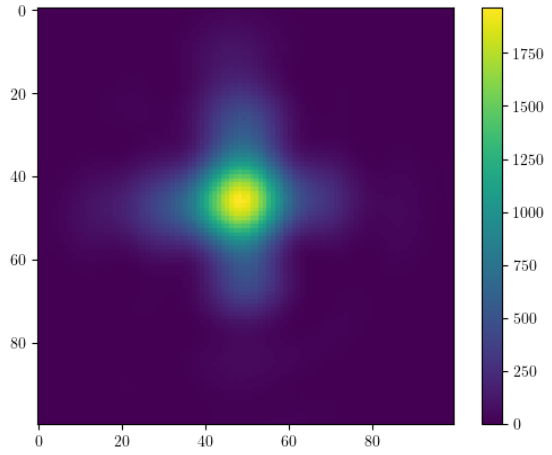

(a) Vertical astigmatism; amplitude = 800 nm
LP1 = 45°, without AGPM.

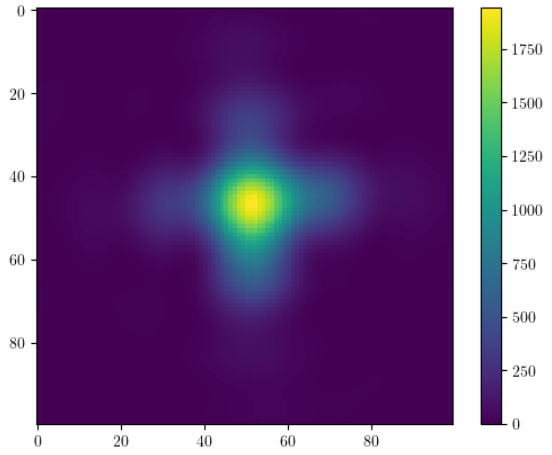

(b) Vertical astigmatism; amplitude = -800 nm
LP1 = 45°, without AGPM.

Figure 10.2: Comparison between images obtained with vertical astigmatism induced by the DM without using the AGPM.

The ambiguity is more visible in this case since that, contrary to coronagraphic imaging,

this is only normal imaging and this requires much less precision than AGPM centering.

The dual polarization setup using the AGPM is now used with LH entrance polarization and the results obtained with ±800 nm of vertical astigmatism are compared.

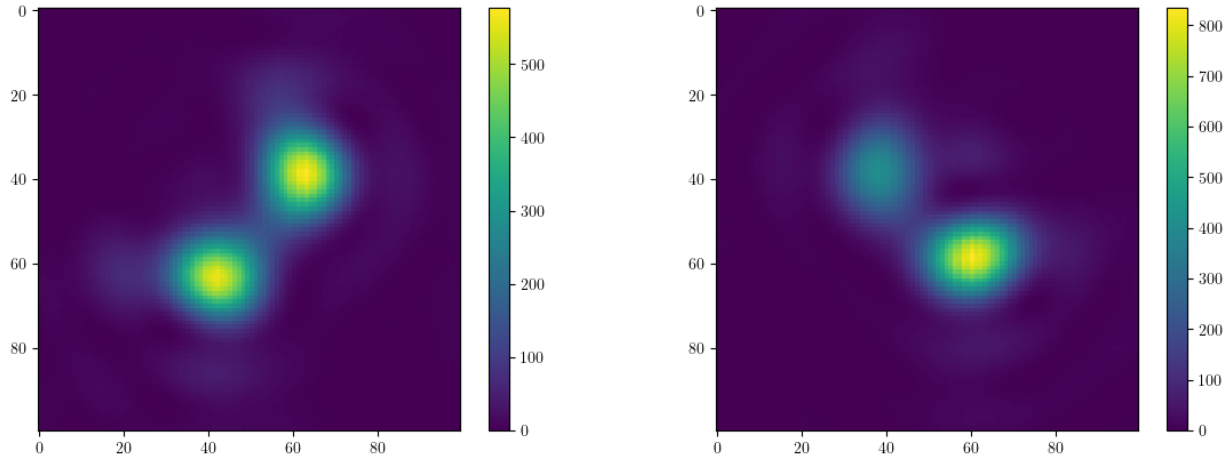

(a) Vertical astigmatism; amplitude = 800 nm LP1 = 45°, AGPM on-axis.

(b) Vertical astigmatism; amplitude = -800 nm LP1 = 45°, AGPM on-axis.

Figure 10.3: Comparison between images obtained with vertical astigmatism induced by the DM using the AGPM on-axis with LH circular entrance polarization.

The pattern has clearly rotated about 90° which confirms enough diversity and the lifting of the ambiguity using this setup. Moreover, the patterns observed in Figure 10.1 seem to correspond to a combination of the patterns obtained in Figure 10.3. However, the pattern seems oblique more than vertical although the aberration induced was vertical astigmatism. Even though, vertical astigmatism is clearly observed in normal imaging from Figure 10.2. This can be discussed by comparing with results obtained through simulations.

10.1.2 Results obtained by simulations

In order to validate the results obtained in Figures 10.1 and 10.3, simalutions are executed considering the same parameters. First, the results obtained without circular polarizer with ±800 vertical astigmatism are displayed.

During the simulations, the AGPM can be considered perfectly centered which gives a total ambiguity. The images obtained in Figure 10.4 are indeed perfectly identical. The results obtained on VODCA in Figure 10.1 have a pattern which tends to the one obtained with the simuations but is limited by the imprecised centering and the residual aberrations from the aberration minimization routine which can impact the pattern obtained. Hereunder are displayed the images corresponding to the combination of the circular entrance LH

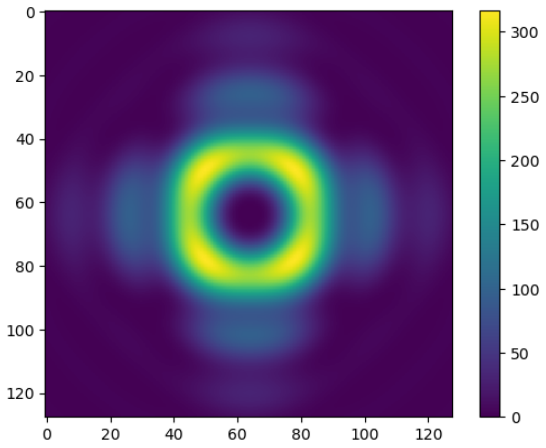

(a) Vertical astigmatism;
amplitude = 800 nm;
No circular polarizer, AGPM on-axis.

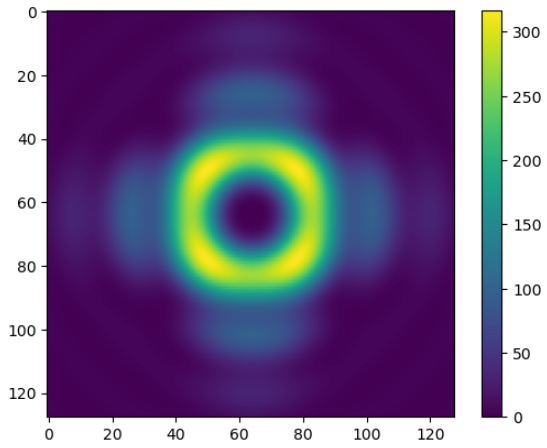

(b) Vertical astigmatism;
amplitude = -800 nm;
No circular polarizer, AGPM on-axis.

Figure 10.4: Comparison between images obtained with vertical astigmatism induced by the DM considering the AGPM on-axis obtained through simulation without circular entrance polarization.

polarization with the vortex effects obtained through simulations. The results obtained

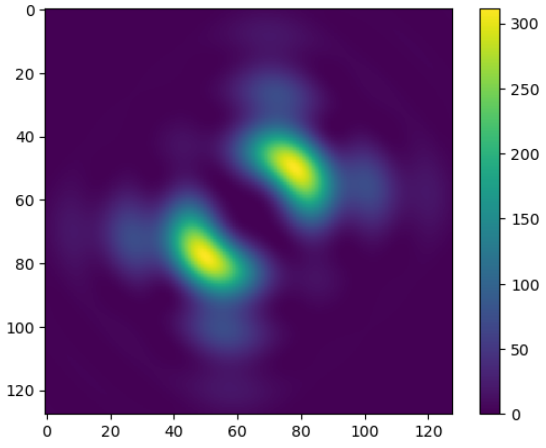

(a) Vertical astigmatism;
amplitude = 800 nm,
LH polarized light upon entry.

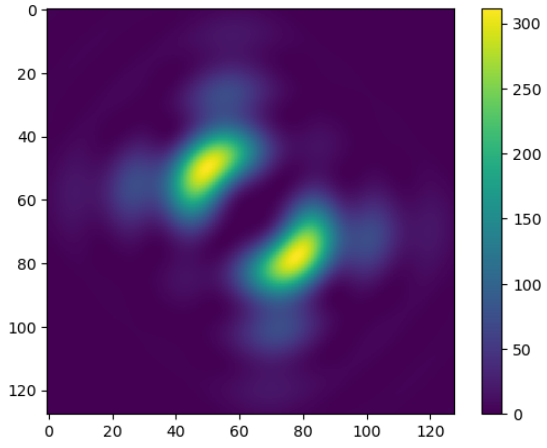

(b) Vertical astigmatism;
amplitude = -800 nm,
LH entrance polarization.

Figure 10.5: Images obtained by simulations using the same configurations as the measurments made on VODCA (vertical astigmatism, ±800 nm, LH entrance polarization.

in Figure 10.5 confirms the pattern obtained with two separated bright spots oriented at ±45°. Contrary to the images obtained on VODCA in Figure 10.3 the images obtained through simulation in Figure 10.5 present a relative oblique axis symmetry. This symmetry appears due to the simulated perfect centering of the incoming light beam on the AGPM,

which is not achieved with the laboratory measurements. The difference in convention about the aberration sign between simulations and VODCA software had to be adapted to compare accordingly the results. As for the results from Figure 10.3, a rotation of 90° is observed between Figure 10.8a and 10.5b which confirms that the ambiguity has been lifted.

The simulations support the fact that this particular pattern orientation in Figures 10.3 isn't due to a setup error. The particular pattern observed in Figures 10.3 and 10.5 correponds to the total aberration pattern obtained by imposing circular polarization through the AGPM. It is therefore not necessarily given that the pattern obtained with the circular polarizer and the AGPM centered should be vertical.

10.2 Diversity on the entrance polarization

10.2.1 Results obtained on VODCA

Another measurement can be made to verify this diversity, it correponds to compare two images obtained with the same aberration sign but with different entrance polarization states. In particular, vertical astigmatism will be kept with 800 nm in amplitude and LH and RH will be compared as entrance polarization states. Moreover, the same setup is used with the AGPM centered and the same 10 high-order modes optimization as in previous section. Once again, the measurements made without the AGPM are first displayed to demonstrate the ambiguity.

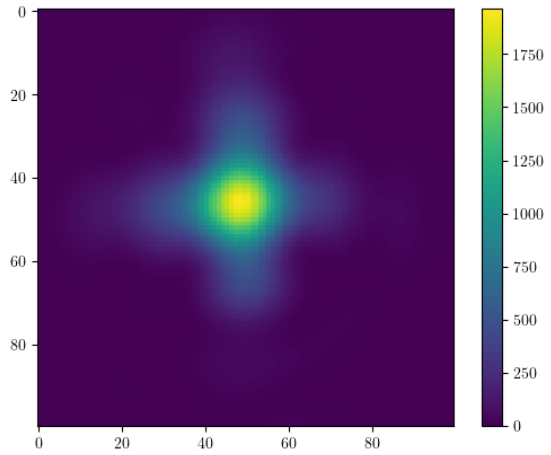

(a) Vertical astigmatism; amplitude = 800 nm
LP1 = 45°, without AGPM.

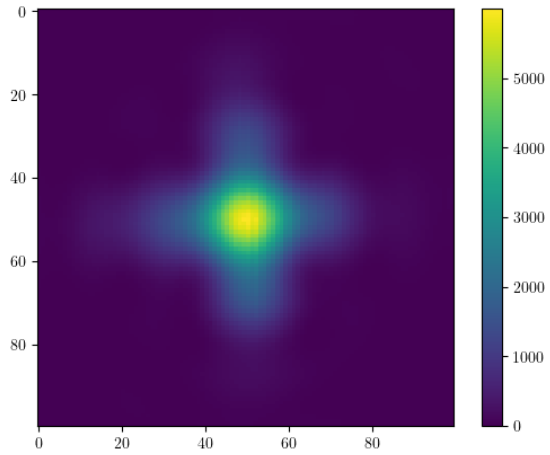

(b) Vertical astigmatism; amplitude = 800 nm
LP1 = 135°, without AGPM.

Figure 10.6: Comparison between images obtained with vertical astigmatism induced by the DM without using the AGPM and both orthogonal circular etrance polarization.

The same ambiguity as in Figure 10.2 is observed. The same observations are made and the results obtained with both orthogonal circular entrance polarization and the AGPM

on-axis are represented here after in Figure 10.7.

The same observations as in Figures 10.3 and are made here. The difference lies in the

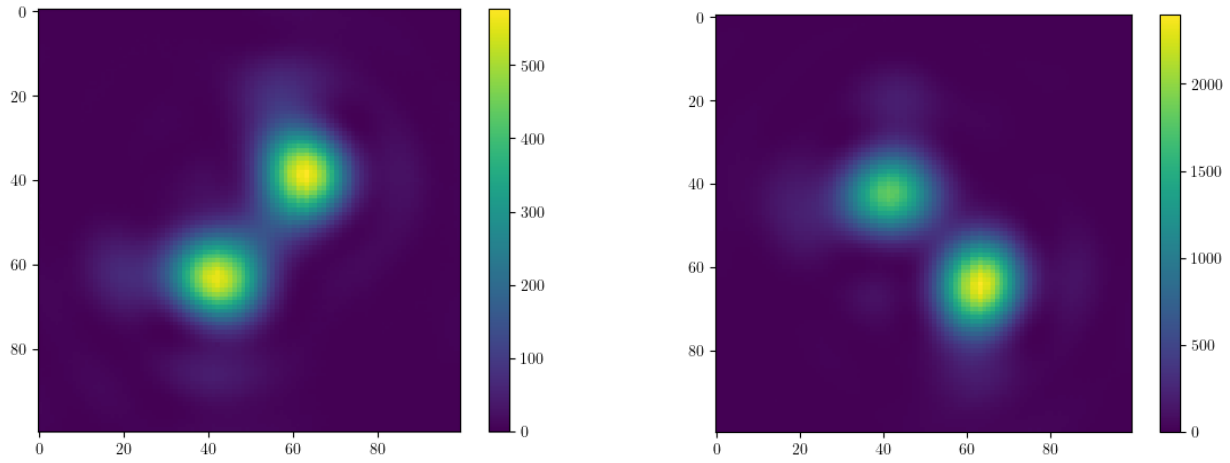

(a) Vertical astigmatism; amplitude = 800 nm
LP1 = 45°

(b) Vertical astigmatism; amplitude = 800 nm
LP1 = 135°

Figure 10.7: Comparison between images obtained with vertical astigmatism induced by the DM using the AGPM.

rotation of the pattern from one configuration to the other in Figure 10.7 which seems to be also 90° but in the other direction.

The other significant difference is the intensity of the light in the image which is much more important in Figures 10.7b and 10.6b. This is due to the entry polarization which is RH. This effect has already been observed in previous results and is due to the polarization state of the source which can include more proportion of RH than LH polarization.

10.2.2 Results by simulation

Hereafter are represented the images obtained by simulations of the exact same configurations as in Figures 10.7 and 10.6.
The rotation of the pattern due to different entrance polarization comes from the intrinsic behaviour of the AGPM. Both orthogonal polarization will see a phase ramp with opposite signs. These opposite signs result in a difference between orientation of the patterns by 90°. When the same entrance polarization is used, the same effect appears when inducing opposite aberration magnitude. The opposite sign leading to a different orientation of the pattern is not induced by the phase ramp but by the sign of the induced aberration itself.

Again as in Section 10.1.2, the results obtained by simulations confirm the results obtained on VODCA. The last comparison lies in the aberration pattern obtained in normal imaging without the AGPM is actually the same with both orthogonal circular entrance

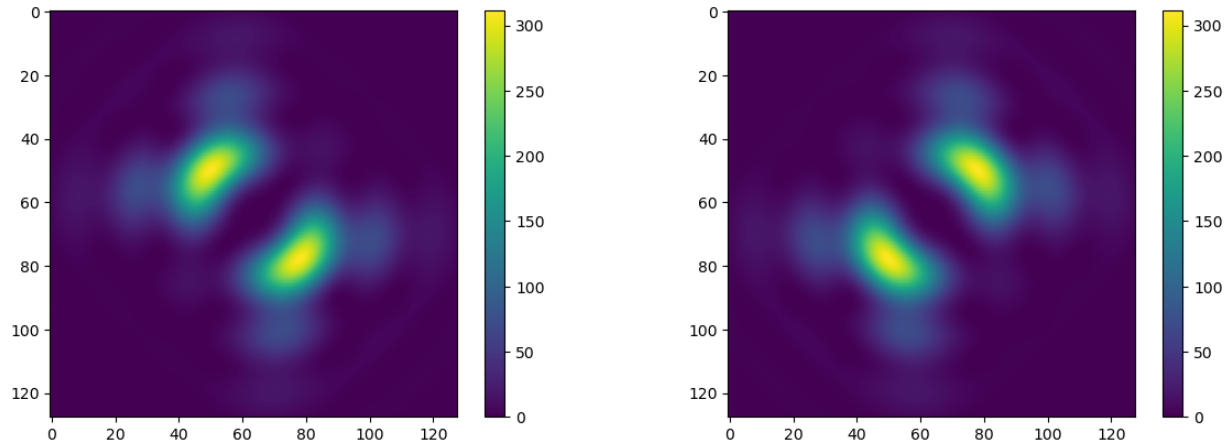

(a) Vertical astigmatism;
amplitude = 800 nm,
LH polarized light upon entry.

(b) Vertical astigmatism;
amplitude = 800 nm,
RH polarized light upon entry.

Figure 10.8: Images obtained by simulations using the same configurations as the measurments made on VODCA (vertical astigmatism, 800 nm, RH and LH polarization upon entry).

polarizations and with both aberration signs.

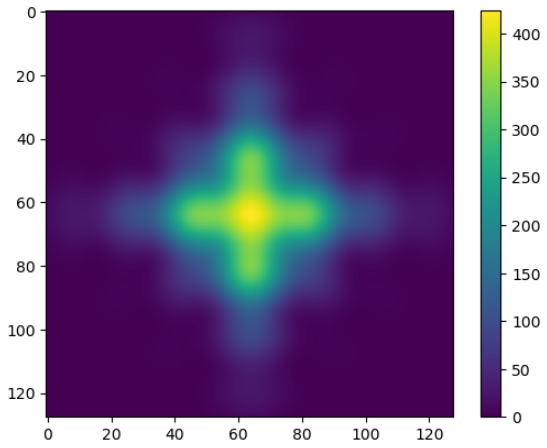

Figure 10.9: Image obtained by simulations using the same configurations as the measurments made on VODCA (vertical astigmatism;
absolute magnitude = 800 nm.

In normal imaging, with any entrance polarization and opposite signs or the aberration injected, the same cross pattern appears in simulations results in Figures 10.9 as it was first observed in Figures 10.2 and 10.6. More than showing an ambiguity present for normal imaging, this shows the vertical astigmatism pattern as it is usually expected between the

sagittal and the transverse foci, which confirms once more that the aberration injected is vertical astigmatism.

10.3 Conclusion

The dual polarization setup resulting from Part III lifted the ambiguity on the sign (and on the entrance polarization) as expected in the objectives from Section 3. This is the main goal of the dual polarization wavefront sensing since the ambiguity lifting allows the retrieval of phase information about the wavefont at the entrance pupil. Through phase retrieval, the wavefront can be reconstructed. This issue is actually discussed in next section.

11. Wavefront reconstruction

In this last section, the unambiguous dual-polarization setup will be used to test some wavefront reconstruction tests using Machine Learning (ML). This corresponds to a first demonstration of the wavefront sensing approach using a dual-polarization setup which is enabled by the analysis and results on polarization issue in previous sections. These tests are only preliminary results and represent a sample of what can be achieved with this type of Convolutional Neural Network (CNN). The training of the CNN is separated in different steps.

11.1 Data set acquisition

The first step is the acquisition of the data set. For this step, the system will acquire a great amount of images. The number of images is arbitrarily set to 10000. Random aberrations are applied to the wavefront and the resulting PSFs are acquired. The maximum amplitude of the wavefront errors can be chosen and it is arbitrarily set to 200 nm. From this data set, a model is constructed. The specific type of ML used in this case is supervised learning. As stated in A. Valizadeh et al, "Supervised learning is a branch of ML that entails training a model on a labeled dataset, where the desired output is already known". Therefore, different aberration modes are injected randomly in the focal plane which leads to a dataset which consists of 10000 different labeled images with the corresponding aberration modes injected and their magnitude. As in G. Orban de Xivry et al. [33], the data set is split in a 90:10 ratio. So over a data set of 10000 images, 9000 are used for the training and 1000 for the validation stage. The same procedure than in [33] is used. It corresponds to a batch size of 64 entries, with all batches constituting one epoch.

11.2 Training

Once the dataset is created, the training begins. The model is trained across 100 epochs, as it is seen in Figure 11.1. At each epoch, the batches are organized in a different way. For the architecture, ResNet-18 is used by default and Adam is used as optimization method, the latter being a method for stochastic optimization presented in D. P. Kingma and J. Ba [27]. ResNet states for Residual Network and 18 corresponds to the depth of the network. Residual Network is a specific type of neural network architecture, presented in He et al. [8], which includes shortcut connections between the layers. These additional connections don't imply additional parameter or complexity. The more depth the network is the more accurate the results are. ResNet-18 corresponds to very low depth architecture but offers faster convergence due to the smaller amount of parameters. Considering a preliminary test, this network will be satisfying.

The results of the training loss compared to the validation loss is plotted here with respect to the number of epochs. The CNN is actually trained to assign amplitudes to the different Zernike coefficients corresponding to the different modes.

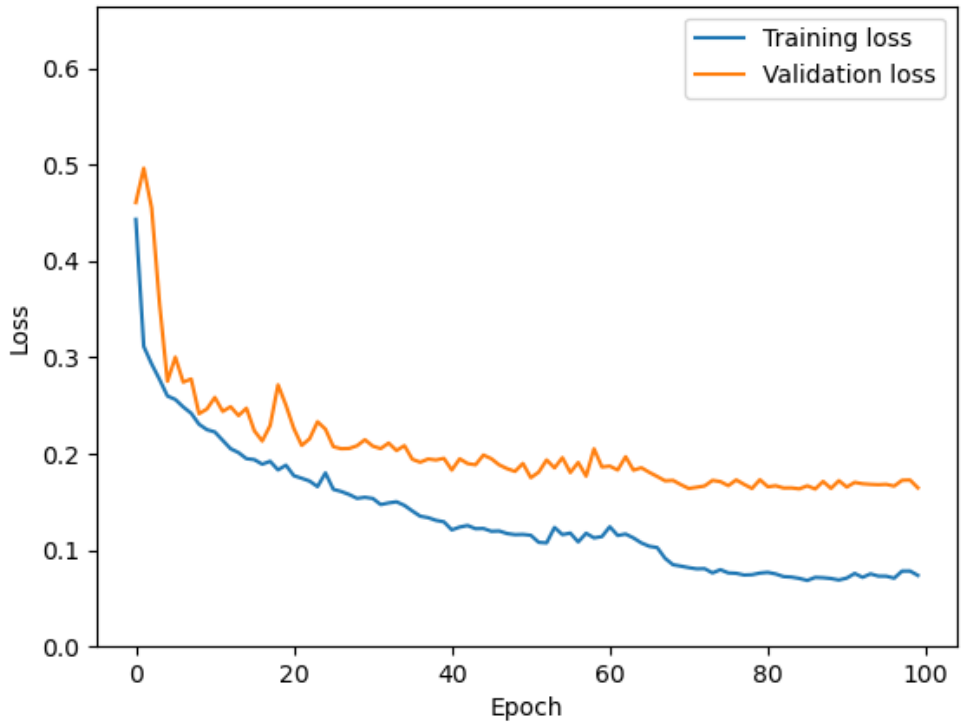

Figure 11.1: Learning curves for the model created.

At each epoch, the CNN is trained with 90% of the dataset and then validated using the other 10% with which haven't been used fo training. The loss on the y-axis represents the error between the predicted output and the true output. Plotting the loss of the model is one way to analyse the learning of the CNN, the other being by representing the accuracy. Contrary to the loss, the accuracy increases with the epochs if the CCN is learning. Here, the network is clearly learning in a relatively smooth way. The difference between the training and validation loss curves can represent the beginning of a relative overfitting. The overfitting occurs when the model is trained and learns with errors or noise too closely and fails to perform the same level of loss for the validation by well predicting with the test data [32] [31] [6]. In Figure 11.1, the validation loss doesn't decrease as much as the training loss which is logical at first since the model is not trained to be the most accurate with the validation data. However, as stated before this can imply the beginning of an overfitting, which is to avoid. However, since a significant learning is observed, the model is used for the next tests.

11.3 Model testing

After the training stage, the model is created and can be tested. Specific aberration modes are induced using the DM actuators. The CNN used the model created to estimate the Zernike coefficients of the phase aberrations induced and try to retrieve the initial wavefront by correcting the aberrations.

Different cases are tested, with oblique astigmastism, with defocus and with a mix of oblique astigmatism, defocus and trefoil. The induced aberrations are chosen in a arbitrary way to include some diversity. For each test, the gain is set to 1. The gain is a value between 0 and 1. A gain closer to 1 will apply the correction more agressively and the processus can recover the initial wavefront faster while a lower gain will apply the correction slower which can stabilize the processus but will take more time.

The first test corresponds to oblique astigmastim induced at 400 nm. Since the model is trained on 200 nm aberrations, more iterations should be necessary than if it was trained on 400 nm aberrations. 10 iterations maximum are fixed for the correction. The first, second and last iterations are depicted in Figure 11.2.

In the graph below the first three images in Figure 11.2a, the dotted red line is representing the aberration induced when calling the function to execute the model. The blue line corresponds to the corrected wavefront error in rms (nm). Already after the first iteration the aberration has been decreased more than half. Some corrections are also applied on other high order modes in order to get closer to initial wavefront even if no aberration was induced in these modes. After 10 iterations, the model has properly converged and has precisely identified the phase aberration induced. Even if it was trained with 200 nm aberrations, in 10 iterations it has corrected 400 nm oblique astigmatism and well approximated the inital wavefront.

The same model is tested with 400 nm defocus. In Figure 11.3, the first, second and tenth iteration are displayed with the same high order amplitude curves than before.

The CNN is as efficient to retrieve defocus as oblique astigmatism. Now, in order to complicate matters, the aberration induced on the wavefront will be divided in 3 different modes. It will induced 200 nm oblique astigmatism, 100 nm defocus and 50 nm trefoil.
This configuration seems to be more difficult to correct. This struggle can be seen by looking at the blue curve. The final iteration curve has less converged than the previous corrections in Figures 11.2 and 11.3. More than that, the final images seem to have more residuals with respect to the first PSF compared to the previous corrections. This can be solved by adding more iteration. However, the result is satisfying for preliminary results.

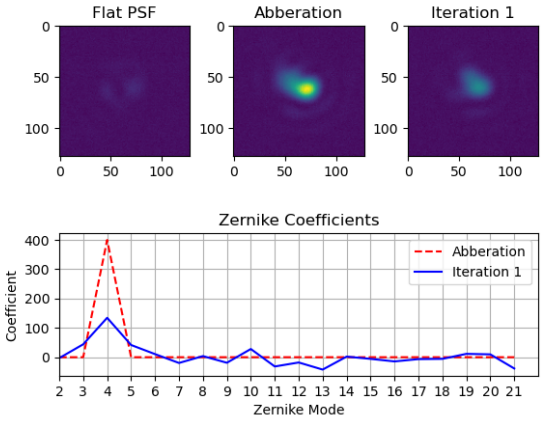

(a) 1^{st} iteration.

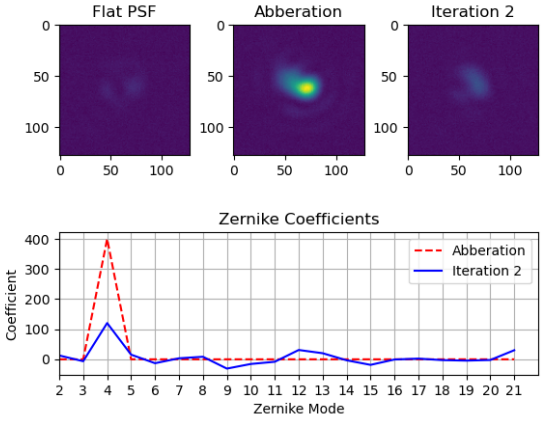

(b) 2^{nd} iteration.

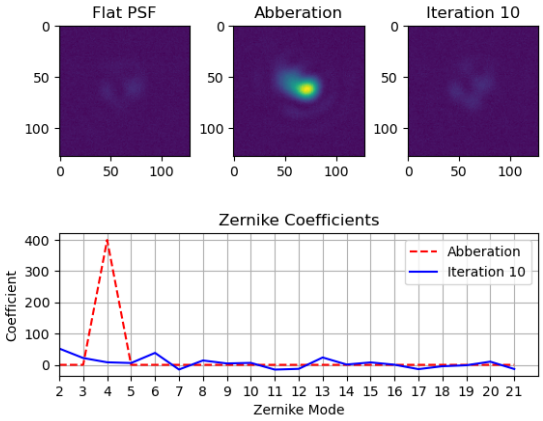

(c) 10^{th} iteration.

Figure 11.2: Wavefront reconstruction using the model created by inducing 400 nm oblique astigmatism. The gain is set to 1.

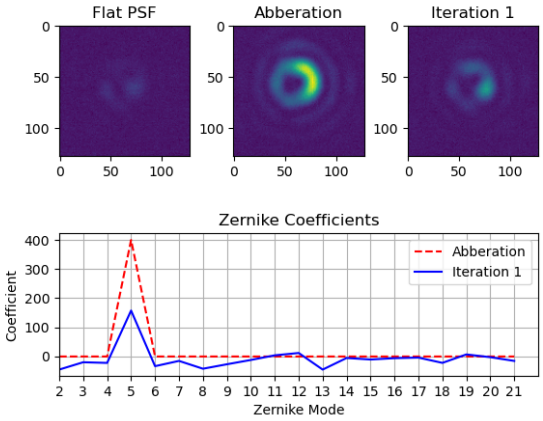

(a) 1^{st} iteration.

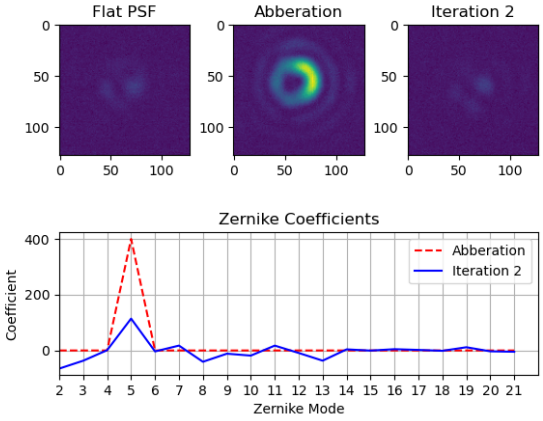

(b) 2^{nd} iteration.

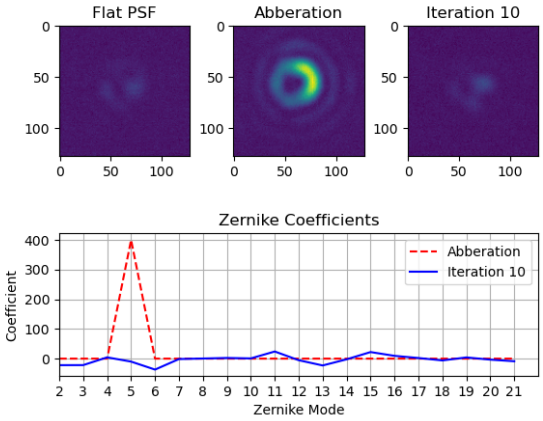

(c) 10^{th} iteration.

Figure 11.3: Wavefront reconstruction using the model created by inducing 400 nm defocus. The gain is set to 1.

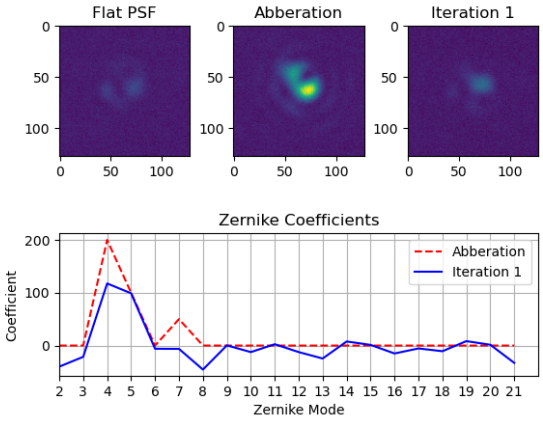

(a) 1^{st} iteration.

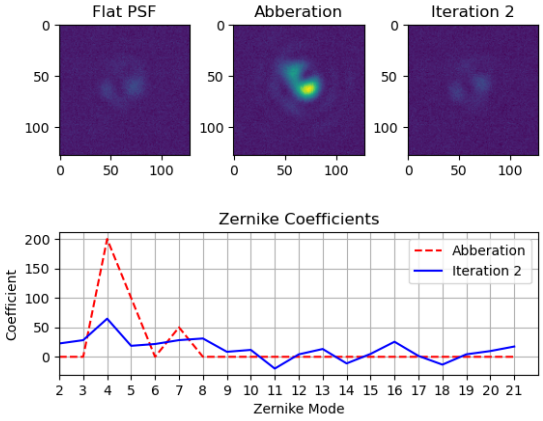

(b) 2^{nd} iteration.

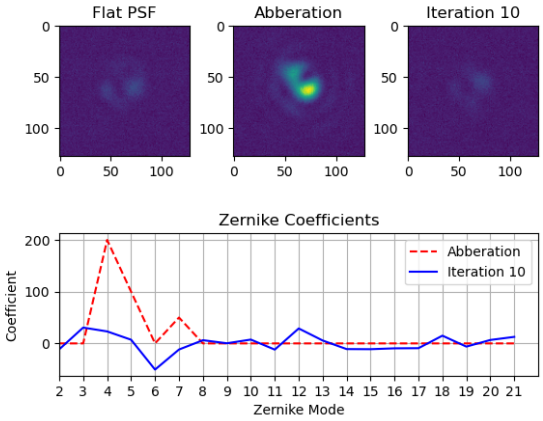

(c) 10^{th} iteration.

Figure 11.4: Wavefront reconstruction using the model created by inducing 200 nm oblique astigmatism, 100 nm defocus and 50 nm trefoil. The gain is set to 1.

11.4 Review

The performance of the phase aberration retrieval of the CNN has been observed. Once the model created and thanks to the diversity created by the dual-polarization setup, the CNN was able to reconstruct the wavefront from the injection of different aberrations. Since the CNN is trained on a data set created by inducing aberrations in the same, it is necessary that the AGPM is properly centered. If the setup on which the dataset is created is not precise enough, the CNN will learn on these imprecisions which will alter its performance in real conditions. However, the first results presented in this section were quite promising.

Part V

Conclusion and perspectives

12. Conclusion

This work have been persued in the sight of adaptive optics . The development and the research behind the different measurements have been made to characterize and ensure an accurate dual polarization setup to be used in wavefront sensing with the vortex coronagraph.

In this context, two polarization measurement methods have been presented and used to ensure the purest circular polarizer needed in the dual polarization setup. The final optimized circular polarizer was able to produce pure left-handed circular polarization at 98% and pure right-handed circular polarization at more than 97%. With the optimized circular polarizer, the dual polarization setup has been evaluated in terms of two particular performance, the extinction ratio and the rejection ratio. The setup has achieved two specific values of extinction ratio with a first contrast of 1924 in a setup without the presence of the AGPM and an exctinction ratio of 1521 when the AGPM is placed off-axis. The performance of the AGPM has been evaluated and a rejection ratio of 2010 for the AGPM has been obtained. Compared to particulary efficient previous results, this performance is quite remarquable. The global contrast achievable with the dual-polarization setup was up to 21e4. This performance ensures a sufficiently high accuracy of the setup to produce a necessary diversity for phase retrieval. This diversity is high enough to lift ambiuguity which limited the phase retrieval and therefore the wavefront reconstruction. Some relative successful wavefront reconstruction tests have been performed using machine learning with CNN trained on a dataset created on VODCA.

The accuracy of the setup can be more improved at different levels. A further optimization in the polarizer accuracy could improve the contrasts obtained and therefore could lead to a more precise phase retrieval. A more precise AGPM centering process can drastically improve the measured performance and allow a more robust diversity in the focal plane. These optimizations would lead to a more efficient wavefront reconstruction through a better training of the CNN.

However, the dual-polarization setup built and the performance obtained in this work represent promising prelimary results for the laboratory validation of the dual-polarization wavefront sensing using the vortex coronagraph.

13. Perspectives

High performing Adaptive Optics using wavefront sensing are particularly useful for ground-based observations due to non-common path aberrations induced by the atmosphere on the light flux coming from the host star and the potential exoplanet in its vicinity. However, space missions also require a performing wavefront sensing and control to be able to achieve the high-contrast imaging necessary for detecting and characterizing exoplanets.

The difference between ground and space missions lies in the frequency required for corrections which is much higher for ground missions due to atmosphere turbulence. In space, it is referred as active optics and corresponds to lower frequency corrections while on the ground, higher frequency corrections are required and it reffers to adaptive optics.

The research in adaptive optics is constantly evolving and more improvements are expected in the next years. One future challenging development lies in the extreme adaptive optics (XAO) which is used for the develoment of the PCS for the Extremely Large Telescope (ELT) [9]. PCS stands for Planetary Camera and Spectrograph and is designed to explore exoplanetary systems focusing on the formation, the evolution and the composition of exoplanet atmospheres. The challenge in this mission lies in the combination of XAO, coronagraphy and spectrosocpy with highest performance possible to meet the requirements. Indeed, the PCS will have to achieve an imaging contrast of approximately 10^{-8} at 15 milliarcseconds and 10^{-9} at 100 milliarcseconds to be able to observe exoplanets while being able to observe individual spectral lines to characterize the atmosphere constitution. These scientific goals can only be achieved through highly performing adaptive optics called extreme adaptive optics. The performance of the extreme adaptive optics will be highly dependent on the aberrations and NCPAs control.

Active Optics will soon be used in space missions including coronagraphic applications such as the Roman Space Telescope which will mark an important milestone in coronagraphy as the first active optics system on a space mission. Active optics wavefront sensing and control in the Roman Space Telescope will allow contrast 100 times better than passive coronagraph in space (e.g. Hubble's passive coronagraph) [12]. The system is not affected by atmospheric induced aberrations but the aberration control is still a key feature of the mission to ensure sufficiently high contrast performance.

It is without doubt that performing aberration and NCPA control will be a key factor for future coronagraphic applications, both on the ground and in space.

Bibliography

[1] A. Jolivet et al. "L- and M-band annular groove phase mask in lab performance assessment on the vortex optical demonstrator for coronagraphic applications". In: *Journal of Astronomical Telescopes, Instruments, and Systems* 5.2 (2019), p. 025001. DOI: 10.1117/1.JATIS.5.2.025001.

[2] A. Valizadeh et al. "Predictive precision in battery recycling: unveiling lithium battery recycling potential through machine learning". In: *Computers Chemical Engineering* 183 (2024), p. 108623. ISSN: 0098-1354. DOI: 10.1016/j.compchemeng.2024.108623.

[3] B. Schaefer et al. "Measuring the Stokes polarization parameters". In: *American Journal of Physics* 75.2 (2007), pp. 163–168. DOI: 10.1119/1.2386162.

[4] C. Delacroix et al. "Laboratory demonstration of a mid-infrared AGPM vector vortex coronagraph". In: *EDP Sciences* (2013). DOI: 10.1051/0004-6361/201321126.

[5] D. Mawet et al. "Annular Groove Phase Mask Coronagraph". In: *The Astrophysical Journal* 633 (Nov. 2005), p. 1191. DOI: 10.1086/462409.

[6] G. James et al. *An Introduction to Statistical Learning, with Applications in R*. Ed. by I. Olkin G. Casella S. Fienberg. Springer, 2013.

[7] G. Ruane et al. "Scalar vortex coronagraph mask design and predicted performance". In: *Techniques and Instrumentation for Detection of Exoplanets IX*. Ed. by Stuart B. Shaklan. SPIE, 2019. DOI: 10.1117/12.2528625.

[8] K. He et al. "Deep Residual Learning for Image Recognition". In: *CoRR* abs/1512.03385 (2015). arXiv: 1512.03385. URL: http://arxiv.org/abs/1512.03385.

[9] M. Kasper et al. "PCS — A Roadmap for Exoearth Imaging with the ELT". In: *The Messenger* 182 (2021), pp. 38–43. DOI: 10.18727/0722-6691/5221.

[10] M. Quesnel et al. "A deep learning approach for focal-plane wavefront sensing using vortex phase diversity". In: *Astronomy and Astrophysics* (2022). DOI: 10.1051/0004-6361/202143001.

[11] M. Quesnel et al. "Deep learning-based focal plane wavefront sensing for classical and coronagraphic imaging". In: *Proceedings of SPIE* (2020).

[12] N. J. Kasdin et al. "The Nancy Grace Roman Space Telescope Coronagraph Instrument (CGI) Technology Demonstration". In: *Instrumentation and Methods for Astrophysics* (2021). DOI: 10.48550/arXiv.2103.01980.

[13] N. Jovanovic et al. "Review of high-contrast imaging systems for current and future ground-based and space-based telescopes II. Common path wavefront sensing/control and Coherent Di.erential Imaging". In: *Adaptive Optics Systems VI* (2018). DOI: 10.48550/arXiv.1807.07043.

[14] O. Absil et al. *The VORTEX project: First results and perspectives*. Oct. 2014. DOI: 10.1117/12.2055702.

[15] O. Guyon et al. “Theoretical Limits on Extrasolar Terrestrial Planet Detection with Coronagraphs”. In: *The Astrophysical Journal Supplement Series* 167.1 (Nov. 2006), pp. 81–99. ISSN: 1538-4365. DOI: 10.1086/507630. URL: http://dx.doi.org/10.1086/507630.

[16] P. Riaud et al. “Instantaneous phase retrieval with the vector vortex coronagraph”. In: *Astronomy and Astrophysics* (2012). DOI: 10.1051/0004-6361/201219614.

[17] S. Babar and J. Weaver. “Optical constants of Cu, Ag, and Au revisited”. In: *Applied Optics* 54 (Jan. 2015). DOI: 10.1364/AO.54.000477.

[18] M. Born and E. Wolf. *Principles of Optics, Electromagnetic Theory of Propagation, Interference and Diffraction of Light*. Fourth. Pergamon Press, 1970.

[19] K. Crabtree. “Polarization Critical Optical Systems: Important Effects and Design Techniques”. In: (2007).

[20] *Deformable Mirrors Datasheet*. Version Revised 2023. URL: https://www.alpao.com/products-and-services/deformable-mirrors/.

[21] R. Galicher and J. Mazoyer. “Imaging exoplanets with coronagraphic instruments”. In: *Comptes Rendus Physique* (2023).

[22] D. Goldstein. *Polarized light, Revised and Expanded*. Ed. by Brian J. Thompson. Second. Marcel Dekker, Inc., 2003.

[23] B. I. Gramatikov. “A Mueller matrix approach to flat gold mirror analysis and polarization balancing for use in retinal birefringence scanning systems”. In: *Optik* 207 (2020), p. 164474. ISSN: 0030-4026. DOI: 10.1016/j.ijleo.2020.164474.

[24] E. Hecht. *Optics, Global Edition*. Ed. by Global Edition. Fifth. Pearson, 2017.

[25] A. Jolivet. “Development and exploitation of an infrared coronagraphic test bench for vortex phase mask performance assessment”. In: (2019).

[26] C. U. Keller. *Lecture 7: Linear Polarizers*. International Summer School On Solar Polarization, South Sichuan’s Bamboo Sea, Sichuan Province, China, 2011.

[27] D. P. Kingma and J. Ba. *Adam: A Method for Stochastic Optimization*. 2017. arXiv: 1412.6980 [cs.LG].

[28] M. A. Laughton and D. J. Warne. *Electrical Engineer’s Reference Book, sixteenth edition*. Newnes, 2003.

[29] P.-Y. Madec. “Overview of Deformable Mirror Technologies for Adaptive Optics and Astronomy”. In: (2012).

[30] D. Mawet et al. “The vector vortex coronagraph: laboratory results and first light at palomar observatory”. In: *The Astrophysical Journal* 709.1 (Dec. 2009), pp. 53–57. ISSN: 1538-4357. DOI: 10.1088/0004-637x/709/1/53.

[31] C. Perlich. “Learning Curves in Machine Learning”. In: *Encyclopedia of Machine Learning*. Ed. by C. Sammut and G. Webb. Boston, MA: Springer US, 2010, pp. 577–580. ISBN: 978-0-387-30164-8. DOI: 10.1007/978-0-387-30164-8_452.

[32] S. Shaeke and L. Xiuwen. “Overfitting Mechanism and Avoidance in Deep Neural Networks”. In: *CoRR* abs/1901.06566 (2019). arXiv: 1901.06566.

[33] G. Orban de Xivry et al. “Focal plane wavefront sensing using machine learning: performance of convolutional neural networks compared to fundamental limits”. In: *Monthly Notices of the Royal Astronomical Society* 505.4 (2021), pp. 5702–5713. DOI: 10.1093/mnras/stab1634.